Geotechnical Journal

EDITED BY:
Dr. N.H. Priyankara

ARTICLES REVIEWED BY:

Prof. Motoki Kazama

Dr. Chaminda Gallage

Dr. Pabasara Kumari

Dr. Radika De Silva

Dr. Avanthi Liyanage

Dr. Dinesha Jayasekara

GEOTECHNICAL JOURNAL

CONTENT

DEVELOPMENT OF COMPACTED CLAY LINERS (CCL) FOR SOLID WASTE LANDFILLS USING LOCALLY AVAILABLE EXPANSIVE SOIL

N. H. Priyankara[1], M. A. G. P. Perera[1] and A. M. N. Alagiyawanna[1]

[1]Department of Civil and Environmental Engineering, University of Ruhuna, Galle, Sri Lanka

ABSTRACT: Solid waste is a growing problem in urban areas of Sri Lanka and management of waste, both liquid and solid has become a critical environmental concern due to absence of engineered methods of disposing waste. Development of a simple engineered landfill facility utilizing locally available materials to suit landfill liner requirements is the most economical and the timely solution to this problem. In the present study, it was investigated the suitability of expansive soil which is commonly available in the south arid zone of Sri Lanka to use as clay liners in landfill facilities. The engineering properties of soil were improved by the addition of commercially available bentonite to build a low hydraulic conductivity barrier. However, the original engineering properties of soil-bentonite mixtures were significantly affected by the leachate interaction over a long period of time. Further, due to formation of shrinkage cracks in landfill clay liners lead to infiltration of leachate into ground during the rainy season. Therefore, in this research study, shrinkage behaviour of expansive soil, which is used to develop compacted clay liners, were evaluated using laboratory desiccation plate tests. A series of tests have been carried out with un-amended soil and soil amended with different percentages of bentonite. Digital image processing technique has been used to determine the Crack Intensity Factor (CIF). Higher desiccation rate was observed for smaller thickness of soil specimen.

Keywords: Clay liner, Expansive soil, Hydraulic conductivity, Shrinkage, Soil-leachate interaction

1. Introduction

Solid waste, especially Municipal Solid Waste (MSW), is a growing problem in urban areas of Sri Lanka and management of waste, both liquid and solid has become a critical environmental concern. The absence of engineered methods of disposing waste and the open dump approach adapted has created this major environmental and social problem of waste within most of the cities. Under open dumping, which is the main trend among local authorities at present, solid wastes are disposed haphazardly and they are subsequently subjected to open burning.

However, solid waste management is very important as people in many areas of the country depend very much on ground water for their drinking purposes and therefore, the contamination of ground water especially by the leachate generated in waste disposal sites should be kept at a minimum by following engineered waste disposal methodologies. Engineered landfilling is one of the best options to overcome the problems associated with contamination of ground water with leachate [Bagchi, 2004; David, 1993]. The liner system in an engineered landfill acts as a barrier for leachate and prevents the transportation of contaminants to the surrounding pollution prone environment. Hence liner system in a landfill becomes one of the critical design considerations [Bagchi, 2004; David, 1993]. A landfill liner is intended to be a low permeable barrier which is generally involves with the application of clay or synthetic material layer [Bagchi, 2004; David, 1993; Jayasekera, 2007]. Since, synthetic materials are very expensive, Compacted Clay Liners (CCL) is the most suitable liner system for developing countries [Ameta et al., 2007].

Expansive soil is a very commonly available material in the south arid zone of Sri Lanka and which can be used as a liner material. Expansive soil mainly consists of fine grained clay which occurs naturally and is subject to swelling and shrinkage, varying in proportion to the amount of moisture present in the soil [Gourley et al., 1993].

Only a limited number of researches are reported with respect to utilization of expansive soil as a CCL material in landfill sites [Jayasekera, 2007]. Therefore, a compacted clay liner was developed using locally available expansive soil in this research study. Further, long term effect of soil-leachate interaction on engineering properties of suggested clay liner was investigated.

It was reported that a lot of cracks have been developed during the dry season in most of the available clay liners [Morris et al., 1992; Abu-Hejleh and Znidarcic, 1995; Nahlawi and Kodikara,

2006]. This is basically due to the shrinkage behaviour of landfill liner material, which leads to infiltration of leachate into the ground during the rainy season. Thus, there is a possibility of contamination of ground water in this area due to development of shrinkage cracks in compacted clay liners. Shrinkage cracking is a complex phenomenon in soil. It is a natural process involving weathering, chemical and biological changes. Shrinkage cracks significantly affect the soil performance. Cracks create zones of weakness in soil and reduce its overall strength and stability. Occurrence of shrinkage cracks may due to several factors, such as clay content, mineralogy, soil thickness, surface configuration, rate of drying and total drying time etc [Alvis and Marcelo, 2011].

As such, in this research study, in addition to the hydraulic characteristics of CCL, an attempt was made to study the shrinkage behaviour of expansive soil. Laboratory desiccation plate test was used to study the shrinkage behaviour of clay and by applying digital image processing technique, geometric and kinematic characteristics of the surface crack pattern was described quantitatively.

2. Methodology

2.1 Engineering properties of expansive soil

In order to investigate the suitability of expansive soil to use as a clay liner, basic engineering properties of original soil collected from Hambantota, which is in south arid zone of Sri Lanka, were determined in the laboratory and presented in Table 1. The column corresponding to 0% bentonite represents the basic engineering properties of unimproved expansive soil. It can be seen that expansive soil is a highly plastic material.

X-ray diffraction test is the most accurate methodology to determine the mineral content of the soil. However, due to limited facilities available and high cost involved, the mineral content could not be found through x–ray diffraction method in this research study. Based on an empirical chart proposed by Savage, 2007, using Atterberg limits and clay content, it was realized that Illite is the most dominating clay mineral in this particular expansive soil.

Swelling potential of expansive soil was determined in accordance with Australian Standard AS 1289.7.1.1(2003) in this research study. The swelling potential is defined in terms of Shrink–Swell Index. By laboratory experiments it was noted that Shrink-Swell Index of the soil is 1.48%, which can be considered as medium swelling potential material.

In addition to the physical properties, hydraulic characteristics of the original material compacted at optimum moisture content, representing the compacted clay liners, were determined in the laboratory using falling head permeability test.

2.2 Improvement of engineering properties of expansive soil

In order to improve the engineering properties of natural expansive soil, different percentages of bentonite varying from 0 to15 % in steps of 5 % on dry weight were mixed with expansive soil and improved properties are depicted in Table 1.

The bentonite is an important naturally occurring clay mineral of great commercial importance possessing inherent bleaching properties [Stewart et al., 2003]. It falls mainly under montmorillonite mineral group and presents strong colloidal properties. Further variations of hydraulic characteristics of soil-bentonite mixtures were studied.

Table 1 - Engineering properties of soil- bentonite mixtures

Physical Property	Bentonite Percentage			
	0 %	5 %	10 %	15 %
Fine Content (%)	67	70	76	79
Clay Content (%)	55	62	65	68
Sand Content (%)	33	30	24	21
Liquid Limit (LL) (%)	41	41	43	49
Plastic Limit (PL) (%)	24	28	30	22
Plasticity Index (PI) (%)	17	13	13	27
Linear Shrinkage (LS) (%)	16	17	19	31
Max. Dry Unit Weight (kN/m^3)	17.0	16.9	16.6	16.3
Optimum Moisture Content (%)	19.0	19.5	22.0	28.0

2.3 Long term effect of soil-leachate interaction

The long-term effect of soil-leachate interaction on hydraulic conductivity and volume change properties of liner material were evaluated by allowing the compacted soil-bentonite mixtures to interact with leachate for a period of four months. After soil-bentonite mixture interact with leachate for a sufficient time, change of hydraulic conductivity was evaluated in the laboratory using falling head permeability test.

2.4 Shrinkage behaviour of landfill clay liner materials

In order to study the shrinkage behaviour of clay liner material, four number of circular type desiccation moulds with diameter of 20 cm were prepared using Perspex sheets. The thicknesses of the mould were 5 mm, 10 mm, 20 mm and 50 mm. The bases of the circular plates have been grooved in a circular manner to avoid soil sliding at the contact surface (Figure 1).

Soil has been air dried and sieved through 0.425 mm sieve to prepare the sample. The test sample was prepared by mixing sieved soil with water in such a way that initial water content of the soil is slightly higher than the liquid limit of the soil. Then samples have been manually placed into the moulds using spatula. Samples were placed in the moulds by ensuring that air is not entrapped within the soil layers. Then samples were allowed to air-dry under room temperature. The weight of the samples was recorded at predefined intervals (1 hour). Similarly, high resolution digital camera has been mounted at top of the setup to capture pictures at predefined intervals (1 hour). Hence, crack initiation time, crack propagation information and crack pattern were investigated.

Engineering properties of soil can be improved by the addition of commercially available bentonite to build a low hydraulic conductivity barrier in engineering landfills. Therefore, a series of tests have been carried out with un-amended soil and soil amended with 5% and 10% of bentonite in order to study the shrinkage behaviour of proposed liner materials. Further, the effects of oleic acid and coir on control of shrinkage behaviour were studied using desiccation plate tests. The bentonite amended soils were mixed with oleic acid (1g of oleic acid per 1kg of soil) and with Coconut coir fibers (5% of coir by volume) in this research study.
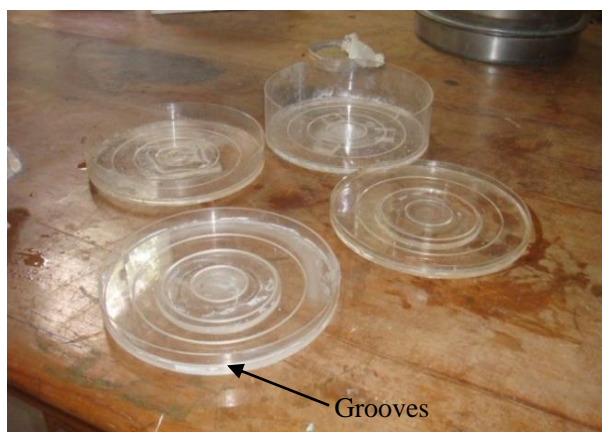
Figure 1 - Desiccation plates

3. Results and discussion

3.1 Particle size distribution

Particle size distribution plays a crucial role in evaluating the suitability of a soil to use as the liner material in a landfill site. The fine fraction should be high with low gravel content to ensure a low hydraulic conductivity through the soil. The particle size distribution of soil-bentonite mixtures is presented in Figure 2. It can be seen that fine fraction of the natural expansive soil is about 67%

and clay content is about 55%. This means that natural soil itself contains a higher fraction of fines.
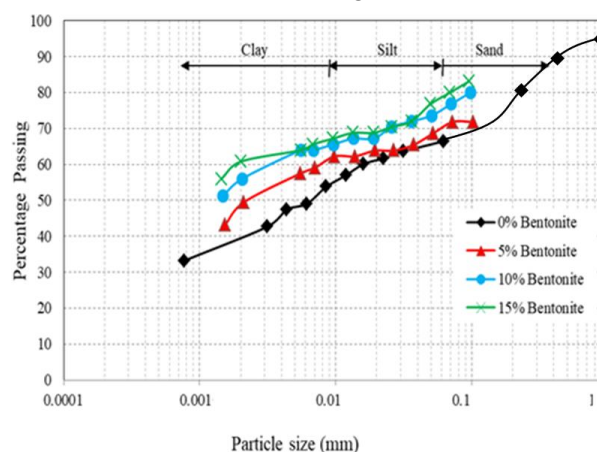
Figure 2 - Particle size distribution of soil-bentonite mixtures

The desired value of fine content of a landfill liner material is equal or greater than 20-30%. Therefore, the natural soil also satisfies this requirement. Since fine fraction of the bentonite is 100%, with the addition of bentonite to natural soil, fine content and clay fraction have been increased significantly as shown in Table 1. Conversely, it can be noted that percentage of sand content decreases with the increase of percentage of bentonite.

3.2 Plasticity Index

Variation of Atterberg limits with the addition of bentonite is presented in Figure 3. It can be seen that liquid limit of soil-bentonite mixtures gradually increases with the increase of bentonite content. A significant increase in liquid limit can be observed when the bentonite percentage is more than 10 %.

Plasticity index is another parameter which should be checked against the landfill liner requirements. It can be observed that liquid limit increases with the addition of bentonite whereas the plastic limit has no such relationship. Plastic limit increases with the addition of bentonite up to 10% and it has been reduced with further addition of bentonite. It can be seen that, the rate of increase of plastic limit is more than that of liquid limit up to the 10% bentonite addition, hence plasticity index decreases.

Plasticity index doesn't show any clear relationship with respect to the percentage of bentonite added. Initially plasticity index decreases up to the 10 % of bentonite content, and further addition of bentonite shows a huge increase in plasticity index. However, the requirement of a landfill liner material which is plasticity index should be more than 7 - 10 % is satisfied in all soil-bentonite mixtures [David, 1993]. Further, Table 1 shows that linear shrinkage limit of soil-bentonite mixtures were gradually increases over bentonite content. The significant

increase of plasticity index and linear shrinkage limit over 15% bentonite is due to the high water absorption capacity of bentonite.
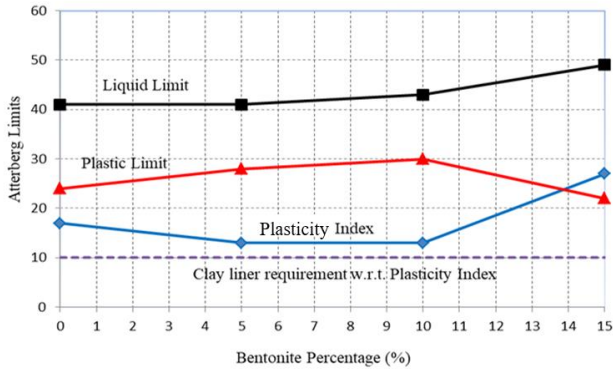
Figure 3 - Variation of Atterberg Limits with bentonite percentage

3.3 Compaction Characteristics

The variation of compaction characteristics of soil-bentonite mixtures is presented in Table 1 and Figure 4. It can be seen that maximum dry unit weight decreases whereas the optimum moisture content increases with the addition of bentonite. The decrease in maximum dry unit weight with increase in bentonite content may be attributed to high swelling characteristics of bentonite that forms a gel called as diffused double layer around soil particles. When this diffused double layer forms around the soil particles, the effective size of soil particles increases which causes increase in void volumes and thus decreased dry unit weights. The optimum moisture content increase over the bentonite content is due to the high-water absorption capacity of bentonite.
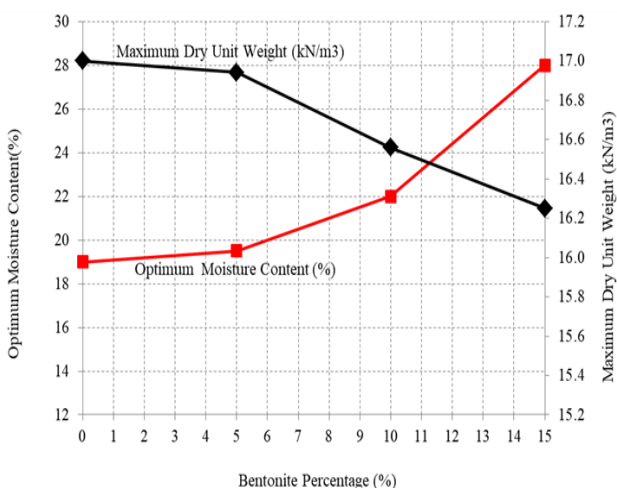
Figure 4 - Variation of compaction characteristics over bentonite content

3.4 Hydraulic Conductivity

The variation of hydraulic conductivity of soil-bentonite mixtures is illustrated in Figure 5. It can be noted that the hydraulic conductivity of soil-bentonite mixtures decreases with the increase of bentonite. With the increase of bentonite, which mainly consists of montmorillonite mineral, the diffused double layers surrounding the clay particles are getting thicker (Figure 6). As a result, the flow paths between the double layers become pinched off and the hydraulic conductivity decreases. Further, according to the Gouy-Chapman theory, the hydraulic conductivity is inversely proportional to the double layer thickness.

The results presented in Figure 5 clearly illustrated that the clay liner requirement with respect to hydraulic conductivity, *i.e.* 1×10^{-9} m/s, can be achieved with the addition of 10% of bentonite to the original soil.
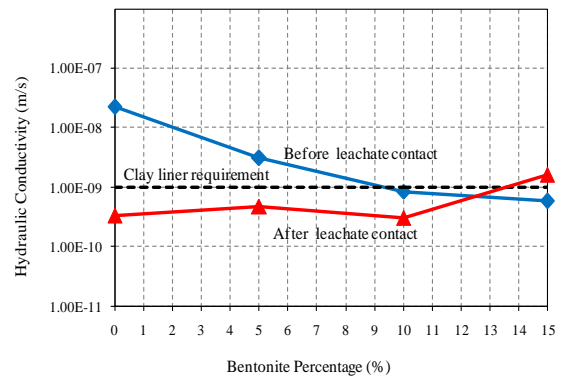
Figure 5 - Variation of hydraulic conductivity with bentonite percentage
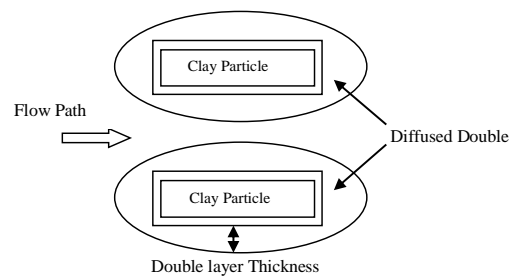
Figure 6 - Reduction of hydraulic conductivity due to increase of double layer

On the other hand, due to the formation of diffused double layer creates repulsive forces along the sides of the clay particles making it difficult for individual clay particles stay closer to each other. Under these repulsive forces, these clay particles align themselves in a more parallel orientation forming a dispersed structure; hence increase the void ratio over the increase of bentonite percentage (Figure 7).

4

According to the above results hydraulic conductivity is the governing factor to select the best percentage of bentonite that should be mixed with expansive soil, as all the other clay liner requirements are satisfied with the natural soil itself. Therefore, mixing 10% of bentonite by weight with expansive soil yields the best mixture for a clay liner and the comparison of clay liner requirements with those mixture properties are given in Table 2.

3.5 Engineering properties of soil-bentonite mixtures after a long-term leachate contact

Long term effect of soil-leachate interaction on hydraulic conductivity is the major factor which determines the satisfactory performance of a landfill liner. The variation of hydraulic conductivity of compacted soil-bentonite mixtures after contact with leachate is also illustrated in Figure 5. It can be seen that hydraulic conductivity of original compacted expansive soil has been decreased significantly after the interaction with the leachate. However, with the increase of bentonite percentage the hydraulic conductivity has been slightly increased and when it comes to a bentonite percentage of about 14%, hydraulic conductivity has been increased comparing to the before leachate contact state. Consequently, clay liner requirement gets dissatisfied.
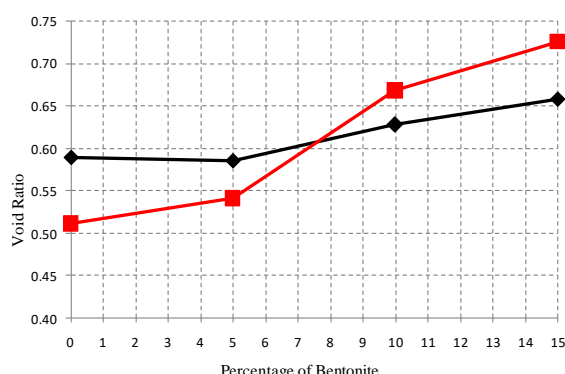
Figure 7 - Variation of void ratio with the addition of bentonite

Table 2 - Clay liner requirements

Property	Clay liner requirement	Expansive soil + 10% bentonite
Hydraulic conductivity	$\leq 1\times10^{-9}\,ms^{-1}$	$8.56\times 10^{-10}\,ms^{-1}$
Plasticity index	$\geq$ 7-10 %	13 %
Percentage fines	$\geq$ 20-30 %	75 %
Percentage gravel	$\leq$ 30%	< 2 %
Maximum particle size	$\leq$ 25-50 mm	2 mm

This reduction of hydraulic conductivity in original expansive soil after contact with the leachate is mainly associated with the clogging of soil particles due to precipitation of the suspended particles existing in the leachate and form a less permeable thin layer at the top. The slight increase of hydraulic conductivity over the soil-bentonite mixture after contact with the leachate is mainly due to reduction of diffuse double layer thickness, which causes increase of flow paths between the diffused double layers. In other words, soil-bentonite mixture has become less reactive (decrease swelling potential) after contact with leachate for a certain period. This is mainly due to the physio-chemical reactions between leachate and soil-bentonite mixture.

Similar results can be observed with respect to void ratio as shown in Figure 7 in soil-bentonite mixture after contact with leachate. The void ratio has been increased with the addition of bentonite, due to the effect of diffused double layer, where repulsive forces of clay particles increased the void spaces. The reduction of void ratio in the original expansive soil after interact with the leachate is mainly due to the precipitation of the suspended particles existing in the leachate, in the void spaces of soil, which leads to increase the volume of solid state in the soil; thus, void ratio has been reduced.

3.6 Soil water evaporation process

The shrinkage behaviour of clay liner is presented using soil water evaporation process. The variation of soil moisture content with time for different sample thicknesses are presented in Figure 8. The experimental results indicate that all samples have similar initial moisture content, which is slightly above the liquid limit of the soil. It can be seen that moisture content has been decreased with time irrespective sample thickness. A significant reduction of moisture content can be observed in thinner samples (5 mm and 10 mm). Further, it can be noticed that thinner samples have been reached to constant moisture content with time. The 5 mm thick sample has been reached to constant moisture content before that of other samples. This behaviour can be further explained using soil-water evaporation rate.

The variation of soil-water evaporation rate with time for different sample thicknesses are illustrated in Figure 9. Based on the figure, two evaporation stages can be easily identified irrespective of sample thickness, namely;
(a) Initial constant evaporation stage
(b) Falling evaporation stage

This evaporation behaviour can be explained with respect to the heat and mass flow between soil and air [Tang et al., 2011]. It was noted that 3

5

conditions must be satisfied for evaporation process to be existed in bare soil surface, namely;

- Continuous heat should be supplied to soil surface
- Vapor pressure at the atmosphere should be less than the vapor pressure at the soil surface
- Continuous water should be supplied to the soil surface
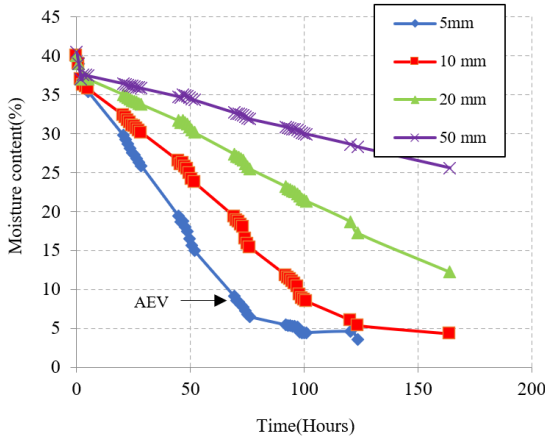
Figure 8 - Variation of moisture content with time with respect to different sample thicknesses
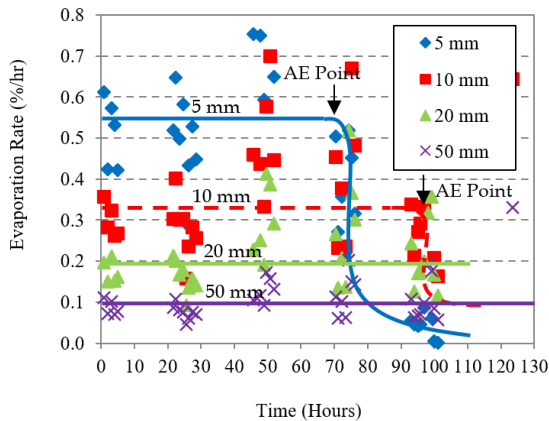
Figure 9 - Variation of evaporation rate with time

Based on the test results as shown in Figure 9, it can be noted that thinner sample has a higher soil water evaporation rate than that of others. The moisture in the deeply seated pores can be easily drawn to surface when the sample is thinner; as a result, higher evaporation rate can be expected. In addition, soil water content has been gradually diminished with time (Figure 8) and soil suction has been increased under constant evaporation rate.

The constant evaporation rate period has come to an end once the Air Entry Value (AEV) is reached. It can be seen that all samples have the same AEV (9%) irrespective of the sample thickness as AEV is a property of the material. However, when the sample is thicker, it takes longer time to reach to the AEV. At this point, air starts to penetrate into the soil pore spaces due to increase of suction, as a

result soil transition from a saturated state to an unsaturated state.

3.7 Quantitative analysis of shrinkage cracks

In order to quantitatively evaluate the development of shrinkage cracks during drying, a term Crack Intensity Factor (CIF) was defined, which is the ratio of crack area to total surface area. The variation of CIF with time for un-amented soil is depicted in Figure 10. It can be seen that CIF has been increased with time irrespective of sample thickness. However, there was no shrinkage cracks have been developed in 20 mm and 50 mm thick samples during the test period. Based on these observations, it can be concluded that development of shrinkage cracks is highly depended on the sample thickness; thicker the sample lesser the crack area.
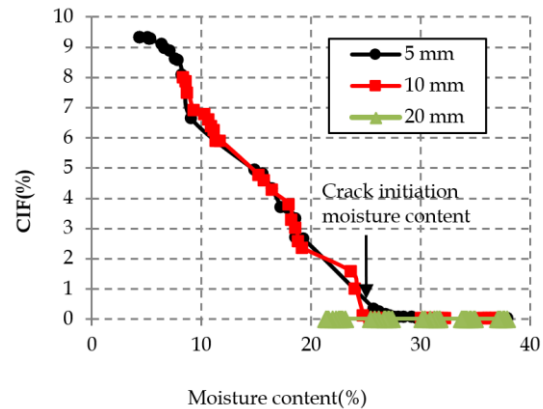
Figure 10 - Variation of CIF with time

In order to study the effect of moisture content on development of shrinkage cracks, CIF has been plotted against moisture content as shown in Figure 11. The figure clearly illustrated that CIF has been increased with the decrease of moisture content irrespective of sample thickness. It can be noted that under particular moisture content, CIF is same for both 5 mm and 10 mm samples.
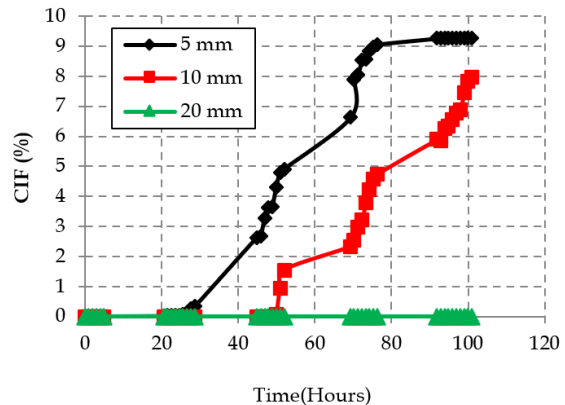
Figure 11 - Variation of CIF with moisture content

This implies that even though thinner samples have higher desiccation rate, crack area is directly proportional to the moisture content of soil. Based on these observations it can be concluded that cracks have been developed irrespective of the Compacted Clay Liner (CCL) thickness. However, if the CCL is thicker, the crack development rate is less. Also, by controlling the moisture present in the soil, crack development can be controlled.

As shown in Figure 11, moisture content at the crack initiation time is independent of the sample thickness. As per the laboratory test results, the average moisture content at the crack initiation time is approximately 25%, which is much more than the AEV (9%).

This clearly indicates that desiccation cracking has been initiated during constant evaporation stage, when the soil is still fully saturated.

3.8 Effect of Bentonite on shrinkage behaviour

As explained in the section 3.4 and section 3.5, bentonite has been successfully utilized to improve the hydraulic characteristics of CCL material. As such, it is very important to investigate the effect of bentonite on shrinkage behaviour of clay liner material. The variation of CIF with time for 5 mm and 10 mm thick samples are presented in Figure 12 and Figure 13 respectively. It can be seen that CIF has been increased with the bentonite content irrespective of sample thickness. With the increase of bentonite, which mainly consists of montmorillonite mineral, the diffused double layers surrounding the clay particles are getting thicker as shown in Figure 6. The diffused double layers create repulsive forces along the sides of the clay particles making it difficult for individual clay particles to stay closer to each other. As a result, cracks can be developed. The effect of bentonite on shrinkage behaviour can be further illustrated with the help of photographs as shown in Figure 14 and Figure 15.

Figure 14 depicts the formation of shrinkage cracks in un-amented soil and soil amended with bentonite in 5 mm thick samples, whereas Figure 15 depicts those of 10 mm thick samples. It can be seen that shrinkage cracks are orthogonal to each other. The cracks propagate both laterally and downward, and finally soil specimen has been split to clods. Further, it can be noted that 5 mm thick samples have higher desiccation than that in 10 mm thick samples irrespective of bentonite content, which shows the effect of sample thickness on desiccation. Photographs clearly illustrated that higher the bentonite content higher the crack formation.

Based on image analysis, it was noted that when a new crack is propagating close to an existing crack,

the new crack is attracted by the existing crack towards it, and new crack is at right angle to the existing crack (Figure 16). As a result, the final crack pattern is mostly square shaped clods.
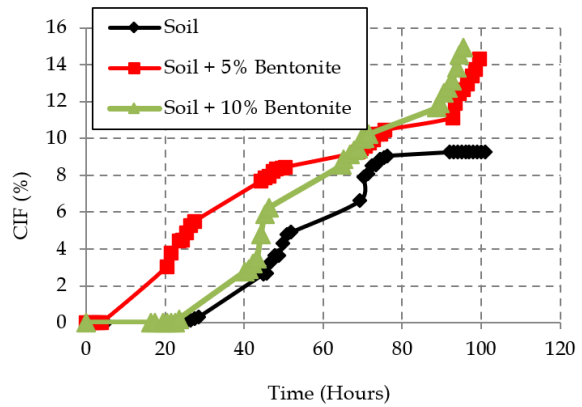
Figure 12 - Variation of CIF with time for 5 mm thick samples
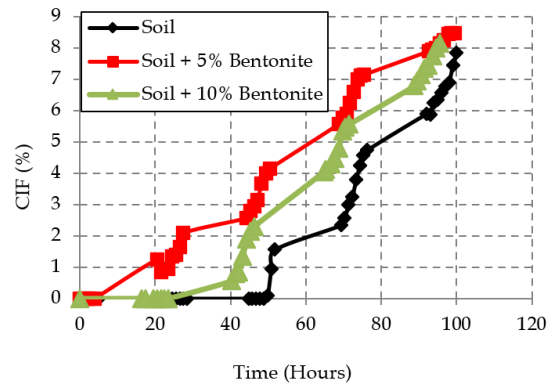
Figure 13 - Variation of CIF with time for 10 mm thick samples

    (a)   (b)   (c)
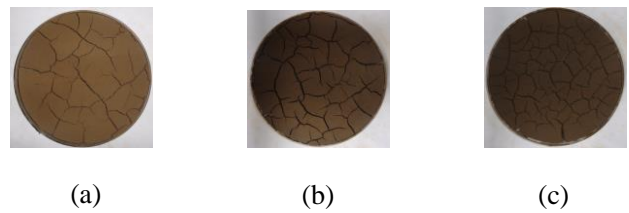
Figure 14 - Photographs of shrinkage cracks in 5 mm thick sample (a) Un-amented soil (b) Soil amended with 5% bentonite (c) Soil amended with 10% bentonite

Summary of the effect of bentonite content on shrinkage behaviour is presented in Figure 17 and Figure 18. Figure 17 shows the variation of CIF with bentonite content for different sample thicknesses whereas Figure 18 shows the variation of crack initiation moisture content with bentonite content for different sample thicknesses. Due to high water absorption capacity of bentonite, crack initiation moisture content increases with the bentonite content. In other words, shrinkage cracks have been easily developed (formed earlier) when

(a)   (b)   (c)
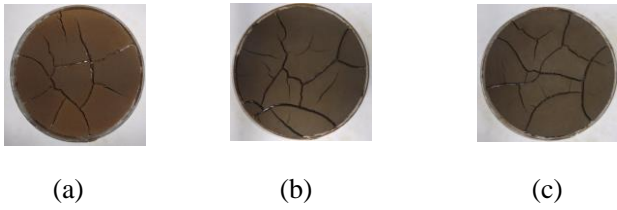
Figure 15 - Photographs of shrinkage cracks in 10mm thick sample (a) Un-amented soil (b) Soil amended with 5% bentonite (c) Soil amended with 10% bentonite

(a)   (b)
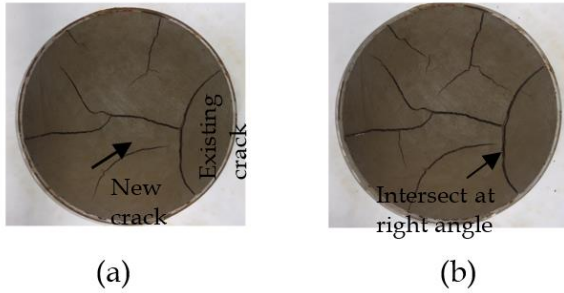
Figure 16 - Crack propagation manner (a) Propagation of new crack (b) Intersection of new crack with existing crack
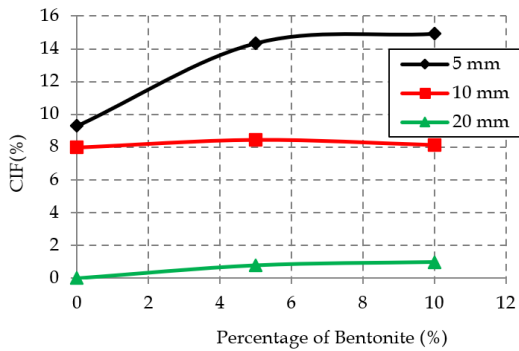
Figure 17 - Variation of CIF with bentonite content
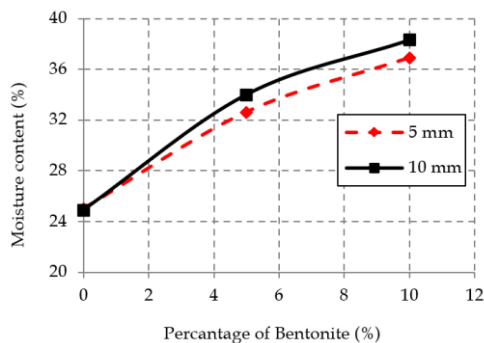
Figure 18 - Variation of crack initiation moisture content with bentonite content

the bentonite is present. Further, it is very clear that CIF has been gradually increased when the sample is thinner. However, there is no any noticeable increment in CIF over bentonite content when the sample is thicker.

3.9 Effect of Oleic acid on shrinkage behaviour

In order to reduce the shrinkage behaviour of clay liner material, oleic acid was used in this research study. Oleic acid is a product of olive oil, and which is an environmentally friendly product. A comparison of variation of CIF on un-amented soil, soil amended with 10% bentonite and oleic acid for 5 mm thick sample is presented in Figure 19. Even though oleic acid was added to control the shrinkage behaviour, it can be seen that with the addition of oleic acid, shrinkage behaviour of soil has been significantly increased. Further, cracks have been developed earlier when soil amended with oleic acid. Based on the laboratory test results, it can be concluded that shrinkage behaviour has been enhanced by the addition of both bentonite and oleic acid.
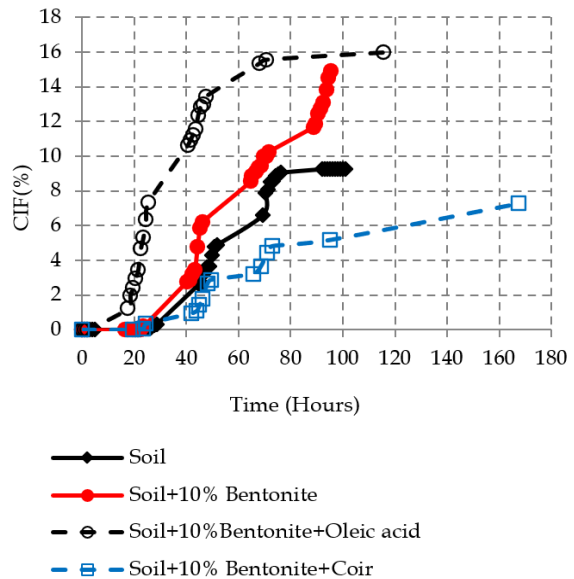
Figure 19 - Effect of oleic acid and coir on CIF
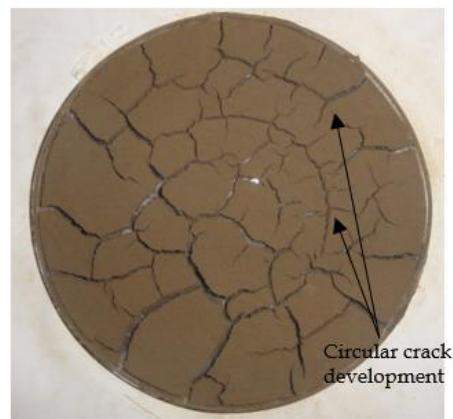
Figure 20 - Photograph of oleic acid amended soil-bentonite (10%) mixture

The shrinkage crack pattern of soil amended with 10% bentonite and oleic acid for 5 mm thick sample is shown in Figure 20. It was noticed that initially cracks were formed at the outer perimeter and gradually propagate towards to the center. Further, it can be seen that shrinkage cracks were developed in almost circular pattern. This behaviour is somewhat deviate from the previous observations on soil-bentonite mixtures.

3.10 Effect of Coconut coir fibers on shrinkage behaviour

In addition to oleic acid, coconut coir fibers were used as an admixture to control the shrinkage behaviour of soil in this research study. The average length of the coir fibers was 10 mm. The comparison of CIF with the addition of different admixtures to soil is presented in Figure 19.

Based on the figure, it is very clear that development of shrinkage cracks has significantly reduced with the addition of coir fibers. Coir fibers act as reinforcement and resist the tensile stresses develop during soil-water drying process, as a result crack formation can be reduced. In other words, due to inclusion of coconut coir fibers into soil, plasticity characteristics of soil have been getting reduced, thereby control the volume change behaviour of soil.

The shrinkage crack pattern of coconut coir amended soil–bentonite (10%) mixture for 5 mm thick sample is illustrated in Figure 21. As shown in split the soil specimen into clods is reduced; hair cracks have been developed. Further, it can be clearly observed that cracks with shallow depths have been propagated in circular pattern.
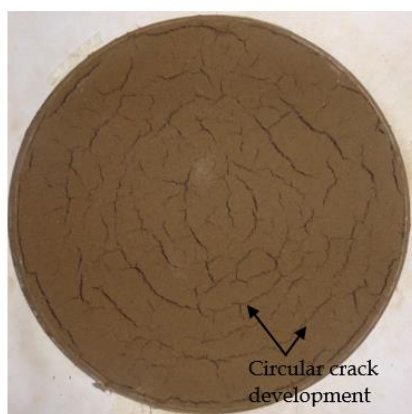
Figure 21 - Photograph of coconut coir fiber amended soil - bentonite (10%) mixture

4. Conclusions

Engineering properties of expansive soil can be well improved by mixing it with different percentages of bentonite. However, the rate of improvement of those properties gets reduced with the increasing bentonite percentage. Therefore, excessive addition of bentonite to expansive soil will not form a suitable mixture to suit clay liner requirements.

All the clay liner requirements other than the hydraulic conductivity get satisfied by the natural expansive soil available in south arid zone of Sri Lanka itself and therefore hydraulic conductivity is the governing factor which determines the most efficient percentage of bentonite. According to the laboratory experiments it can be concluded that addition of 10% of bentonite by weight will yields the most economical soil-bentonite mixture to build clay liners.

The original engineering properties of soil-bentonite mixtures can be significantly affected by leachate interaction over a period of time. After interact with leachate, the hydraulic conductivity has been significantly decreased in the original expansive soil whereas it has been slightly increased with the increase of bentonite percentage. Therefore, it can be concluded that, the satisfactory performance of the compacted clay liner is highly depending on the alteration of soil structure due to the soil-leachate interaction over a long period. These consequences will affect the satisfactory performance of the clay liner over time.

In addition to hydraulic characteristics, desiccation plate tests were conducted to study the shrinkage behaviour of CCL materials. Samples were prepared by mixing soil with water in such a way that initial water content of the soil is slightly higher than the liquid limit. Moreover, effect of bentonite, oleic acid, coconut coir fibers on desiccation cracking behaviour was studied. The water evaporation process, surface crack initiation and crack propagation behaviour were monitored during the whole drying process. The image processing technique was used to quantitatively analyze the desiccation crack propagation pattern.

Based on the laboratory test results, it can be noted that the soil-water evaporation process composed of two stages namely initial constant evaporation stage and falling evaporation stage. Thinner the sample, higher the soil water evaporation rate. Further, during soil-water evaporation process, the constant evaporation rate period comes to an end once the moisture content of the soil reaches to Air Entry Value (AEV) of the soil, at which soil transition from saturate state to unsaturated state. All samples have the same AEV irrespective of the sample thickness. However, when the sample is thicker, it takes longer time to reach to the AEV.

It can be concluded that desiccation cracking highly depend on the moisture presence in the soil. Formation of desiccation cracking is increased with

the decrease of moisture content irrespective of sample thickness. This indicates that desiccation cracks can be developed irrespective of the Compacted Clay Liner (CCL) thickness in a solid waste landfill. However, if the CCL is thicker, the crack development rate is less. In addition, desiccation cracking initiation time is independent of the sample thickness. Moreover, crack initiation moisture content is much more than the AEV. This indicates that desiccation cracking has been initiated during constant evaporation stage, when the soil is still fully saturated.

Based on laboratory experiments, it was observed that shrinkage cracks are orthogonal to each other. The cracks propagate both laterally and downward, and finally soil specimens were split to clods. Further, when new cracks propagate close to an existing crack, the new crack is attracted by the existing crack towards it.

When bentonite has been added to improve the hydraulic characteristics of CCL, formation of desiccation cracks has been increased due to presence of montmorillonite mineral in the bentonite. Utilization of Oleic acid to control the shrinkage behaviour of CCL was unsuccessful. However, coconut coir fibers can be effectively used to control the desiccation cracking behaviour of CCL.

REFERENCES

AS 1289.7.1.1 (2003), "Methods of testing soils for engineering purposes," Method 7.1.1: Soil reactivity tests - Determination of the shrinkage index of a soil - Shrink-swell index

Abu-Hejleh, A.N. and Znidarcic, D. (1995), "Desiccation theory for soft cohesive soils," Journal of Geotechnical Engineering, Vol 121, No. 6, pp. 493-502.

Alvis, A. and Marcelo, S. (2011), "Analysis of cracking behaviour of drying soil," 2nd International Conference on Environmental Science and Technology, Vol. 6, pp. 66-70.

Ameta N.K., Purohit D.G. M. and Wayal A.S. (2007), "Characteristics, problems and remedies of expansive soils of Rajasthan," Electronic Journal of Geotechnical Engineering - India, www.ejge.com.

Bagchi A. (2004), "Design of landfills and integrated solid waste management, "3rd edition, John Wiley and Sons Inc.

David E.D. (1993), "Geotechnical practice for waste disposal, "1st edition, Chapman and Hall, pp. 97-186.

Gourley C.S., Newill D. and Schreiner H.D. (1993), "Expansive soils: TRL's research strategy," Proceedings of the first international symposium on engineering characteristics of arid soils, City University, London.

Jayasekera S. (2007), "Long term effects of landfill leachate on volume change and hydraulic conductivity properties of expansive clays, "Proceedings of the Sri Lankan Geotechnical Society's First International Conference on Soil and Rock Engineering," Colombo, Sri Lanka.

Morris, P.H., Graham, J. and Williams, D.J. (1992), "Cracking in drying soils," Canadian Geotechnical Journal, Vol. 29, pp. 263-277.

Nahlawi, H. and Kodikara, J.K. (2006), "Laboratory experiments on desiccation cracking of thin soil layers," Journal of Geotechnical and Geology Engineering, Vol. 24, pp. 1641-1664.

Savage P.F. (2007), "Evaluation of possible swelling potential of soil," University of Pretoria, South Africa.

Stewart D.I., Studds P.G. and Cousens T.W. (2003), "The factors controlling the engineering properties of bentonite-enhanced sand," Applied Clay Science, Vol. 23, No. 1-4, pp. 97-110.

Tang, C., Shi, B., Liu, C., Gao, L. And Inyang, H.I. (2011), "Experimental investigation of the desiccation cracking behaviour of soil layers during drying," Journal of Materials in Civil Engineering, ASCE, Vol. 23, No. 6, pp. 873-878.

EVALUATION OF SLOPE STABILITY OF MUNICIPAL SOLID WASTE DUMP SITES USING PROBABILISTIC APPROACH

V. R. S. De Silva[1], N. H. Priyankara[1] and A. M. N. Alagiyawanna[1]

[1]Department of Civil and Environmental Engineering, University of Ruhuna, Galle, Sri Lanka

ABSTRACT*:* In Sri Lanka the most sought after method of disposal of Municipal Solid Waste (MSW) is unfortunately, open dumping. Unplanned dumping of MSW has resulted in disastrous shear failures. The purpose of this study is to determine shear strength parameters of MSW and to use it in proposing a method to evaluate slope stability for design of MSW dump sites in Sri Lanka. Landfilled solid waste samples were collected from dump site at Hambantota, a rapidly developing area. Shear strength parameters were obtained through direct shear apparatus produced cohesion ranging from 14 kPa to 74 kPa while the friction angle ranged between 25º and 48º. Reliability analysis via response surface method was adopted to evaluate failure probability of various slopes. Failure probabilities below 2% were observed for slopes ranging from 1:3 to 1:0.5.

1. Introduction

Municipal Solid Waste (MSW) generation has increased in mammoth proportions in the past few decades. According to the World Bank review on solid waste management in 2016, global city residents and commercial institutions generated a staggering 2.01 billion tons of MSW per year (www.worldbank.org). Furthermore, with rapid population growth and urbanization, annual MSW generation is expected to increase by 70% from 2016 level to 3.4 billion in 2050. As such, the current average daily per capita generation of 0.74 kg MSW is further expected to increase with rapid urbanization of the globe (www.worldbank.org).

Cities in low to middle lower income countries tend to have collection rates below 50% of waste generation, most of which is the waste that is not recovered for recycling. It is well known that the most common disposal method for collected waste in these countries is open dumps. Waste disposal in developing countries such as Sri Lanka, has not been given any significant attention over the past few decades. This had led to unregulated disposal of solid waste primarily in urban and suburban areas. Lack of attention given to solid waste disposal had led to the poor practice in disposing of solid waste in open dumps. Sri Lanka is among the largest MSW producing countries in terms of daily per capita generation.

Open dumps are the primary mode of disposing MSW in the country due to the lack of technical knowledge and financial constrains encountered in solid waste management. In addition, lack of sufficient land has led to dumping waste in high mounds and in steep slopes resulting in catastrophic failures in MSW slopes. One example for such failure can be taken as the Payatas Landfill in Manila, Philippines which was subjected to a shear failure in the year 2000 where 1.2 million m^3 of waste of the top layer slid down the slope causing 230 reported deaths and over 800 people reported missing (Jafari et al., 2013). Similarly, the large garbage dump site at Meethotamulla in Colombo of Sri Lanka was slide on 14th of April 2017 caused 32 deaths with 8 more missing and affected a total of 1765 people (en.wikipedia.org). Another such recent failure in Sri Lanka can be taken from the 24 m high Bloemendhal open dump in Maligawatta which took place in mid-2009. Although, no harm for human life was recorded, the shear failure of the dump resulted in a considerable amount of property damage to the nearby dwellings in the adjoining area (worldfailure.com). However, evaluation of MSW dump site slope stability in Sri Lanka has not been previously done and it is a vital component which needs to be fulfilled for the design of engineered landfills.

Unlike soil, shear strength parameters of MSW tend to change over time and with location due

to bio-chemical degradation taking place within the waste body (Zhan et al., 2008; Reddy et al., 2009). As a result, evaluation of slope stability of MSW landfills has proven to be a tedious and unreliable task if done by adopting conventional Factor of Safety (FOS) method. Considering the high variability of shear strength parameters of MSW, a probabilistic approach was adopted in this study. To evaluate the stability of slope a methodology incorporating the uncertainties involved in determining shear strength characteristics of landfilled MSW, which can be adopted in determining slope stability of MSW dump sites, is presented in this paper.

2. Sample collection

Waste dump site at Hambantota Municipal Council, a rapidly developing area, was selected as the study area to obtain representative MSW. Hambantota is located in the Southern Province of Sri Lanka belonging to the south arid zone of the country. With a land area covering 322.54 km^2 and a population of 55289, the number of housing units in the Hambantota Municipal Council is 14518 (www.statistics.gov.lk). The daily generation of MSW within this area is about 20.4 tons and only 9.9 tons is collected and dumped at the Hambantota open dump site located about 5 km to the north of Hambantota city (Balasooriya et al., 2015).

Spanning across an area of 1 acre, the open dump site is located along Hambantota - Gonnoruwa main road. Dump site can be mainly categorized in to two zones with old and new waste. Schematic diagram of Hambantota Municipal Council waste dump site is depicted in Figure 1. Old dump areas are indicated by **A** and **B**. The old waste dump area indicated by **A** is about 15 years in age and was not selected for sampling as it is outside the elephant fence. The old waste area indicated by **B** is about 10 years in age. The new waste area indicated by **C** is less than 2 years in age. The area indicated by **D** is allocated for future landfill and intact area **E** is assumed to be uncontaminated with leachate. The dump site consists of a composting facility to utilize the large amount of organic waste arriving at the dump site. It is the usual practice that new waste is always pushed towards the old waste area **B** to acquire space for new waste dumping. Thus, even though, area **B** is categorized as old waste, it is a mixture of old and new waste. Further, most of the waste in the old waste area **B** is burned. This is a very

common practice in almost all open dump sites in Sri Lanka. An elephant fence **H** surrounds the existing dump site to protect it from wild elephants.
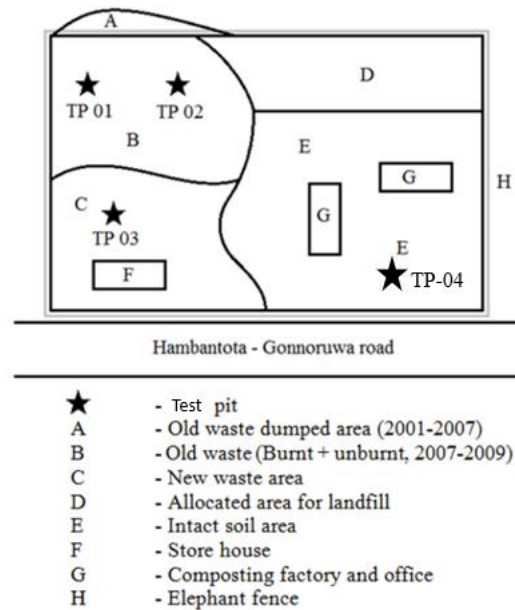
Figure 1 – Layout of the existing dump site at Hambantota (not to scale)

Waste and soil samples for the research study were obtained from four Trial Pits (TP) as shown in Figure 1. TP-01 and TP-02 represent the old waste area while TP-03 represents the new waste area. At each test pit in the waste area, samples were obtained at 0.5 m and 1.0 m depths from the waste surface. In addition, soil samples were obtained from each test pit at 0.5 m and 1.5 m depths from bottom of the waste layer as shown in Figure 2. This procedure was followed for both new and old waste areas. Note that the open dump site is relatively new, it was found out that below about 1.0 – 2.0 m of excavation, in-situ soils were present. Intact soil samples were obtained from TP-04 at 0.5 m depth. Two box samples were collected at each depth from all test pits.

It can be noted that conventional techniques cannot be used to collect undisturbed samples from the solid waste dump sites due to presence of large particle sizes. Moreover, as waste consists of particles like polythene and plastics, it is difficult to obtain undisturbed well representative samples using boreholes. Thus, a large size 300 mm cubical box was used to extract samples. First waste surface was smoothed and the steel box was driven in to the waste layer. Then a trench around the box was carefully excavated and the sample

was cut from bottom layer as shown in Figure 3. The method adopted made it possible to recover relatively undisturbed samples containing larger particles from the waste dump site while retaining its natural moisture content. The same procedure was adopted to obtain undisturbed soil samples in this research study.
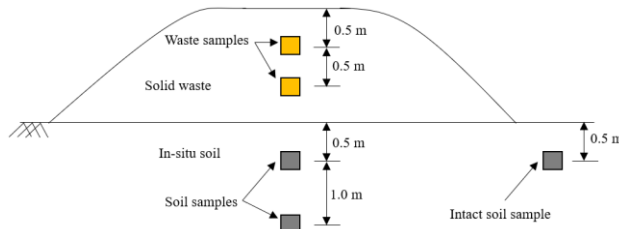
Figure 2 – Samples collection locations

Figure 3 – Box sampling

3. Laboratory testing program

3.1 MSW composition

Initially MSW components were sorted as bio-degradable and non-biodegradable by visual observations. The residual fines contained some inert fraction, but it was difficult to quantify this by visual observations. Therefore, air dried samples were heated in the oven to 440ºC to determine the organic content of MSW. The solid waste material obtained had a higher percentage of fine particles. Majority of the solid waste consisted of fine particulate matter which were indistinguishable. Thus, in advance to sorting, the solid waste sample was sieved through a 4.75 mm standard sieve to separate the fine component. Figure 4 illustrates the variation of composition of MSW with respect to location and age.

The composition of waste with age and location exhibited very little variation. In the categorization of waste, organic food waste was not distinguishable, although a major proportion of waste in Sri Lanka consists of food waste. The main reason behind such an observation could be due to the age of MSW collected. Dixon & Jones (2005) and Machado et al. (2010) described food wastes as easily biodegradable. Thus, it can be assumed that by the time of sampling most of the food waste had biodegraded. Furthermore, the reason for the low concentration of materials such as glass and metal is the scavenging induced by poverty in the developing countries (Jafari et al., 2013). Compressible waste, namely paper, plastic, polythene, wood, garden waste, and fabric occupied 2–8% of the total waste. It is noted that a marginally higher percentage of incompressible waste exists in the new waste than in old waste.
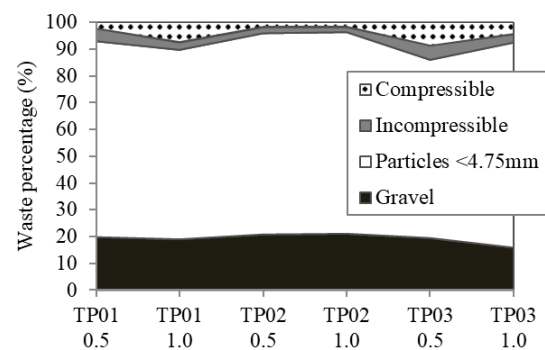
Figure 4 – MSW composition

The high concentration of gravel and other particulate matter in both new and old waste may be due to the practice of constantly bulldozing dumped waste towards the old waste area from the new waste area, which also results in mixing waste with soil. Consequently, the specific gravity of shredded MSW samples measured by water replacement method yielded results similar to that of soil (Ohata et al., 2015). Composition analysis of the waste at the Hambantota dump site conducted by Ohata et al. (2015) yielded results agreeing with this study, even though a different categorization was adopted considering diversity of materials. The particle fraction (< 4.75 mm) was 61.8% for new waste and 59.1% for old waste, while the gravel content was 29.5% and 23.7% for new and old waste, respectively (Ohata et al., 2015).

3.2 Index properties of MSW and soil

Summary of the index properties of waste and soil at new and old waste areas are illustrated in Table 1 to Table 3. The procedure of determination of index properties of waste and soil are described in Balasooriya et al. (2015). Based on the index properties it can be noted that MSW within the site is already subjected to higher biodegradation.

Table 1 - Index properties at new waste area (TP-03)

Description	Depth (m)	Liquid Limit (%)	Plastic Limit (%)	Plasticity Index (%)	Electrical Conductivity (μs/cm)	pH	Moisture content (%)	Organic content (%)	Specific gravity (Particle size < 1.7 mm)	Specific gravity (Particle size > 9.5 mm)	Bulk unit weight (kN/m³)	Dry unit weight (kN/m³)
Waste	0.5				450.0	7.52	6.22	1.35	2.72	2.69	18.07	
	1.0				595.5	7.43	61.93	39.64	2.49	2.15	12.63	14.4
Soil below the waste layer	0.5	32	14	18	1019.5	7.26	18.98	17.68	2.52		17.89	17.6
	1.5	59	28	31	634.0	7.82	14.18	3.03	2.29		17.25	

Table 2 - Index properties at old waste area (TP-01)

Description	Depth (m)	Liquid Limit (%)	Plastic Limit (%)	Plasticity Index (%)	Electrical Conductivity (μs/cm)	pH	Moisture content (%)	Organic content (%)	Specific gravity (Particle size < 1.7 mm)	Specific gravity (Particle size > 9.5 mm)	Bulk unit weight (kN/m³)	Dry unit weight (kN/m³)
Waste	0.5				235.5	7.34	17.8	8.30	2.46	2.44	12.81	17.0
	1.0				307.5	7.28	36.2	8.70	2.29	2.57	11.11	16.0
Soil below the waste layer	0.5	37	16	21	526.5	7.05	16.9	4.60	2.48		22.85	20.0
	1.5	50	23	27	269.0	5.93	11.6	2.96	2.50		16.96	

Table 3 - Index properties at old waste area (TP-02)

Description	Depth (m)	Liquid Limit (%)	Plastic Limit (%)	Plasticity Index (%)	Electrical Conductivity (μs/cm)	pH	Moisture content (%)	Organic content (%)	Specific gravity (Particle size < 1.7 mm)	Specific gravity (Particle size > 9.5 mm)	Bulk unit weight (kN/m³)	Dry unit weight (kN/m³)
Waste	0.5				480.0	8.20	24.1	8.02	2.60	2.53	12.89	17.0
	1.0	18			380.0	8.30	19.9	5.84	2.68	2.49	13.69	17.0
Soil below the waste layer	0.5	31	10	21	610.0	7.15	14.3	4.02	2.60		19.59	21.0
	1.5	35	19	16	332.0	11.57	12.0	1.45	2.51		17.44	

This behaviour can be explained with respect to organic content where very low organic content exists at old waste area when compared with that of new waste area due to biodegradation. The pH value is a very good indicator to understand the decomposition stage of MSW. It is well known that; micro-organisms are very active if pH is 6 - 9. Based on the results presented in Table 1 to Table 3, it can be seen that waste in the dump site consists of highly active micro-organisms. Electrical Conductivity (EC) is relatively high in the new waste than that of old waste. Also, EC of soil under the waste layer is much higher than that of intact soil. It is postulated that, soil under the waste is highly contaminated due to infiltration of leachate. Further, it can be noted that degree of contamination of soil in new waste area is much higher than that of old waste area, which implies the effect of fresh leachate on soil. Based on the result, it can be observed that EC of both waste and soil decreases with time irrespective of the depth; this is a clear indication of the effect of fresh leachate on waste degradation.

3.3 Shear strength characteristics

Direct shear tests were conducted to determine the drained shear strength parameters of soil and waste samples obtained from the dump site. Tests were performed in accordance with ASTM D3080. Conducting large scaled testing for MSW samples was not available in this study and direct shear tests conducted were limited to a maximum diameter of 100 mm and 45 mm thickness. Thus, MSW samples had to be shredded and remolded in order to conduct direct shear testing. For this purpose, initially compaction curves were developed by conducting standard Proctor compaction tests for shredded MSW samples of 4.75 mm maximum particle size. Maximum particle size of 4.75 mm was used for two main reasons. First reason is to eliminate the obstruction for movement of components in the direct shear apparatus by limiting maximum particle size to about one tenth of the smallest dimension of the sample prepared. This particle size is further justified because as shown in Figure 4 nearly 60% of the waste mass consists of particles which are less than 4.75 mm. Figure 5 illustrates the compaction curves developed for different solid waste samples. Higher dry unit weights were observed for compacted wastes. Values obtained in this study are highly unlikely compared to maximum dry unit weight of 5.9 kN/m^3 obtained by Reddy et al. (2009). Unlike typical MSW (with larger

proportion of plastic, paper and organic waste), samples obtained from Hambantota consisted of a higher percentage of gravel and sandy material which can be explained as the reason for such high compacted dry unit weights.
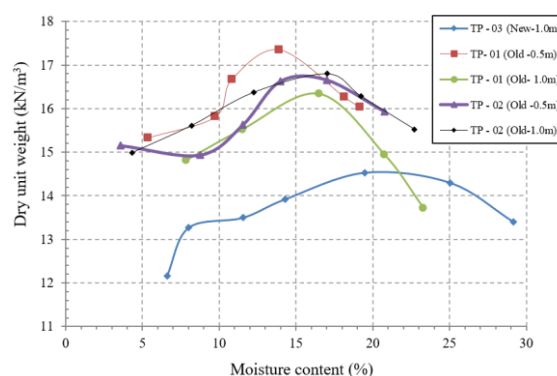
Figure 5 – Standard Proctor Compaction curves of the MSW

Considering the results obtained from standard Proctor compaction tests, waste samples were reconstructed with varying moisture content to determine the shear strength parameters through direct shear tests. For each test pit location, air dried waste samples were prepared with Optimum Moisture Content (OMC), OMC+3%, OMC+6%, OMC-3% and OMC-6% to obtain representative samples from the entire compaction curve. This allowed the collection of data while giving attention to the variation of shear strength parameters of decomposed MSW with moisture content and the degree of compaction which governs the unit weight of the sample. Zekkos (2010) has shown the importance of maintaining the unit weight of the samples as shear strength parameters tend to increase with increasing unit weight.

All direct shear tests were conducted under drained condition to obtain effective shear strength parameters. Samples were sheared at a constant shear strain rate of 0.15mm/min under different normal stresses of 25 kPa, 50 kPa and 75 kPa. For locations where soil was present under waste layers undisturbed samples were extruded from a circular cutter and sheared under the same vertical stresses.

When samples showed no peak shear stress, the stress at 15% shear strain was obtained to produce the Mohr-Coulomb failure envelope. Similar methodology was adopted by Reddy et al. (2009) in defining shear strength parameters for solid waste.

Composition of waste is a highly influential factor in determining the MSW shear strength

parameters. If separate samples are used to determine shear strength parameters at different normal stresses, it would yield scattered points making it difficult to produce a failure envelope. In order to overcome this difficulty, Zekkos et al. (2010) conducted a series of direct shear tests at several levels of increasing normal stress on the same waste specimen and reported that this method provides conservative estimate of shear strength parameters than use of separate samples.

To verify the argument of staged testing in MSW as explained by Zekkos et al. (2010), direct shear tests were conducted to separate waste samples and same waste sample at different normal stresses and the results were compared in this research study. Under the staged testing, once a sample was sheared, the normal stress was released and the sample was rested to the initial state. Then a higher normal stress was applied to the sample and the sample was allowed to compress. When there was no significant settlement in the sample, shearing of the subsequent stage was initiated. This procedure was adopted for three different normal stresses.

The typical direct shear test results for shredded MSW sample under different normal stresses is shown in Figure 6. Figure 6(a) shows the results when separate samples were used for each normal stress while Figure 6(b) shows the results when the same sample was used for different normal stresses. As shown in Figure 7 the Mohr-Coulomb failure envelops for separate samples and same sample are almost identical.

In most tests examined did not reach peak shear stress conditions during shearing. It is unlikely that a significant shear band developed in the waste specimen at the end of each loading stage. Thus, it can be assumed that waste was not significantly pre-sheared before the next load stage. And the shear surface that may have partially developed previously is compressed downwards due to recompression of the specimen under the higher normal stress, therefore new shear surface of the next stage of the test is created above the level of shearing imposed in the previous stage of the test. Which results in a shear surface that is different than that previously formed and is sheared during the next stage of the test. As such, pre-shearing effects would not be expected in the MSW shearing (Zekkos et al., 2010). Therefore, in this research study, stage testing method was used to obtain shear strength parameters.

The variation of cohesion and friction angle over moisture content is shown in Figure 8 and Figure 9 respectively. Both friction angle and cohesion showed an erratic behaviour with respect to moisture content. Also, no pattern in the variation of
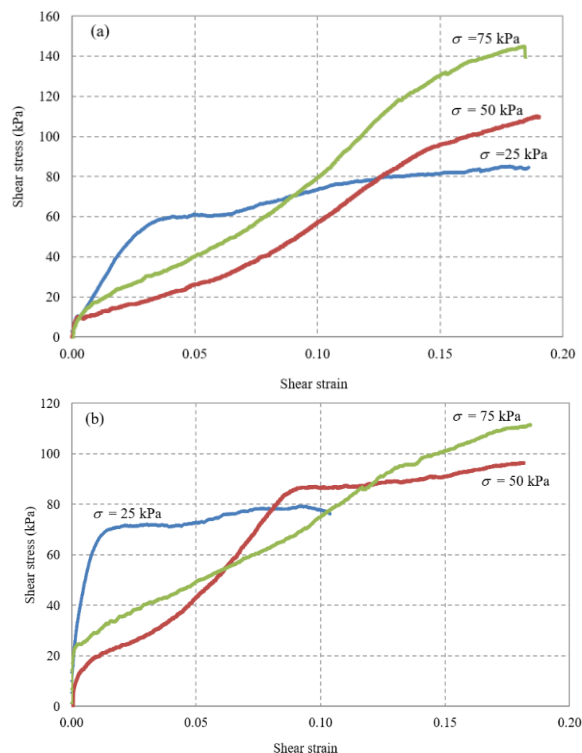
Figure 6 – Typical direct shear test result (TP – 01 Old waste – 1.0 m depth) (a) separate samples (b) same sample
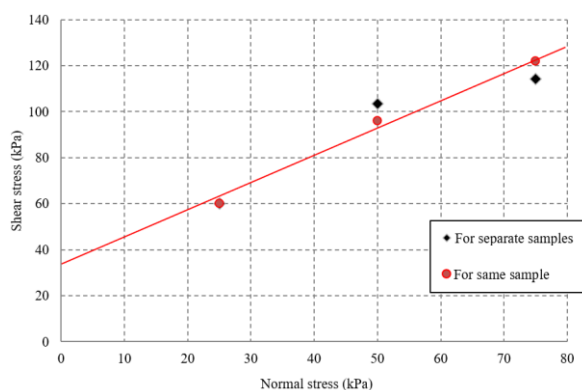
Figure 7 – Mohr-Coulomb failure envelope for shredded MSW for separate samples and same sample (TP – 01 Old waste – 1.0 m depth)

new and old MSW was observed in the summarized results in Figure 8 and Figure 9. This is an indication of the unpredictability of shear strength parameters of landfilled MSW. The effective cohesion ranged from 14 kPa to 74 kPa whereas the friction angle fluctuated between 25° to 48°. Reason for such extreme

variation of shear strength parameters are due to the inherently heterogeneous nature of MSW composition. These results further reinforce the need to resort to a probabilistic approach in evaluating the slope stability of MSW dump sites.
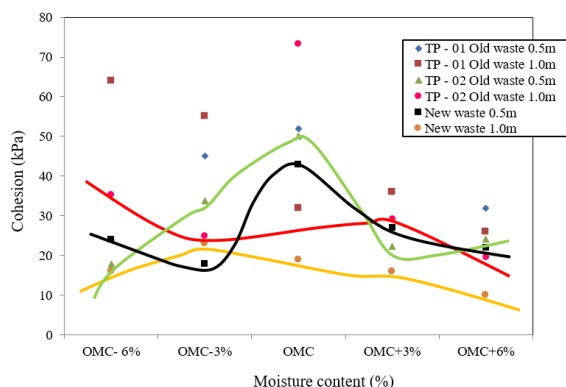
Figure 8 – Variation of cohesion with moisture content
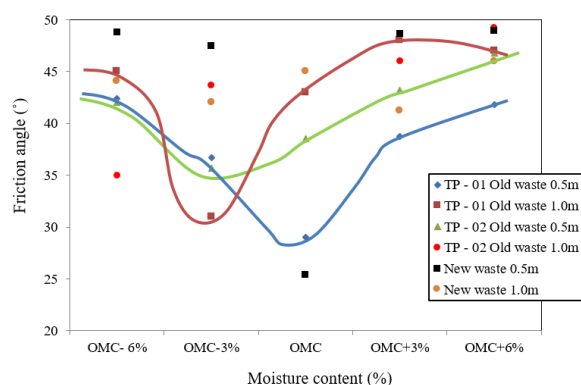
Figure 9 – Variation of friction angle with moisture content

4. Slope stability analysis

The slope stability of MSW dump sites were evaluated by adopting probabilistic approach to account for the high uncertainties and variability in the waste samples tested. For the purpose of evaluation, Reliability Analysis via Response Surface Method proposed by Xu et al. (2006) for embankments was adopted. Finite Element Modeling was adopted to evaluate the slope stability of each design slope angle.

4.1 Reliability analysis based on Finite Element Method

The conventional methods adopted in evaluation of slope stability of embankments cannot be used in the context of MSW dump sites, simply because the values obtained for the factor of safety will be inconsistent and will

not provide a comprehensive measure of risk. The reasons for the inconsistencies can be due to changes in shear strength parameters, errors in testing and environmental conditions. These uncertainties can be accounted for and a more consistent measure of slope stability can be obtained by resorting to a probabilistic analysis method (Xu et al., 2006).

According to Xu et al. (2006), the failure probability of a slope is given by Equation (1).

$$p_f = P[G(X) \le 0] = \int_{G(X) \le 0} f(X) dx \qquad (1)$$

Where, $G(X)$ is the performance function defined by Equation (2).

$$G(X) = F(X) - 1 \qquad (2)$$

Where, $F(X)$ is the function for the factor of safety and $f(X)$ is the probability density function of the basic variable vector, X. Due to the difficulty in identifying and integration of the probability function an approximate 2nd order polynomial function is defined for the performance function. Reason for defining a second order polynomial function and the procedure for reliability analysis is further elaborated by Low (1996) and Xu et al. (2006). The second order polynomial function which defines the approximate performance function can be written as in Equation (3).

$$G'(X) = l + \sum_{i=1}^{r} m_i x_i \sum_{i=1}^{r} n_i x_i^2 \qquad (3)$$

Where x_i, $i = 1,, r$ are random variables, l, m_i, n_i are parameters which need to be determined. For a function with n number of random variables $2n+1$ number of unknown coefficients need to be determined to define the performance function.

4.2 Modeling of two layered slope and Performance Function

For the evaluation of slope stability of the dump sites, two layered model was created using PLAXIS Finite Element modeling software. As indicated in Figure 10, waste layer of thickness 5 m and a soil layer of thickness 6 m were considered. This selection was done based on the site observations where the parent stratum was to be homogeneous to a depth of 6 m and the waste layer with the current composition is not likely to reach beyond 5 m in height.

The selected variables should have significant influence on the slope stability of the MSW dump site. Usually, the random variables used

in slope reliability analysis include the solid waste's unit weight (γ_1), cohesion (c_1), friction angle (ϕ_1), and supporting soil layer's unit weight (γ_2), cohesion (c_2), friction angle (ϕ_2) (Figure 10). As described, altogether 6 parameters were considered as random variables which govern the factor of safety. The depth of the supporting soil layer was not considered as a variable.

The values of the random variables at the chosen sampling point were determined. For each random variable, its mean value (μ_i) and two other values ($\mu_i \pm m\sigma_i$) were determined, where m is an arbitrary number. There is no rigid rule for a proper value of m. In the present analysis, the value of m was selected as 1. Consequently, for stability problems involving 6 random variables, the performance function for the factor of safety consisted of 13 (2x6+1) terms which meant 13 unknown coefficients had to be determined to define the performance function $G(X)$. Values for random variables required were selected from the database collected with the varying moisture content. Combination of new and old waste was used for sampling as no significant variation of shear strength parameters were visible between new and old waste.

The chosen values of the random variables were then used in the deterministic stability analysis to obtain the Factor of Safety (FOS) values for each slope angle of MSW dump site as depicted in Table 4. The finite-element program PLAXIS was adopted to estimate the FOS. The calculated FOS for each set of input parameters should be corresponded to the most critical failure mechanism at each slope angle. The critical failure surfaces of the four different slopes corresponding to dataset 1 is illustrated in Figure 11.
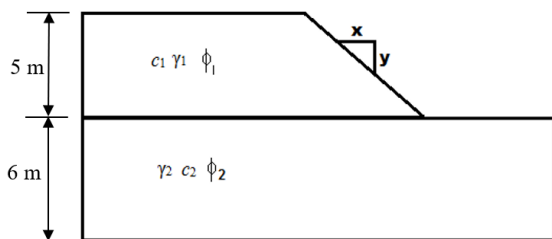
Figure 10 – Variables used to evaluate the slope stability

The calculated factor of safety values and corresponding input variables were used to construct a response surface $G(X)$ which represents the performance function for each slope considered in the analysis. Simple matrix multiplication can be used to solve the coefficients for the function for the Factor of

safety. It should be noted that the response surface in this case is a six dimensional function which passes through all thirteen points selected. Using the performance function defined the reliability index is calculated by using the First Order Reliability Method as explained by Low (1996).

(a) Slope = 1: 0.5

(b) Slope = 1: 1

(c) Slope = 1: 2

(d) Slope = 1: 3
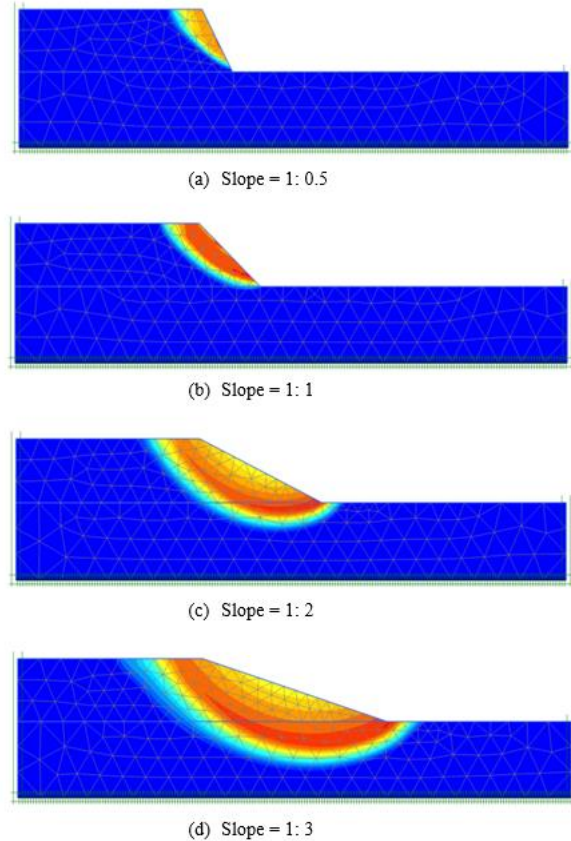
Figure 11 – Critical failure surfaces (Data set 1)

4.3 Reliability Index and Probability of Failure

The Reliability Index is defined as the minimum distance from the point of mean values of the random variables to the boundary of the limit state function in units of directional standard deviations. The reliability index β, is given by Equation (4).

$$\beta = min_{X=F}\sqrt{\left(\frac{X_i - m_i}{\sigma_i}\right)^T (R)^{-1}\left(\frac{X_i - m_i}{\sigma_i}\right)} \qquad (4)$$

Where R = correlation matrix, m_i = mean of the random variable and σ_i = standard deviation of random variable x_i. The reliability index is calculated based on the limit state function when, $G(X) = 0$. For the analysis of this study the correlation matrix was considered to be a 6 x 6 identity matrix because the parameters had no correlation with one another. Microsoft

18

Table 4 - Input sampling points for performance function based on Finite Element Method

Data Set	Input Variables						FOS			
	MSW			Soil			Slope Angle (V:H)			
	C_1 (kPa)	ϕ_1	Υ_1 (kN/m³)	C_2 (kPa)	ϕ_2	Υ_2 (kN/m³)	1:3	1:2	1:1	1:0.5
1	18	47.48	17.69	30	21.80	15.85	4.39	3.80	3.01	2.24
2	23	41.98	16.99	36	49.70	17.25	6.11	4.71	3.51	2.71
3	27	48.57	18.70	49	36.90	16.00	6.82	5.47	3.68	2.73
4	16	41.42	17.85	30	21.80	15.85	4.20	3.58	2.55	1.88
5	43	25.64	18.40	36	49.70	17.25	6.57	5.17	3.69	2.84
6	45	36.75	18.53	32	35.75	18.00	5.95	4.99	3.97	3.25
7	55	31.02	18.16	32	35.00	14.92	5.85	5.03	4.14	3.52
8	36	38.86	19.17	24	39.00	17.43	5.46	4.51	3.47	2.82
9	36	48.00	18.88	32	35.75	18.00	5.97	5.04	3.69	3.22
10	34	35.75	17.69	32	38.67	17.11	6.05	4.92	3.59	2.75
11	25	43.70	19.04	41	47.00	15.64	6.18	4.77	3.24	2.41
12	22	43.20	19.43	14	35.00	16.96	4.26	3.5	2.70	2.17
13	29	45.99	19.20	32	38.67	17.11	5.91	4.88	3.61	2.72
Mean m_i	31.51	40.64	18.44	32.31	37.29	16.72	5.67	4.64	3.45	2.71
Standard deviation σ_i	11.44	6.89	0.72	8.15	8.68	0.96	0.86	0.63	0.46	0.46

Excel's built-in Solver optimization tool was used to minimize the reliability index (Low, 1996). Based on the reliability index the probability of failure, P_f can be obtained by the Equation (5).

$$P_{f=} 1 - \phi(\beta) \qquad (5)$$

Where ϕ = Cumulative Distribution Function (CDF) of the standard normal variable. The random variables should be normally distributed and the limit state surface should be planar. The failure probability used here means the probability that the performance function G(X) = F(X) −1 is equal to 0 in the presence of parametric uncertainties.

Table 5 illustrates the reliability index values and corresponding probability of failure for each slope angle. A clear trend in the factor of safety is visible with the slope angle. There is an obvious reduction in the factor of safety of the slope with the increase of the slope angle. In addition, the reliability index (β) shows a reduction as the slope increases. Because the data were assumed to be normally distributed, the cumulative distribution function of the

standard normal variate was used to define the probability of failure. As the reliability index decreases, the probability of failure (P_f) of the slope increases.

It is clearly evident that even at a high factor of safety of 2.71 for the 1:0.5 slope, a high failure probability is existent due to the large variability between input parameters. According to the results, a clear trend can be observed where the failure

probability is increased from 0.001% to 1.995% with the increasing slope angle. According to Gibson (2011) the evaluated slopes can be categorized as;

- Slope 1:3 and 1:2 - P_f < 0.5%, for very long-term slopes (no monitoring is required)

- Slope 1:1 and 1:0.5 - P_f = 1.5% to 5%, for semi-permanent medium-term slopes (incidental superficial monitoring is required)

Table 5 - Input sampling points for performance

Slope angle (V:H)	Variable value at critical point						FOS (mean)	β	P_f
	MSW			Soil					
	C_1 (kPa)	ϕ_1	Υ_1 (kN/m³)	C_2 (kPa)	ϕ_2	Υ_2 (kN/m³)			
1:3	9.28	41.38	18.42	19.29	7.37	16.64	5.67	4.27	0.001
1:2	18.80	46.47	18.30	1.05	45.27	16.60	4.64	4.19	0.004
1:1	24.20	34.86	18.84	32.72	34.62	18.41	3.45	2.14	1.626
1:0.5	10.30	36.39	18.44	28.62	40.84	16.52	2.71	2.05	1.995

5. Sensitivity analysis of input parameters

The sensitivity analysis of the input parameters was conducted to identify the level of impact of each variable in the slope model towards the factor of safety in terms of Spearman rank correlation coefficient method. Influence levels of each parameter on varying slopes are depicted in Figure 12.

As shown in Figure 11(a), when the slope angle is 1:0.5, the failure occurs only in the waste layer, also known as a slope circle and therefore the factor of safety is more sensitive to the shear strength parameters of the waste layer. This relation can be easily identified by the significantly large Spearman's rank correlation coefficients of cohesion and friction angle of the waste layer as shown in Figure 12(a).
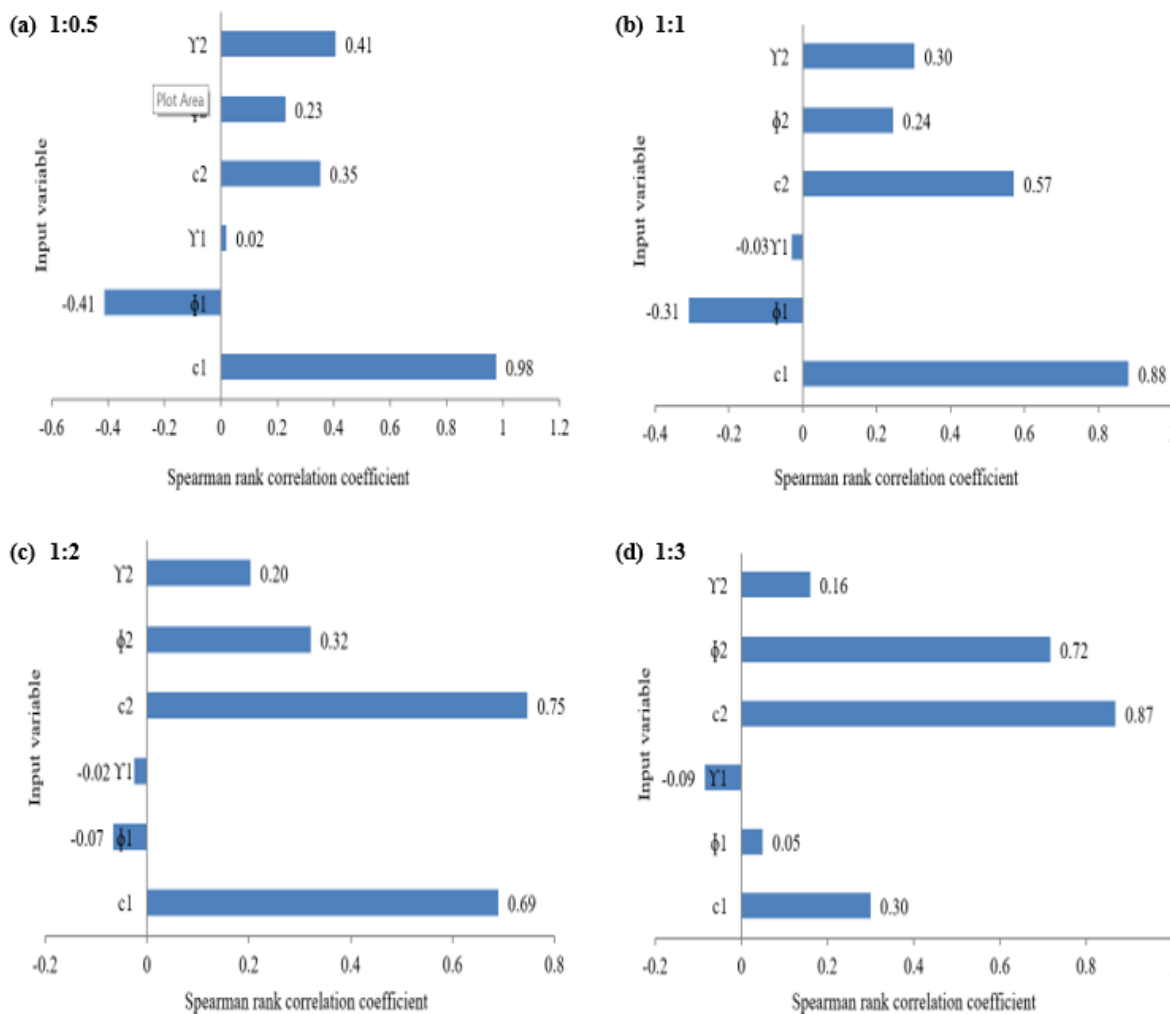
Figure 12 – Sensitivity analysis of input parameters

Similarly, when the slope angle is 1:1, critical failure surface resembles to a toe circle (Figure 11(b)) and thus, the cohesion and friction angle of the supporting soil layer also plays a contributing role to the factor of safety of the slope. As a result, the Spearman's correlation coefficients of the underlying layer have significantly higher values (Figure 12(b)) than those of slope angle of 1:0.5 (Figure 12(a)). Slopes with angles 1:2 and 1:3 fail under base failure mechanism where the slip surface propagates through the supporting soil media as illustrated in Figure 11(c) and Figure 11(d) respectively. Thus, the factor of safety is most sensitive towards shear strength parameters of the supporting soil layer as revealed by the spearman's rank correlation coefficients in Figure 12(c) and Figure 12(d).

5. Conclusions

Based on the results obtained from this research study, following conclusions can be drawn;

Shear strength of MSW mainly depends on waste composition, level of compaction, moisture content, leachate and age of MSW etc.

MSW shear stress–strain curves exhibit strain hardening behaviour, where MSW specimen is becoming stronger as the strain increases.

Shear strength parameters showed erratic behaviour for samples tested while direct shear test results proved to be very high. The reason behind such high cohesion and friction angle values can be explained by the fact that solid waste tested had a high content (about 60% by dry mass) of fine particles (< 4.75 mm) and gravel (about 20% by dry mass).

Laboratory direct shear test results depicted that cohesion of MSW vary between 14 kPa to 74 kPa whereas friction angle vary between 25° to 48°. Similar results were obtained soil below the waste layer where cohesion of soil varies between 24 kPa to 41 kPa while friction angle vary between 20° to 49°.

Slope stability of MSW landfills must be evaluated by adopting a probabilistic approach. Conventional FOS methods only consider a single set of input data when producing a factor of safety for a slope. Thus, variation in shear strength parameters of the waste layer and uncertainties involved in conducting tests are not accounted for. By using the reliability analysis via response surface method, the uncertainties involved with the spatial distribution of landfilled MSW shear strength parameters can be accounted for. The proposed model can be easily adopted in evaluation of slope stability of MSW landfills in the country and is compatible with various deterministic stability methods (both finite element modelling and limit equilibrium method) with readily available software without the need for additional coding.

The slope stability analysis illustrated that even with a higher factor of safety there exists a probability of failure for the slope angles defined.

The proposed method in this research study can be extended for analysis in the wet zone of the country incorporating pore water pressure within the waste mass as another random variable, enabling the evaluation of stability of a solid waste slope under saturated conditions. This will further increase the number of sample points required to determine the performance function for the factor of safety.

References

Balasooriya, B.L.C.B., Priyankara, N.H., Alagiyawanna, A.M.N., Dayanthi, W.K.C.N., Koide, T. & Kawamoto, K. (2015). Waste Amount and Composition Survey (WACS) in Galle and Hambantota Municipal Councils, *Proc. of International Symposium on Advances in Civil and Environmental Engineering Practices for Sustainable Development* (ACEPS), pp. 240–247.

Dixon, N. & Jones, D.R.V. (2005). Engineering properties of municipal solid waste, *Geotextile and Geomembarnes*, Vol. 23, No. 3, pp. 205–233.

Gibson, W. (2011). Probabilistic methods for slope analysis and design, *Australian Geomechanics*, Vol. 46, No. 3.

Jafari, N.H., Stark, T.D., & Merry, S., (2013). The July 10 2000 Payatas Landfill Slope Failure. *International Journal of Geoengineering Case Histories*, 2(3), pp.208–228.

Low, B.K., (1996). Practical probabilistic approach using spreadsheet. *ASCE Geotechnical Special Publication No. 58, Proc. Uncertainty in the Geologic Environment – From theory to Practice*, Vol. 2, pp.1284-1302.

Machado, S.L., Karimpour-Fard, Mehran, S., Carvalho, N., Miriam, F. & Julio, C.F.N. (2010). Evaluation of the geotechnical properties of MSW in two Brazilian landfills,

Waste Management, Vol. 30, No. 12, pp. 2579–2591.

Ohata, H., Saito,T., Tachibana, S., Balasooriya, B.L.C.B., Priyankara, N.H., Alagiyawanna, A.M.N., Kurukulasuriya, L.C. & Kawamoto, K. (2015). Geotechnical properties of municipal solid waste at open dumping sites located in wet and dry zones Sri Lanka, *International Conference on Geotechnical Engineering ICGE Sri Lanka*, pp. 669-272.

Reddy, K.R., Hettiarachchi, H.P., Naveen, S.G., Janardhanan, B. & Jean, E., (2009). Compressibility and shear strength of municipal solid waste under short-term leachate recirculation operations: Waste management and research, *The journal of the International Solid Wastes and Public Cleansing Association*, ISWA, 27(6), pp.578–87.

Xu, B., Low, B.K. & Asce, F., (2006). Probabilistic Stability Analyses of Embankments Based on Finite-Element Method, *Journal of geotechnical and geoenvironmental engineering* ASCE, pp.1444–1454.

Zekkos, D., George, A. A., Jonathan, D. B., Athena, G. & Andreas, T., (2010). Large-scale direct shear testing of municipal solid waste, *Waste management*, Vol. 30, No. 8, pp.1544–1555.

Zhan, T.L.T., Chen, Y.M. and Ling, W.A., (2008). Shear strength characterization of municipal solid waste at the Suzhou landfill, China. *Engineering Geology*, 97(3-4), pp.97–111.

https://www.worldbank.org/en/topic/urbandevelopment/brief/solid-waste-management, visited on 20/10/2021.

https://en.wikipedia.org/wiki/2017_Meethotamulla_landslide, visited on 03/05/2020.

http://worldfailure.com/index.php/government-failures/11-infrastructure-failure/233-colombo-sri-lanka-garbage-mountain, visited on 08/06/2014.

http://www.statistics.gov.lk/PopHouSat/CPH2011/Pages/sm/CPH%202011_R1.pdf, visited on 25/05/2015.

A COMPARATIVE STUDY OF USE OF DIFFERENT FACING TYPES IN SOIL NAILING IN SRI LANKA

B.I. Kumarage[1] and S.A.S. Kulathilaka[2]

[1]*National Building Research Organisation, Sri Lanka,*
[2]*Department of Civil Engineering, University of Moratuwa, Sri Lanka*

Abstract: Soil nailing has been used in Sri Lanka lately, as a cost-effective slope stabilization technique. However, detailed analyses with rigor, for facings/ nail heads are not often performed in the local practice. Full-face shotcrete, grid-beams, isolated nail heads, metallic meshes, and combinations of all these facings types are currently in use. The manner in which and how the basic functions such as anchoring the soil nails at slope-face, resisting local failures, and erosion control differ with facing type. In this study, design guidelines for various facing types are critically reviewed to assess the performance of soil nails and the surface slope stability. Further, a cost comparison of each facings type is presented. Some guidelines are developed for making the decisions on the most appropriate facing type depending on the prevailing conditions.

Keywords: Slope rectification, Soil nailing, Facing types for soil nailing

1 Introduction

1.1 *Background*

Soil nailing is a technique used to reinforce the existing or man-made sloping grounds to enhance stability. These structural elements, which are generally in the form of deformed steel bars are called Soil Nails. The steel bars could be either installed in bored holes which are subsequently grouted, self-drilled, or driven (Phear et al. 2005). The function of Soil Nails is to use the tensile capacity of reinforcement bars to enhance the overall shear strength of soils. The developed tensile loads are then transferred to the surrounding ground through bond shear stresses along the grout-ground interface.

1.2 *Soil nail facings*

Soil nails do not stabilize the exposed surface soil when used to stabilize existing slopes or excavations. Hence, a system of soil nails generally consists of head plates and/or facings of some form that connects the installed soil nails at the surface of the slope. In addition to the function of stabilizing the surface soil, the reaction forces produced by soil-nail heads/facing provide confinement and contribute to developing tensile forces along the soil nails. This tensile force acts in addition to the force developed by frictional interaction between the soil nails and the surrounding soil (Geotechnical Engineering Office. 2008).

As such, the forces induced by local instabilities on the facing/ nail head as well as the tensile forces at the nail heads shall be mainly considered in the design of soil nail facings.

1.3 *Failures of soil nail systems*

Occasionally, failures of soil-nailed walls occur even though not many public records are available. Several failures that can be attributed to matters related to facings such as inferior facing design, lack of attention towards the interrelationship between nail spacing and type of facing, and inferior construction practices have been reported (Phear et al. 2005). Hong Kong GEO (Geotechnical Engineering Office) Report No. 222 (Ng et al. 2007) presents several reported cases of failures involving soil nailing.

1.4 *Use of soil nail facings in Sri Lanka*

In Sri Lanka, different types of facings are being used. Facing designs are mostly adopted from Hong Kong publications. However, detailed designs for nail head/ facing are not often carried out. Currently, the selection of the facing type is mainly based on three major factors; observed nature of the surface slope and soil, ease of construction, and aesthetics.

BS EN (British Standards European Norm) 14490:2010 (British Standards Institution 2010) defines 3 main types of facings, Hard facings, Flexible facings, and soft facings. In the Sri Lankan practice, most of the types stated above are used in combinations. Such main types of facings are as follows:

- Hard Facings; Full-face shotcrete Fig. 1-(a), reinforced concrete grid beams Fig. 1-(b).

- Flexible Facings; High tensile steel wire mesh with metal bearing plates Fig. 1-(c) and high tensile steel wire mesh with isolated reinforced concrete nail heads Fig. 1-(d).
- Soft facings; Nail heads are not structurally connected. Some connection is provided to facilitate the growth of vegetation to prevent erosion. This may include, Coir meshes, and Geosynthetic mesh products.
- Mixed Types; Reinforced concrete grid beams along with high tensile flexible wire mesh with vegetation cover on the slope surface.

Fig. 1 (a) Full-face shotcrete, (b) Concrete grid beams, (c) High tensile steel wire mesh with metal bearing plates, (d) High tensile steel wire mesh with isolated reinforced concrete nail heads

During the short history of adopting soil nailing in Sri Lanka, a few failures that relate to facings have occurred. The major failure reported in a mitigation site at Diyagala – Ginigathhena in 2018, could be considered as a typical example of soil mass in the front face sliding off in between the soil nails, as described in FHWA (Federal Highway Administration) (Byrne et al. 1998).

2 Tensile force at the nail head

2.1 *The behavior of soil nail forces*

With the transfer of shear stresses from the sloping ground, the actual soil nail (rebar) inside the grout body is placed under a loading condition

similar to getting pulled from the two ends. As such, the tensile force along the soil nail has a distribution as shown in Fig. 2. This distribution indicates how the nail head load, T_o is related to the maximum tensile force, T_{max} of the soil nail. Many studies and guidelines have discussed this relationship in the context of the performance of facings.

T_{max}= Maximum nail force

T_0 = Tensile force at the nail head
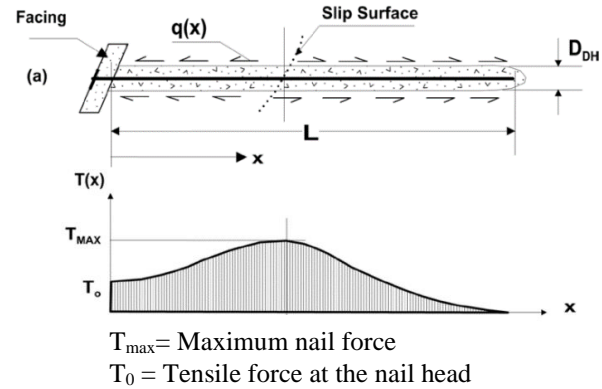
Fig. 2 Distribution tensile force along the soil nail (Lazarte et al. 2015)

2.2 *Design guides for obtaining nail head force*

FHWA (Byrne et al. 1998) present the results of a series of tests carried out on instrumented full-scale soil nail walls at different sites (Fig. 3) with which they propose a method for obtaining the nail head load.
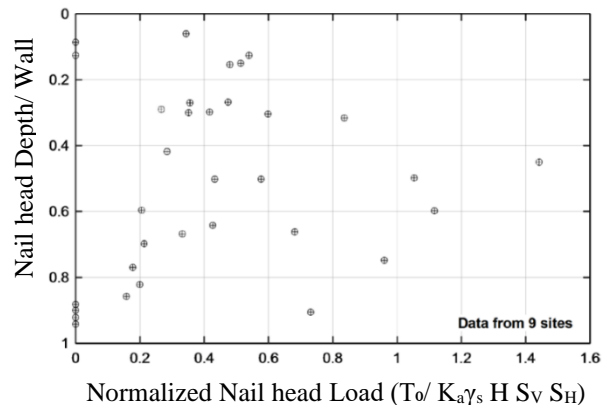
Fig. 3 Normalized Nail head Load (F_F) Distribution (Byrne et al. 1998)

The average normalized nail head loads vary approximately from 0.50 to 0.60. Accordingly, equation (1) can be used for estimating the nail head load:

$$T_0 = F_F K_A \gamma_s H S_H S_V \qquad (1)$$

Where, T_0 is the nail head load. F_F is the normalized nail head load, γ_s is the unit weight of soil, H is the slope height, S_H, S_V are horizontal and vertical nail spacing, and K_A is active earth

pressure coefficient obtained by the Coulomb method.

Similarly, FHWA (1998) proposes an expression for obtaining the maximum nail load, T_{max}

$$T_{max} = 0.65 \, K_A \gamma_s H S_H S_V \qquad (2)$$

FHWA (Byrne et al. 1998) recommends using $F_F = 0.5$ in equation (1) for obtaining T_o. Full-scale tests by (Gaessler and Gudehus 1981) on shotcrete facings, field studies by (Stocker and Riedinger 1990), (Clouterre 1991), and the results of instrumented soil nail walls by (Holman and Tuozzolo 2009) justify this recommendation.

Comparative results to FHWA (Byrne et al. 1998) were achieved by the finite element analysis with FLAC (Fast Lagrangian Analysis of Continua) presented in GEO Report No. 175 (Shiu and Chang 2005). Analyses carried out using different isolated nail head sizes of 400 mm and 800 mm showed values of T_0 / T_{max} varying around 0.55 to 0.7 where T_0 is the nail head load and T_{max} is the maximum soil nail load. Similar to the FHWA (Byrne et al. 1998), the top two-thirds of the nails showed a higher ratio while the lower third showed a lower ratio of T_0 / T_{max} as shown in Fig. 4.
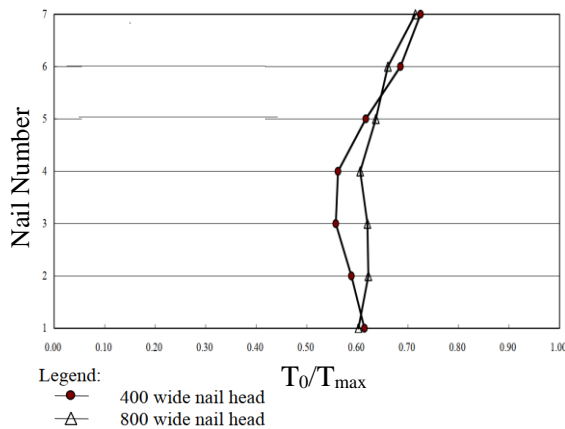
Fig. 4. T_0/T_{max} distribution of isolated nail heads via finite element analysis (Shiu and Chang 2005)

Clouterre (1991) proposed an alternative method for calculating the T_0 / T_{max} ratio for shotcrete facings. This method has been recommended in CIRIA (Construction Industry Research and Information Association) report c637 (Phear et al. 2005) as well and the expression presented is in equation (3).

$$T_o = T_{max}[0.6 + 0.2(S_v - 1)] \qquad (3)$$

Where T_{max} is the maximum nail force, and S_V is vertical soil nail spacing in linear meters

The maximum soil nail force (T_{max}) used in this method could be obtained either from a detailed stability analysis of the soil nailed slope, Method

given in equation (4) proposed by Clouterre (1991).

$$T_{max} = \min\left[\frac{q_s \pi D L_e}{\gamma_d}, \frac{f_y}{\gamma_s}\right] \qquad (4)$$

Where, q_s is skin friction in the resistive zone, D is the diameter of borehole, L_e is soil nail length in the resistive zone, f_y is tensile strength of soil nail, γ_d is Partial safety factor for skin friction, and γ_s is partial safety factor for the tensile strength of the rebar.

2.3 *Determining the suitable method for obtaining the nail head load*

A summary of the methods proposed in international publications is shown in Table 1.

Table 1. Methods in literature for obtaining nail head load

Publication	Calculation method
FHWA, 1998	Recommends 50% of the Coulomb earth pressure ($F_F = 0.5$)
CIRIA c637	Refers to FHWA, 1998
Clouterre, 1991	Calculates T_0/T_{max} based on nail spacing. Varies from 0.6 to 1
GEO Report175	Calculates T_0/T_{max} via FLAC for isolated nail heads. Varies from 0.55 to 0.7.

Accordingly, the discussed approaches could be utilized in the designs as follows.

Case 1:

In cases where precise analysis data are not available, the method given in equation (1) can be directly used for estimating the nail head loads.

Case 2:

In cases where an analysis of stability is carried out, T_{max} can be obtained via the analysis and used to obtain T_0 using equation (3).

2.4 *Application for a case history - landslide rectification at Hakgala*

The methods discussed were applied for the soil nail system at the rectification of Landslide at Hakgala (Kumarage 2021).

The steep escarpments developed due to the landslide has to be stabilized to prevent further propagation. The rectification design of section CS5 (Slope height H = 13 m, Slope angle = 66º) is illustrated in this study. The escarpment section at CS5 had a FOS of 0.811 with the limit equilibrium analysis done using Slope/W software by the Spencer method.

A nailing arrangement in the form of three 16m long and three 12m long 32mm diameter soil nails at an angle of 15° was used in this analysis. Resultant spacing arrangement $S_H = S_V = 2.0$ m increased the Factor of Safety (FOS) up to 1.335 (Fig. 5).

The method described in "Case 2" was adopted to obtain the nail head load. The expressions used in equation (4) can be directly obtained from Slope/W software's "View Object Information" option. The values for nails at each level were obtained from Slope/W output. The value from the bottom-most level (T_{max}=145.34 kN) became the most critical. This T_{max} value and S_V=2 m was used in equation (3) to obtain the nail head load, T_0=116.27 kN.

Additionally, the Slope/W analysis and above calculations were repeated with the same method to evaluate the variation of nail head load under different nail spacings for comparison (Table 2). Although the
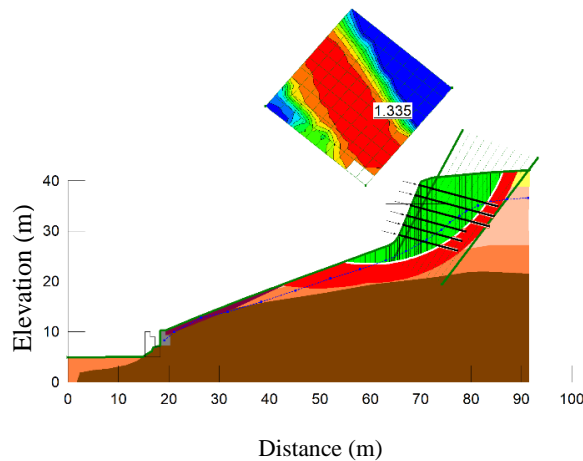
Fig. 5. Stability analysis soil nailing - CS5 – Hakgala

Table 2. Variation of Nail head Load with Nail Spacing

S_V (m)	S_H (m)	FOS	T_{max} (kN)	T_o (kN)
2.5	2.5	1.289	170.85	153.76
2	**2**	**1.335**	**145.34**	**116.27**
1.5	1.5	1.401	99.8	69.86
2.5	2	1.324	170.86	153.77
1.5	2	1.372	164.62	115.23

minimum acceptable FOS (FOS = 1.324) was achieved from the S_V = 2.5 m and S_H = 2m arrangement, it was seen that the nail head load of this arrangement is 32% higher than that of S_V = S_H =2.0 m spacing arrangement. Moreover, the structural integrity of a given facing with an S_V =

S_H arrangement will be greater than that of an $S_V \neq S_H$ arrangement as shown in this study. As such $S_V = S_H$ =2.0 m was preferred to economize the facing design. Nail head load value obtained for $S_V = S_H$ =2.0 m arrangement (T_0=116.27 kN) will be used for facing designs in the later sections.

It could be realized that the method adopted here coupled with a Slope/W analysis to obtain nail head load can yield a facing design to conform to the site-specific geology, morphology as well as groundwater conditions.

3 Design of shotcrete facings

3.1 *The behavior of forces on shotcrete facings*

Shotcrete facing is essentially a reinforced concrete flat slab (wall) that connects the nail heads and is constructed on the slope surface. The nail head loads resulting from the soil movements are distributed across the surface starting from the nail head plate.

The two most critical failure mechanisms are the flexure and the punching shear around the nail head that result from the nail head load. To obtain the earth pressure behind the facing, force equilibrium of the facing in the nail direction is considered (Fig. 6). To account for the non-uniform earth pressure, the factor, C_F is generally used.
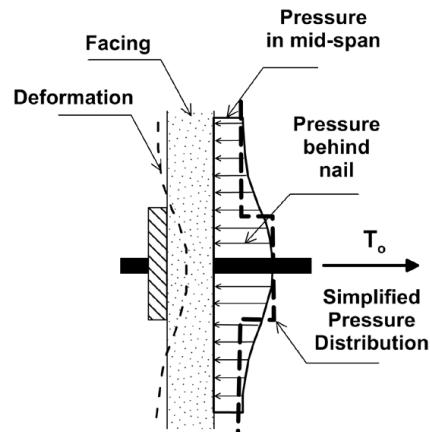
Fig. 6. Soil pressure acting behind the facing (Byrne et al. 1998)

3.2 *Guides for designing shotcrete facings*

FHWA (Byrne et al. 1998) CIRIA c637 (Phear et al. 2005) and Clouterre (French National Project Clouterre 1991) are the major publications where shotcrete design methods are presented.

Both FHWA (Byrne et al. 1998) and CIRIA c637 (Phear et al. 2005) present expressions for obtaining flexural resistance and punching shear resistance of full shotcrete facing modeling it as a

non-uniformly loaded 2-way spanning continuous slab.

FHWA manual (Byrne et al. 1998), assumes a non-uniformly loaded 2-way spanning continuous slab to develop expressions for the structural resistance of shotcrete. Factor C_F is used to account for the non-uniform earth pressure.

The flexural resistance of full shotcrete facing, R_{FF} is given in FHWA (Byrne et al. 1998) as the minimum of:

$$R_{FF} = C_F \times (m_{vm} + m_{vn}) \times \left(\frac{8S_H}{S_V}\right)$$

$$R_{FF} = C_F \times (m_{hm} + m_{hn}) \times \left(\frac{8S_V}{S_H}\right) \qquad (5)$$

Where, S_V and S_H are vertical and horizontal soil nail spacings, and $m_{vm}, m_{vn}, m_{hm}, m_{hn}$ represents the vertical (v), horizontal (h), moment resistances at nail head (n), and midspan (m).

The moment resistance, m is obtained by:

$$m = \frac{A_s F_y}{b}\left(d - \frac{A_s F_y}{1.7 f_c' b}\right) \qquad (6)$$

Where, A_s is the area of tension reinforcement, F_y is the yield strength of tension reinforcement, b is breadth of section considered, d is effective depth of section considered, and f_c' is compressive strength of shotcrete/ concrete.

Similarly, based on a system with a bearing plate connection as shown in Fig. 7, expressions for punching shear resistance of full shotcrete facing, R_{FP} is presented in FHWA (Byrne et al. 1998) as given below.

$$R_{FP} = V_F \left(\frac{1}{1 - C_S \frac{(A_C - A_{GC})}{(S_V S_H - A_{GC})}}\right) \qquad (7)$$
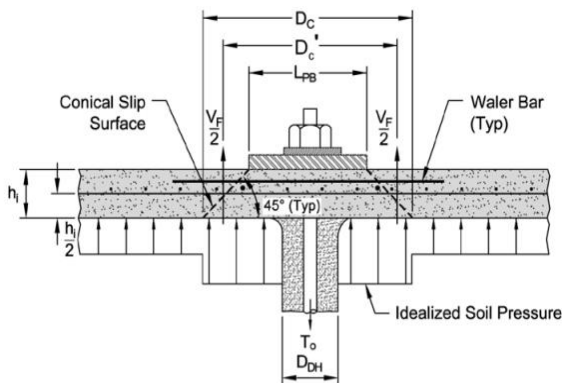
Fig. 7. Punching Shear Mechanism of a Nail head, (Lazarte et al. 2015)

Where internal punching shear strength of a shotcrete facing;

$$V_F = 0.33\sqrt{f_c'}(\pi)(D_C')(h_i) \qquad (8)$$

and,

$$A_C = \pi D_C^2/4$$

$$A_{GC} = \pi D_{DH}^2/4$$

$$D_C' = L_{PB} + h_i$$

L_{PB} = bearing plate length, h_i= facing thickness

The design guides presented in the Clouterre (French National Project Clouterre 1991) also have similar fundamentals to the FHWA (Byrne et al. 1998) method. However, Clouterre recommends considering the soil pressure behind the facing as a uniformly distributed load (udl) and states that it is conservative. For structural calculations, Clouterre recommended using the BAEL 83 (Béton armé aux états limites/ Reinforced concrete at limit states - France) which was the French code of practice regarding the use of reinforced concrete in construction.

CIRIA c637 (Phear et al. 2005) approach also analogizes the facing to a non-uniformly loaded 2-way spanning continuous slab. Force equilibrium of the facing in the nail direction is considered as in the previous approaches. CIRIA c637 presents expressions for flexural resistance of shotcrete facing, R_{FF} which is also using C_F factor to account for nonuniform earth pressure is as follows;

$$R_{FF} = C_F \times n \times S_H \times S_V \qquad (9)$$

Were, the load per unit area of shotcrete;

$$n = \min\begin{bmatrix} \frac{m_{vn}}{\beta_{sx} \times l_x^2} & or & \frac{m_{vn}}{\beta_{sy} \times l_x^2} \\ \frac{m_{hm}}{\beta_{sx} \times l_x^2} & or & \frac{m_{hm}}{\beta_{sy} \times l_x^2} \end{bmatrix} \qquad (10)$$

β_{sx} and β_{sy} can be obtained from Table 3.14 of BS 8110: Part 1. l_x would be the smaller of the horizontal nail spacing and the vertical nail spacing. The ultimate moment resistance, m, is proposed to be obtained from clause 5.3.2.3 of BS 5400 part 4.

Similarly, expressions for punching shear resistance of full shotcrete facing, R_{FP} is presented in CIRIA c637 (Phear et al. 2005), based on BS 5400: Part 4:1990:

$$R_{FP} = [4 \times \xi_s v_c \times (L_{BP} + h) \times d]/(1000) \qquad (11)$$

and the ultimate shear strength of concrete, v_c:

$$v_c = \frac{0.27}{\gamma_m}\left(\frac{100 A_s}{b_w d}\right)^{1/3}(f_c')^{1/3} \qquad (12)$$

Where, (f_c') is concrete compressive strength, (h) is facing thickness, (L_{BP}) is the bearing plate

length, and (d) is the effective depth of the section;

and the depth factor,: ξ_s

$\xi_s = (500/d)^{1/4}$ or 0.70 ; whichever is greater

A summary of the methods for shotcrete design proposed in publications is shown in Table 3.

Table 3. Approaches for shotcrete design

Publication	Calculation approach
FHWA, (1998)	Non-uniformly loaded 2-way continuous slab. Allowable limit design.
CIRIA c637 (2005)	Non-uniformly loaded 2-way continuous slab (refers to BS 5400 part 4). Allowable limit design.
Clouterre, (1991)	Uniformly loaded continuous 2-way spanning slab. Refers to BAEL83

All 3 approaches rely on the same basic principle. The CIRIA c637 (Phear et al. 2005) refers to British standards. Nevertheless, the method used to calculate the ultimate resistance moment and ultimate shear strength of concrete in CIRIA c637 (Phear et al. 2005) isn't based on BS 8110. As such, as a part of this study, a new set of calculations for the structural design of shotcrete based on Clause. 3.7, Design of flat slabs in BS 8110:1997: Part 1 was presented. This closely resembles the loading mechanism of shotcrete facings. With this, the designer can obtain the reinforcement requirements based on the nail head loads.

3.3 *Application of shotcrete design approaches for a case history*

Continuing from nail head load calculations in section 2.4, analysis was done to assess the applicability and requirements of shotcrete facing for section CS5 in the Hakgala Landslide mitigation project. Accordingly, the method recommended in CIRIA c637 (Phear et al. 2005) and modified according to BS 8110:1997: Part 1 was used to determine the structural requirements against flexure and punching. Additionally, the facing requirements for alternative nail spacings were also calculated and the results are tabulated in this proved that a shotcrete facing with a practicable structural arrangement can be used in the CS5 area. The maximum nail spacing (either vertical

Table 4. Shotcrete designs for alternative nail spacing

S_V (m)	S_H (m)	T_{oULT} (kN)	Facing thickness (mm)	Main R/F	Bearing plate size (mm)
2.5	2.5	153.76	175	2Y16	175x175
2	**2**	**116.27**	**150**	**2Y16**	**200x200**
1.5	1.5	69.86	125	2Y10	200x200
2.5	2	153.77	175	3Y16	175x175
1.5	**2**	**115.23**	**150**	**2Y16**	**150x150**

or horizontal) was found to govern the structural requirement of the spacing. As such, using the $S_V = S_H$ arrangement could be recommended as stated in section 2.4.

In addition to BS 8110 modified method, the FHWA (Byrne et al. 1998), and the CIRIA c637 (Phear et al. 2005) methods were used for the calculation of nail head resistance, R_n (lower of flexural, R_{FF} and punching, R_{FP} resistance values) at each $S_V = S_H$ nail spacing arrangement (Fig. 8).

The ultimate nail head load values have also been plotted to better visualize the design requirement at each spacing.
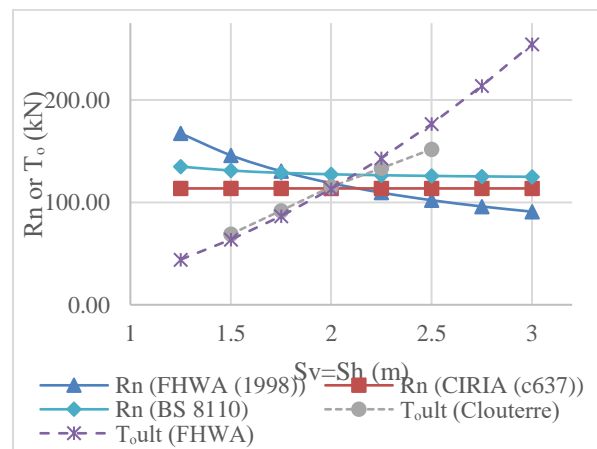
Fig. 8. Nail head resistance, R_n of different methods, and $T_o$ult vs spacing at CS5 of Hakgala landslide mitigation

From this final comparison, it was seen that the three methods produced similar R_n values throughout the spectrum.

From further comparisons, it was seen that the punching shear resistance is governing the structural requirement and the punching resistance is more sensitive to the thickness and around the nail head. Thus, shotcrete facing that has increased thickness at the nail head area could be highly efficient.

4 Design of grid beam facings

4.1 *The behavior of forces on grid beam facings*

Grid beams are systems of reinforced concrete beams constructed across the surface of the slope and connects the nail heads. The main difference between shotcrete and grid beam is that shotcrete is transferring the loads throughout the whole slope face whereas grid beam limits the load transfer to the beam width. Therefore, steel meshes are typically installed along with the grid beam systems to prevent local instabilities between the grids.

Flexure or shear resulting from the nail head load are the most critical failure mechanisms. As in shotcrete, the equilibrium of facing in the nail direction is considered to obtain earth pressure behind facing.

4.2 *Guides for designing grid beam facings*

A limited number of methods for grid beam designs are available in the literature. Japanese guides on grid beam designs weren't available to be found in the English language during this study.

HKIE (Hong Kong Institution of Engineers) report (HKIE and GEO 2013) presents a method where the beam is treated as a simply supported beam with a UDL for the structural design. However, the HKIE method is based on the Hong Kong code of practice (Building Department HK 2013). Accordingly, in this study, procedures for calculating the structural design of grid beams have been presented based on BS 8110:1997: Part 1, Clause. 3.4, Design of Beams. The structural calculation for flexure, checks for $A_{s(req)} < A_{s(prov)}$ requirement and $A_{s(min)} < A_{s(prov)}$, shear design, minimum shear reinforcement A_{sv} are checked.

Grid beam design methods have been developed in this study by modifying the Shotcrete design methods in FHWA (Byrne et al. 1998) and CRIA c637 (Phear et al. 2005). The accuracy of these methods was compared against HKIE (HKIE and GEO 2013) method.

4.3 *Application of grid beam design approaches for the case history*

Continuing from section 2.4 analysis has been carried out to access the applicability of a grid beam facing for the Hakgala Landslide mitigation project's CS5 area using the modified method which is based on the BS 8110:1997: Part 1 Clause. 3.4. Additionally, the same method was used to assess the grid beam design at different nail spacings and the results are tabulated in Table 5.

Table 5. Grid beam designs for alternative nail spacings

S_V (m)	S_H (m)	T_{oULT} (kN)	Beam size (mm)	Main R/F	Shear R/F
2.5	2.5	153.76	250x250	4Y16	R10@150mm
2	**2**	**116.27**	250x250	**4Y12**	R10@150mm
1.5	1.5	69.86	200x200	4Y10	R10@200mm
2.5	2	136.69	250x250	4Y16	R10@150mm
1.5	**2**	**115.23**	250x250	**4Y12**	R10@150mm

The structural arrangement suggests that a grid beam system is also applicable in the CS5 area. As in shotcrete facings, it is highly recommended to use a $S_V = S_H$ arrangement to economize facing requirements. In addition to this, to account for local instabilities, the requirements of a flexible steel mesh facing along with the grid beams will be also assessed in section 6.

5 Isolated nail head systems

Isolated nail heads (Pillows) are essentially concrete pads that distribute nail head load onto the slope surface. The load transfer of pillows could be analogized to pad footings of a building. Bearing failure of the slope becomes the critical failure mode. Design of isolated nail heads has been extensively discussed in GEO report 175 (Shiu and Chang 2005) using finite element modeling, as well as in CIRIA c637 (Phear et al. 2005) which proposes an empirical formula called the lower-bound method. Both methods produce comparable results.

The expressions presented in the Lower bound method are as follows:

$$a_{req} = \left(\frac{T_o}{\eta}\right)^{\frac{1}{3}} \tag{13}$$

$$\eta = \frac{\gamma(1 - r_u)\tan\beta\, e^{3\left(\frac{\pi}{4} \frac{\phi'}{2} + \delta\right)\tan\phi'}}{2\cos\left(\frac{\pi}{4} + \frac{\phi'}{2}\right)(1 - \sin\phi')} \tag{14}$$

Where;

a_{req} Length & width of the nail head required

T_o Nail head load

γ Unit weight of soil

r_u Pore-water pressure ratio

β Slope angle

ϕ' Effective angle of friction resistance

δ Angle of the soil nail

Substitute values for Hakgala CS5 area in equation (14):

$$\eta = \frac{18(1-0.5)\tan(66)e^{3\left(\frac{\pi}{4}\frac{28}{2}+15\right)\tan 28}}{2\cos\left(\frac{\pi}{4}+\frac{28}{2}\right)(1-\sin 28)}$$

$$\eta = \frac{123.68}{0.55} = 226.31$$

Equation (13)

$$a_{req} = \left(\frac{116.27}{226.31}\right)^{\frac{1}{3}} = 800 \, mm$$

This calculation revealed that a pillow size of 800 mm x 800 mm is necessary to resist the obtained nail head load at the CS5 area. This size requirement makes pillows less appealing due to the excess weight induced by the facing onto the nail.

6 Design of flexible structural facings

Flexible structural mesh facing coupled with grid beams, pillows, and/ or bearing plates that promote vegetation are preferred over shotcrete facings in Sri Lanka because of the ability to dissipate pore water pressures and the appearance that blends with the natural environment.

6.1 *The behavior of forces on flexible facings*

In all cases where a hard facing such as concrete blocks (pillow method), or grid beams are used with the flexible facing, the nail head load will not influence flexible facing design. Instead, flexible mesh-facing must resist the out-of-balance force exerted from the soil in-between the nail heads/ beams and transfer it onto the nail head plates. However, in cases where the bearing plate is used as the nail head, the mesh must resist both the punching force from the nail head load as well as the local instabilities because the smaller-sized plates do not generate adequate bearing resistance against the slope.

The mesh product must be chosen based on its resistance against shearing at the nail head/ plate (dependent on wire diameter, strength, and opening size). In addition to the selection of mesh, proper sizing of the head-plate is equally important when designing flexible facings.

6.2 *Guides for designing flexible facings*

CIRIA report c637 (Phear et al. 2005) briefly presented a method for designing flexible meshes. To obtain the out-of-balance force, in the case of shallow slopes, a two-part wedge failure mechanism (Fig. 9) based on HA 68/94 (The Highways Agency 1994) is used. In the case of steeper slopes, a single-wedge failure mechanism based on (Ruegger and Flum 2000) is used. However, it is recommended to calculate forces from both methods and obtain the maximum. The pore water pressure ratio, r_u taken as 0.5 to address the worst case. In these analyses wedge angles θ, θ_1 and θ_2 must be varied to obtain the maximum force induced on the mesh, iteratively.

However, a developed analysis method was not presented therein. Therefore, calculation steps have been developed and presented in this study.
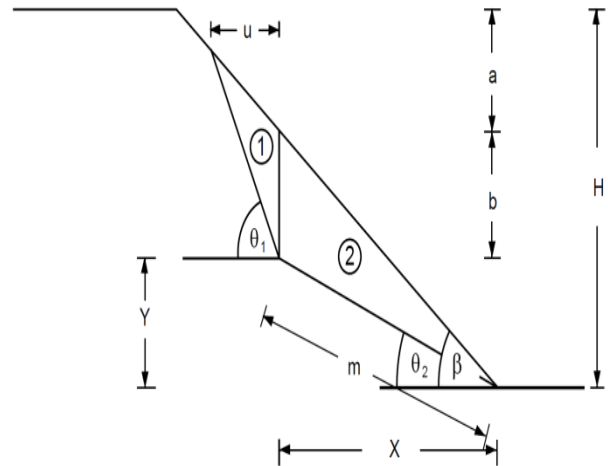
Fig. 9. Mechanism of two-part-wedge failure (Phear et al. 2005)

Cala et al. (Cala et al. 2020) also presented methods to obtain the out-of-balanced forces using two failure modes (One-body and two body), which could be considered more complicated than the CIRIA c637 (Phear et al. 2005) methods (Fig. 10). Groundwater flow parallel to the slope is idealized in these methods instead of using r_u. Features such as pre-tensioning are also included. These have been omitted from the steps developed in this study because such applications are not adopted locally.

presented the maximum vertical spacings between soil nails of a slope that can be left unsupported without using a flexible mesh facing. The chart given therein could be used to have an insight into the requirement of a flexible mesh for the slope in consideration.

6.3 *Application of flexible facing design approaches for the case history*

Analyses were carried out in this study to assess the applicability of a flexible metallic mesh facing over the grid beams to account for local instabilities in the case study; cross-section CS5 in the Hakgala Landslide mitigation project. In this exercise, the soil nail arrangement was considered

as $S_V = S_H = 2$ m similar to the previous applications. All slope and soil properties were the same as in the previous calculation.

6.3.1 *Obtaining the out of balance force*

Spreadsheets were developed in this study to obtain the out-of-balance forces using the four discussed methods and the results are given in Table 6. Initially, the out-of-balance force was calculated for when the metallic meshes are used alongside Grid Beams facings where the height of the two-part-wedge model (H) is equal to the vertical nail spacing, $S_V = 2m$.

Table 6. Summary of out of balance force for Grid Beam method results

CIRIA c637		Cala, et al. 2020	
Two-part wedge	Single wedge	Two body	One body
40. 69 kN	15.91 kN	26.17 kN	24.97 kN

The pore water pressure condition used, $r_u = 0.5$ which is an extreme scenario seems to have caused this approach to produce a larger force (40.69 kN) which will be conservatively considered for evaluating the appropriate mesh for this application.

6.3.2 *Mesh product required to be used with Grid Beams*

The tests carried out on the metallic meshes have revealed higher puncturing resistance than the theoretical values derived from tensile capacity. As such, in cases where testing cannot be carried out locally, the designers could use the manufacturer-tested puncturing resistance values in the designs with modifications to suit head plates used locally. However, the products must carry a reliable product certification such as ETA (European Technical Assessment) in order to confidently use the values presented by the mesh manufacturer in the designs.

Accordingly, the tested strength parameters of the mesh type (3STUTOR Plus 100/2.7, wire strength $= 900$ N/mm^2, wire diameter $= 2.7\,mm$, opening size $= 75\,mm$) was used to assess its adequacy with modifications. The head plate was assumed to be of 200 x 200 mm size which intersects 14 Nos of wires of the proposed mesh.

Published punching resistance of the mesh when the tested plate covers 16 nos of wires $= 72\,kN$

Punching resistance of the mesh which covers 14 nos of wires, P_R $= 63\,kN$

Design value of punching resistance, S_m $= \dfrac{P_R}{1.5}$ $= 42\,kN$

Total punching force induced per nail head, F $= 40.69\,kN \leq \textbf{42 kN}$
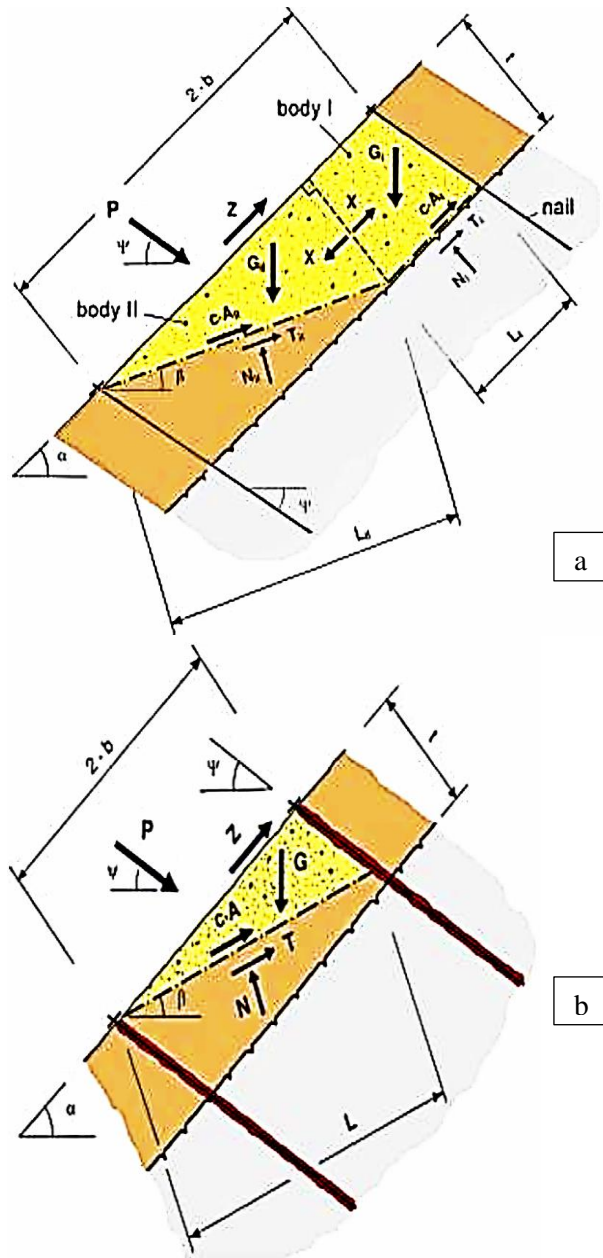
Fig. 10. (a) Two-body (a) One-body failure mechanism (Cala et al. 2020)

The design value of punching resistance, S_m for this combination was 42 kN which is higher than the out-of-balance force, 40.69 kN. As such, it was concluded that the proposed product or equivalent could be used for the protection of local instabilities in-between the proposed grid beam facing.

6.3.3 *Mesh product required to be used with Isolated nail heads (pillows)*

Additionally, the punching shear capacity requirements of a flexible mesh used with an isolated nail head system were assessed. Although the nail spacing considered is the same, because of the zig-zag nailing pattern used in pillow systems, the height of the two-part-wedge failure model (H) for failures in between isolated concrete blocks (pillows) is twice the vertical nail spacing, $2 \times S_V = 4$ m.

For the case history, the out-of-balance force from local instabilities where each facing type is used with the same nail spacing is compared in Table 7.

Table 7. Out of balance forces for pillows and grid beams

Facing Type	Nail spacing $(S_V=S_H)$	Height of failure model (m)	Punching force on the mesh (kN)
Pillows	2	4	**95.19**
Grid Beams	2	2	40.69

It is realized that the mesh used with grid beams was inadequate to be used with isolated nail heads. Mesh type (3STUTOR Plus 100/4.0, wire strength $= 900$ N/mm^2, wire diameter $= 4\,mm$, opening size $= 75\,mm$) that produce a design punching resistance $S_m = 99.17\,kN$ or an equivalent mesh could be used in this application. High tensile options such as TECCO G65/3 with wire strength 1770 N/mm^2, wire diameter of $3\,mm$, and an opening size of $65\,mm$ could also be an alternative for this.

6.3.4 *Mesh product required to be used with Isolated nail heads (Bearing plates)*

The bearing plates must be able to transfer the nail head load onto the slope with the aid of metallic mesh. The adequacy of the mesh and plate to directly withstand the nail head load was assessed in this study. As calculated in section 2.4 the nail head load was, $T_{oULT} = 116.27\,kN$ for the proposed nailing arrangement.

The 3STUTOR Plus 100/4.0 with design punching resistance, $S_m = 99.17\,kN$ or equivalents were found to be inadequate for the bearing plate method. A high tensile option, TECCO G65/3 with $S_m = 120\,kN$ or equivalents were needed for this application.

High-capacity mesh requirement makes the bearing plate facing method a more expensive option compared to other facing types.

7 Cost comparison of facing types

Construction cost is a key factor in choosing the applicable facing type. Comparison in Table 8 was carried out based on the current market prices extracted from contractors' proposals for recent slope mitigation projects in Sri Lanka. Percentiles of the rates for each component of facing, quoted by 8 bidders were used to compute the overall cost.

Full face shotcrete is considerably expensive compared to the pillow and grid beam methods. The metal-bearing plate method which utilizes high tensile wire meshes is the most expensive due to the higher cost of the mesh.

Table 8. Cost per unit area of slope of each facing type

Item	Cost per unit Area (LKR)
Isolated Nail heads (Pillows) with high tensile steel netting with vegetation of the slope in-between the nail heads	**11,500.35**
Grid beams with high tensile netting with vegetation of the slope in-between the grid beams	**12,735.90**
Full face Shotcrete	**14,795.44**
Bearing plate with high tensile wire facing with vegetation of the slope in-between the grid beams	**20,050.00**

8 Performance of different facing types after construction

At the time of conducting this study, the different soil nailing facing types discussed herein have been constructed at sites around Sri Lanka. Therefore, as a means of triangulating the findings of the study, a post-construction performance assessment was carried out using a set of soil nailing sites in Sri Lanka.

Most of the mitigated slopes in Sri Lanka have not been categorized as critical soil nail installations for which dedicated monitoring is necessary to be used. As a result, many of the soil nailed slopes in Sri Lanka currently do not have instrumentation or continuous data to monitor the deformations, loads on soil nails, and pore water pressures which could be used to assess the performance of the facing. Therefore, the assessment of performance was purely based on observation in this study.

To make the approach more systematic, the field inspection criteria were based on the criteria used

in Hong Kong Geoguide 5 for inspecting and maintenance of slopes.

The assessment results of a set of study locations that cover the main facing types discussed in the study have been presented in Section 8.1.

8.1 *Assessment of facing the condition*

8.1.1 *Southern Expressway CH 42+500*

Facing Composition	Full Face Shotcrete
Critical Slope Angle	60 degrees
Critical Slope height	15m
Completion Date	17.07.2015
Date of Assessment	06.03.2020
At the completion of Construction	At Assessment:

Items checked	Condition
Shotcrete facing	Fair

Signs of nonconformity	
Signs of Cracking: Cracks up to 1mm in width can be found at the toe area of shotcrete which could be due to thermal expansion and lack of reinforcement. Cannot be considered detrimental to the slope stability.	**Seepage/ Leaching:** Clusters of large Calthemite deposits caused by water seepage through minor cracks present in Shotcrete. This indicates pore water pressure built up. These cracks may have self-healed due to calcium deposits over time.

Remarks
• In case the leeching is continuous throughout the service life, the facing could get deteriorated over time, corrosion of embedded reinforcement will take place and further cracks could develop.
• In the long run, for sites with excess pore water pressure built up, alternative methods to full-face shotcrete which promotes seepage could be recommended. Alternatively, an effective drainage layer including vertical band drains can be installed behind the full-face shotcrete facings in such conditions.

8.1.2 *Kandy Mahiyangana Road A026 - Location 2*

Facing Composition	Grid Beams with Metallic Mesh & Shotcrete
Critical Slope Angle	60 degrees
Critical Slope height	7m
Completion Date	20.02.2016
Date of Assessment	05.03.2020
At the completion of Construction	At Assessment

Items checked	Condition
Grid Beam and Shotcrete	Good
Vegetation Cover:	Good
Metallic Mesh:	Good

Signs of nonconformity	
Seepage in between facing elements: Seepage is observed in the area of Grid Beam, not necessarily from the horizontal drains. The use of grid beams in this area has permitted free seepage reducing the excess pore water pressure built-up in b-between nail heads.	**Seepage/ Leaching through facing:** Minor signs of seepage at the toe of shotcrete facing at RHS. However, no signs of leaching/ water pressure built up behind shotcrete facing are observed.

Remarks
• Vegetation cover has grown successfully, despite the steep slope angle.
• The selection of Grid Beam for the LHS of the slope has been an exceptional choice considering the amount of seepage observed in the area between nail heads.
• The difference in aesthetic appeal between the two facing types (Grid beam & Shotcrete) can be observed

8.1.3 *Kandy Mahiyangana Road A026 - Location 3*

Facing Composition	Concrete Nail heads (Pillows) with Metallic Mesh
Critical Slope Angle	65 degrees
Critical Slope height	8m
Completion Date	20.02.2016
Date of Assessment	05.03.2020
At the completion of Construction	At Assessment

Items checked	Condition
Concrete Nail heads (Pillows):	Good
Vegetation Cover:	Fair
Metallic Mesh:	Good

Signs of nonconformity
Local instabilities
Minor local slope instabilities could be observed at the RHS side of the nailed area. Soil mass in between the nail head has failed and the debris had slid through the metallic mesh and the slope.

Remarks:
• Vegetation cover has failed to grow as expected on a few steep-sloped spots and, this could also be attributed to the boulder-rich slope surface.
• In the area where the vegetation cover is lacking, local failures or erosion had taken place at the slope surface. This shows the unreliability of pillow facings in instances where the slope surface is steep, jointed, erodible, or embedded with boulders.
• The Coir mesh which had been used to support the growth of vegetation has decayed away at the time of assessment.

9 Conclusion

Choosing the most appropriate soil nail facing meeting the requirements in a given mitigation project is an extremely important task.

Grid beams and full-face shotcrete facings offer the most freedom to achieve a higher value of nail head resistance as well as to more effectively connect the nail heads as a statically indeterminate system. Full-face shotcrete is superior to grid beams, particularly in terms of the ability to resist both nail head loads as well as local instabilities without having to resort to other components. A full-face shotcrete facing must be the preferred choice on slopes where the surface soil is showing a sandy, blocky, or crumbly nature. These slopes are susceptible to erosion and collapsible in the event of water flowing on the slope. The confinement provided by shotcrete throughout the slope face is extremely effective in such circumstances. This should be the first choice for slopes with angles steeper than 65°.

However, the cost of shotcrete is relatively high compared to grid beam and pillow options. If the short drains provided at the facing are not effective pore-water pressure could build up behind the facing. On the other hand, shotcrete may be less appealing aesthetically. The designer must be cautious in this aspect in opting for full-face shotcrete.

Alternatively, using isolated concrete nail head systems with, planting, sodding, or hydroseeding would blend with the natural landscape. However, where nail head loads are larger and the out-of-balance force from local instabilities is high, the required high tensile metallic mesh products would make it uneconomical. For residual soil formations in Sri Lanka, grid beams coupled with non-high tensile mesh systems could be preferred as a cost-effective, structurally superior solution that is aesthetically pleasing.

Based on the finding of this study, a comparison of the applicability of different facing types from different viewpoints is presented in Table 9. This can be used for selecting appropriate facing types for a given slope before proceeding to detailed facing designs.

Table 9. Applicability of different facing types under different design considerations

Consi-deration \ Facing Type	Applicability			
	Grid Beams with Mesh	Full face Shot-crete	Con-crete pillow with Mesh	Bear-ing plate with Mesh
Larger nail head loads	Excel-lent	Good	Fair	Poor
Local In-stabilities	Good	Excel-lent	Poor	Fair
sandy, crumbly surface	Good	Excel-lent	Poor	Poor
Higher ground-water ta-ble	Good	Poor	Fair	Excel-lent
Aesthet-ics	Good	Poor	Good	Excel-lent
Construc-tion Time	Poor	Good	Fair	Excel-lent
Cost*	Good	Fair	Excel-lent	Poor

* a detailed comparison of costs is presented in Table 8.

References

British Standards Institution. (2010). *BS EN 14490:2010 Execution of special geotechnical works. Soil nailing - European Standards. British Standards Institution*, London.

Building Department HK. (2013). "Code of Practice for Structural Use of Concrete 2013."

Byrne, R. J., Cotton, D., Porterfield, J., Wolschlag, C., and Ueblacker, G. (1998). *Manual for Design & Construction Monitoring of Soil Nail Walls*. FHWA.

Cala, M., Flum, D., Rüegger, R., Roduner, A., and Wartmann, S. (2020). *TECCO® slope stabilization system and RUVOLUM® dimensioning method*. AGH University of Science and Technology.

Clouterre. (1991). *Recommendations CLOUTERRE 1991*. Project National Clouterre.

Gaessler, G., and Gudehus, G. (1981). "Soil Nailing - Some aspects of a new technique." *Proceedings of the International Conference on Soil Mechanics and Foundation Engineering*, A. A. Balkema.

HKIE, and GEO. (2013). *Design Illustrations on the Use of Soil Nails to Upgrade Loose Fill Slopes*.

Holman, T. P., and Tuozzolo, T. J. (2009). "Load Development in Soil Nails from a Strain-Gauge Instrumented Wall." ASCE, 25–32.

Hong Kong (China). Geotechnical Engineering Office. (2008). "Guide to soil nail design and construction." Geotechnical Engineering Office, Civil Engineering and Development Dept., The Government of the Hong Kong Special Administrative Region, (7), 97.

Kumarage, B. I. (2021). "A Study of Applicability of Different Facing Types in Soil Nailing." MEng Thesis Submitted to University of Moratuwa.

Lazarte, C. A., Robinson, H., Gómez, J. E., Baxter, A., Cadden, A., and Berg, R. (2015). *Soil Nail Walls - Reference Manual*. FHWA.

Ng, F., Lau, M., Shum, K., and Cheung, W. (2007). *GEO Report No. 222 - Review of Selected Landslides Involving Soil-Nailed Slopes*. Geotechnical Engineering Office, Hong Kong.

Phear, A., C Dew, B Ozsoy, NJ Wharmby, J Judge, and AD Barley. (2005). *CIRIA C637 - Soil nailing: best practice guidance*.

Ruegger, R., and Flum, D. (2000). *Slope stabilization with high-performance steel wire meshes in combination with nails and anchors. Proceedings of the Korean Geotechical Society Conference*, Korean Geotechnical Society.

Shiu, Y. K., and Chang, G. W. K. (2005). "GEO Report No.175 - Soil nail head review." Geotechnical Engineering Office, Hong Kong

Stocker, M. F., and Riedinger, G. (1990). "The bearing behaviour of nailed retaining structures." *Design and Performance of Earth Retaining Structures*, ASCE, 612–628.

The Highways Agency. (1994). *HA 68/94 - Design Methods for the Reinforcement of Highway Slopes by Reinforced Soil and Soil Nailing Techniques*.

MODELLING OF HYDRO-MECHANICAL ALTERATIONS IN FRACTURED COAL CAUSED BY STEPWISE CO_2 INJECTION

K.H.S.M. Sampath[1] and M.S.A. Perera[2]

[1]*Department of Civil Engineering, University of Moratuwa, Sri Lanka*
[2]*Department of Infrastructure Engineering, Engineering Block B, Grattan Street, Parkville, University of Melbourne, Victoria 3010, Australia*

ABSTRACT: The increase of anthropogenic CO_2 level in atmosphere has caused numerous environmental and social issues, forcing researchers to conduct investigations on new CO_2 minimization techniques. Among multiple such techniques, CO_2 sequestration in fractured rock formations such as coal seams has become popular because the process is coupled with coalbed methane (CBM) extraction. However, the process gets quite complicated due to the structural alterations that occur in coal seams upon CO_2 interaction. One of the major drawbacks in the process is the CO_2 adsorption-induced coal volumetric swelling, that causes the fracture permeability reduction. This in turn hinders the further CO_2 injection into coal seam, diminishing the productivity of the overall sequestration process. This study focuses on numerically analyzing and quantifying the hydro-mechanical alterations that occur in fractured coal mass due to stepwise CO_2 injection process. The fractured coal mass is modelled with discrete fracture matrix (DFM) modelling approach and the CO_2 fracture flow, matrix diffusion, adsorption, matrix swelling, and fracture permeability variation are combined through a fully coupled process. The results indicate that, in the first phase of CO_2 injection, CO_2 easily flows through the natural fractures and adsorbs on to coal matrix, causing matrix swelling to some extent. This in fact reduces the existing fracture apertures, while fully closing down some small fractures in the original geometry. The deformed geometry causes completely different/delayed CO_2 flow behaviour in the second phase of CO_2 injection, confirming the fact that the CO_2 sequestration process is significantly affected by the CO_2 interaction-induced rock structural alterations.

Keywords: CO₂ sequestration, coal seam, DFM modelling, hydro-mechanical coupling

1. Introduction

The rapid growth of population and the industrial revolution has caused a significant increase in anthropogenic CO_2 level in the atmosphere, causing a severe environmental damage. The resultant greenhouse gas effect is the major reason for recent environmental problems including climate change, food shortages, spread of deceases and pandemics and desertification of fertile areas. All the countries around the globe are therefore collectively trying to minimize the greenhouse gas effect in every possible aspect. For instance, during the 21st conference of the parties (COP21) which was held on 2015 in Paris, under the United Nations framework convention on climate change (UNFCCC), around 195 countries have come to a public agreement to reduce the CO_2 level in the atmosphere, to maintain the global warming 2°C less than the pre-industrial level (COP21,

2015). While minimizing the further emission of CO_2 from possible sources, studies are underway to find techniques to mitigate the already-released CO_2 in the atmosphere.

Among multiple ways of doing this, CO_2 capture and sequestration in underground geological reservoirs has been identified as a viable option, because most of the potential reservoirs consist of huge amount of pore spaces that are ideal for CO_2 trapping (Aminian, 2003). The possible geological reservoirs identified include several sedimentary rock types such as shale, sandstone, siltstone and coal. Among them, coal seams have proven to be a better option, because the natural fracture network of coal (i.e., cleat system) provides easy flow paths for the injected CO_2 to migrate towards the potential adsorption cites. Further, most potential coal seams are saturated with methane – an alternative energy source, which can be easily harvested by replacing with the

injected CO_2. This is known as the CO_2-enhanced coalbed methane (CO_2-ECBM) extraction; a technique that is already popular in many countries around the world (Sampath et al., 2017).

Although this seems a viable option, the process is quite complicated due to the complex hydro-mechanical alterations that occur in sensitive coal structure, upon the interaction with injected CO_2. In fact, there are numerous physico-chemical interactions that occur in coal, resulting in adverse modifications in the coal structure, including alterations in coal permeability and strength (J. Q. Shi & Durucan, 2003). This in turn leads to a high-risk of CO_2 back-migration, outbursts, reservoir failures and contaminations, posing a great threat to local habitats. Further, the CO_2 adsorption-induced swelling can close down the natural fracture network of coal, thereby reducing the coal permeability and the CO_2 flow ability through the seam (Pan & Connell, 2007). This has become a major concern in the CO_2 sequestration industry because the reduction in fracture permeability can substantially hinder the CO_2 injectivity into the coal seam and subsequently hamper the efficiency of the overall sequestration process. For an example, Oudinot et al., (2011) observed a huge drop in CO_2 injectivity in the long run, during the Fruitland Coal Fairway CO_2 sequestration project. In fact, they have observed a reduction of injectivity from 7.08×10^4 m^3/day to 1.42×10^4 m^3/day, just after a one year of CO_2 injection.

It is therefore necessary to comprehensively study the complex CO_2 flow behaviour and the associated hydro-mechanical alterations that occur in fractured coal seams. Only the experimental studies are not sufficient to get a clear image, as the observations are highly specific to the tested coal type, due to the heterogeneous and anisotropic nature of coal. A detailed numerical analysis is thereby necessary to understand the underlying complex process and to model the reservoir behavior accurately. This study is focused on modelling the CO_2 flow, adsorption and swelling behaviour of a fractured coal seam during a stepwise CO_2 injection process. The model is developed as a fully coupled hydro-mechanical model using discrete fracture matrix (DFM) modelling approach. The CO_2 injection is modelled as a two-step process and the variations in pore pressure, volumetric swelling, fracture aperture and permeability are analysed in detail.

2. Stepwise CO_2 injection and the resultant hydro-mechanical alterations

Several previous experimental studies suggest that CO_2 interaction causes large alterations in coal structure, affecting the further CO_2 injection into the seam. Hence, this study is initiated to simulate this behaviour. The numerical model was developed with equi-dimensional DFM modelling approach in which a lab-scale geometry was analyzed considering fully coupled CO_2 flow – adsorption – deformation process. If the entire procedure is considered in a practical point of view; initially, when the CO_2 is injected into the lab-scale coal specimen (i.e., a 78 mm x 36 mm sample) with a fully opened fracture network, CO_2 rapidly flows through the fracture network due to its high fracture permeability. Therefore, all the major and interconnected fractures get fully saturated instantly as soon as the injection pressure is applied on the sample boundary. According to experimental experience, this takes only a few seconds. Then, the CO_2 starts to diffuse into coal matrices from the fracture matrix interfaces and adsorb on to potential adsorption sites. Since, all the bounding fractures of a particular coal matrix are fully saturated instantly, CO_2 diffuses into the respective matrix from all the interfaces/boundaries, as shown in Fig. 1. This is a very slow process, compared to fracture flow.

The adsorption of CO_2 onto coal matrices causes coal matrix swelling, causing mechanical deformation and the reduction in local fracture aperture. The reduction in aperture drastically reduces the fracture permeability, as the permeability is dependent on the fracture aperture. In summary, in the 1st CO_2 injection cycle (i.e., 1st simulation phase), CO_2 rapidly flows through the natural fracture network, diffuses, and adsorbs on to coal matrix, causing matrix swelling and fracture permeability reduction. This reduction in permeability due to CO_2 interaction in the 1st phase, causes large flow modifications in the seam, affecting further CO_2 injection into the seam. If a 2nd CO_2 injection cycle is considered, now the coal seam is mechanically altered due to initial CO_2 interaction and hence the flow behaviour would be quite different than that in
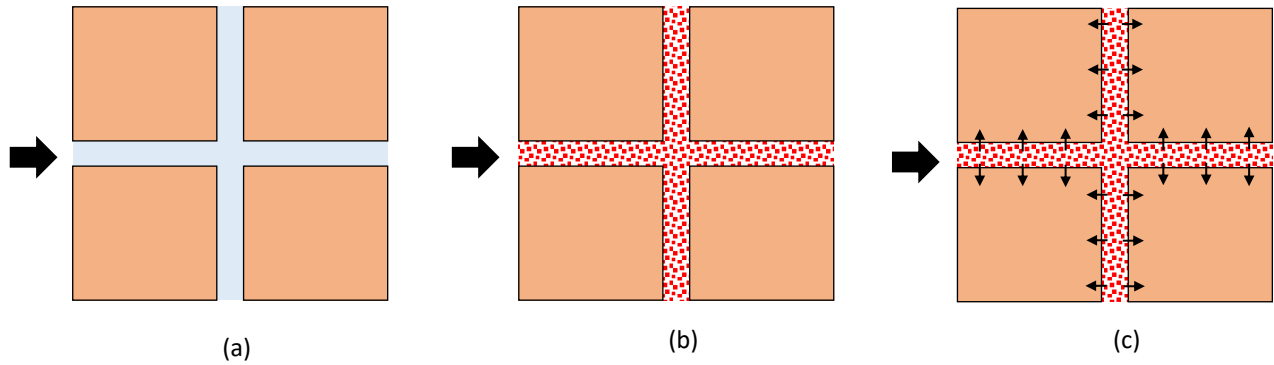
Figure 1 – (a) Initial fracture-matrix geometry, indicating the injection point, (b) fracture network gets saturated as soon as the CO_2 is injected, due to high permeability, and (c) CO_2 starts to diffuse into coal matrices from fracture matrix interfaces.

the 1st CO_2 injection phase. This difference may be dependent on the CO_2 fracture-matrix geometry, pore pressure variation, adsorption and swelling potentials of coal matrices.

3. Numerical modelling approach

The numerical analysis is conducted using COMSOL Multiphysics software package. The lab-scale equi-dimensional DFM geometry is defined such that it consists of 6 matrix blocks and a fully opened, interconnected fracture network. The study consists of two phases: as the 1st phase, CO_2 is injected from atmospheric pressure to 10 MPa pressure and the simulation is run until it the system reaches the full pressure equilibrium. During this time, the original DFM geometry is deformed, and fracture apertures are changed due to sorption-induced swelling, all of which are captured by the coupled mechanical deformation model. Then, the deformed geometry is transferred to the 2nd phase, re-meshed, and the CO_2 injection pressure is increased up to 20 MPa using a stepwise function *(see Fig. 2)*. The CO_2 flow through the deformed geometry and the flow modifications are evaluated and the difference of CO_2 flow in the coal seam between 1st and 2nd injection cycles are highlighted. The complete simulation process is illustrated in Fig. 3.

4. The theoretical approach

A typical coal mass is composed of coal matrices and a natural fracture network which is known as the coal cleat system. This includes two orthogonal fracture types called face cleats and butt cleats. The fracture network controls

the fluid flow in the coal mass through the fracture permeability, whereas the matrix system that includes nano-scale pores governs the diffusion and adsorption process (K. Sampath et al., 2020; J. Shi & Durucan, 2005). The numerical model is developed by assuming the coal structure as a bundle of matchstick geometry, in which the individual cubical coal matrices are separated and bounded by fully void fractures (Ma et al., 2011).
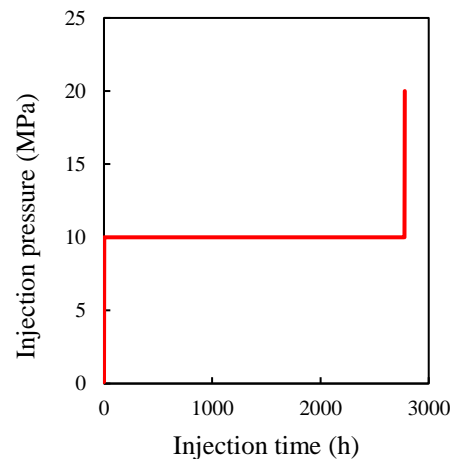
Figure 2 – Stepwise CO_2 injection used in the model.

The fully coupled process implemented in the current numerical model consists of CO_2 flow through the existing fractures, CO_2 diffusion and adsorption to coal matrices, the resultant swelling of the matrices, and the alterations in fracture aperture and therefore the fracture permeability. The separate processes are coupled through mass transfer, effective stress, adsorption/sorption – induced deformation, permeability, and porosity evolution models'
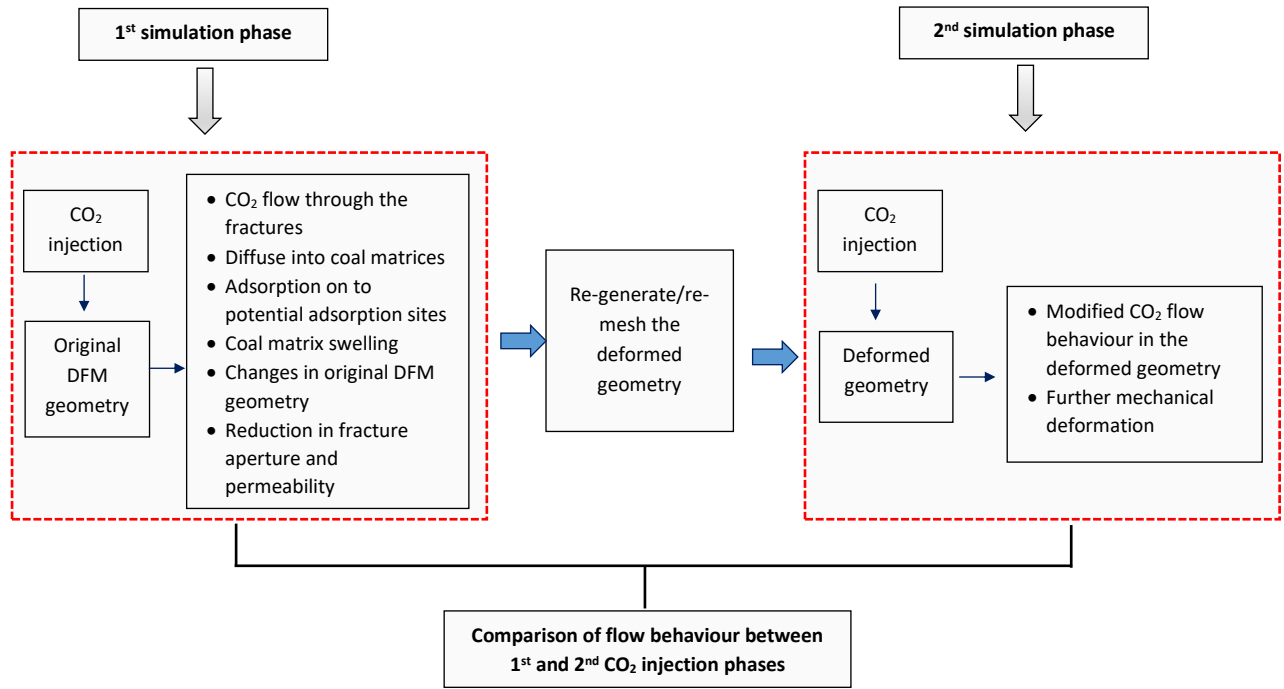
Figure 3 – Complete simulation procedure, indicating the 1st and 2nd CO_2 injection cycles.

formulations incorporated to implement the entire process in fracture and matrix domains in the equi-dimensional DFM geometry, which are explained as follows.

In general, the transportation of injected CO_2 through the fractured coal mass occurs in three ways: CO_2 flow through the fractures in longitudinal direction, CO_2 transfer between fracture and matrix domains at fracture matrix interfaces, and CO_2 diffusion in the matrix domain. The equation that governs the CO_2 flow in fracture domain is defined as:

$$\frac{\partial(\phi_f \rho_{g,f})}{\partial t} + \nabla(\rho_{g,f} q_L) = Q_s \qquad \text{Eq. 1}$$

where, ϕ_f is porosity of fractures, which is equal to one considering fully open condition, $\rho_{g,f}\left(= \frac{M_g}{RT} p_f\right)$ is gas density in fracture domain, p_f is pressure of CO_2 in fractures, R is universal gas constant, M_g is CO_2 molar mass, T is the temperature, and $q_L \left(= -\frac{k_f}{\mu} \nabla p_f\right)$ is CO_2 flow in fractures in the longitudinal directions – defined with the Darcy's law (Darcy, 1856), k_f is permeability of fractures, μ is gas dynamic viscosity, and Q_s is sink/source.

The fracture permeability is defined with the parallel plate law (Witherspoon et al., 1980),

assuming that a particular fracture is formed with two parallel boundaries of adjacent matrix blocks. Hence, fracture permeability can be defined as in Eq. 2, neglecting the roughness of the fractures.

$$k_f = \frac{b^2}{12} \qquad \text{Eq. 2}$$

where, b is local fracture aperture directly measured from the geometry as the orthogonal distance between the corresponding adjacent matrix block walls. Here, the fracture aperture is a function of sorption-induced swelling, effective stress variation and fracture fluid pressure; thus, is coupled with the mechanical deformation equation.

The Fick's second low of gas diffusivity is used to model the CO_2 flow in the fracture domain, assuming that the spatial gradient of mass flux is equal to the temporal derivative of gas content *(see Eq. 3)* (Crank, 1979). Further the total gas content (m) is expanded by considering both free and adsorb gas phases in the matrix domain, in which the adsorbed gas is defined with a Langmuir-type model (Saghafi et al., 2007), as given in Eq. 4.

$$\frac{\partial m}{\partial t} + \nabla . J = 0 \qquad \text{Eq. 3}$$

$$m = \frac{M_g}{RT} \phi_m p_m + (1 - \phi_m) \frac{M_g P_a}{RT} \rho_c \frac{V_L p_m}{p_m + P_L} \qquad \text{Eq. 4}$$

$$\left[\phi_m + (1-\phi_m)P_a\rho_c \frac{V_L P_L}{(p_m+P_L)^2}\right]\frac{\partial p_m}{\partial t} + \left(p_m - P_a\rho_c \frac{V_L p}{p+P_L}\right)\frac{\partial \phi_m}{\partial t} - \nabla(D_g \nabla p_m) = 0 \qquad \text{Eq. 5}$$

where, J is mass flux, ϕ_m is porosity in matrix, P_a is atmospheric pressure, p_m is CO_2 pressure in matrix, ρ_c is coal density, P_L and V_L are Langmuir pressure and sorption constants.

By combining Eq. 3 and Eq. 4, and assuming a constant diffusion coefficient (D_g), the extended governing equation can be derived as given in Eq. 5.

Further, the fluid transfer between fracture and matrix domains is simulated by preserving the pressure and flux continuities at fracture matrix interfaces (see Eq. 6 and Eq. 7). (Tunc et al., 2012).

$$q_{T,f}.n = q_{T,m}.n \quad \text{on} \quad \Gamma_{m,f_1} \text{ and } \Gamma_{m,f_2} \qquad \text{Eq. 6}$$

$$p_f = p_m \quad \text{on} \quad \Gamma_{m,f_1} \text{ and } \Gamma_{m,f_2} \qquad \ldots \ . \text{ Eq. 7}$$

where, Γ_{m,f_1} and Γ_{m,f_2} are fracture matrix interface boundaries, $q_{T,i}$ is transverse flow and $\mathbf{n}$ is unit normal vector.

When modelling the mechanical deformation, the constitutive relationship for matrix deformation is defined as:

$$\varepsilon_{ij} = \frac{1}{2}(u_{i,j} + u_{j,i}) \qquad \text{Eq. 8}$$

Where, ε_{ij} is total strain tensor and u_i is displacement component.

By combining several theoretical formulations, the constitutive relation can be extended as in Eq. 9.

$$\varepsilon_{ij} = \frac{1}{2G}\sigma_{ij} - \left(\frac{1}{6G} - \frac{1}{9K}\right)\sigma_{kk}\delta_{ij} + \frac{\alpha}{3K}p_m\delta_{ij} + \frac{\varepsilon_s}{3}\delta_{ij} \qquad \text{Eq. 9}$$

where, K is bulk modulus, G is shear modulus, $\sigma_{kk} = \sigma_{11} + \sigma_{22} + \sigma_{33}$, α is Biot's coefficient, δ_{ij} is Kronecker delta, $\varepsilon_s = \left(\varepsilon_L \frac{p_m}{p_m+P_L}\right)$ is sorption-induced strain model with Langmuir-type equation, ε_L is Langmuir volumetric strain constant (Cui & Bustin, 2005).

Further, the mechanical equilibrium is defined as,

$$\sigma_{ij,j} + f_i = 0 \qquad . \text{ Eq. 10}$$

where, σ_{ij} is total stress tensor and f_i body force component.

By combining Eqs. 8, 9, and 10, the governing equation for mechanical deformation can be expressed as a Navier-type equation, as given in Eq. 11.

$$Gu_{i,kk} + \frac{G}{1-2v}u_{k,ki} - \alpha p_{m,i} - K\varepsilon_{s,i} + f_i = 0$$
Eq. 11

The fracture stiffness is modelled with the Hooke's law, assuming that the fracture aperture deforms according to the linear elastic behaviour of a spring (Bertrand et al., 2019; Lepillier et al., 2019). Further, the fracture fluid pressure is applied on the fracture surfaces as a surface pressure. Hence, assuming a normal fracture stiffness, the relationship between fracture closure and the fracture normal stress can be expressed as in Eq. 12. Moreover, the contact modelling combined with frictional interfaces is incorporated to model the fracture closure more realistically, in which the contact model uses a no-penetration rule (Agheshlui et al., 2018), and the frictional interfaces assume Coulomb frictional model (Coulomb, 1773).

$$\sigma_n = \sigma_0 + \Delta p_f + K_n\Delta b \qquad \text{Eq. 12}$$

where, σ_n is total normal stress acting on the fracture surface, σ_0 is total stress at initial stage, K_n is normal fracture stiffness, Δp_f is change in CO_2 pressure in fractures, and Δb is fracture closure.

The above mentioned fully coupled model is implemented in the defined DFM fracture geometry and the results are presented in the following section.
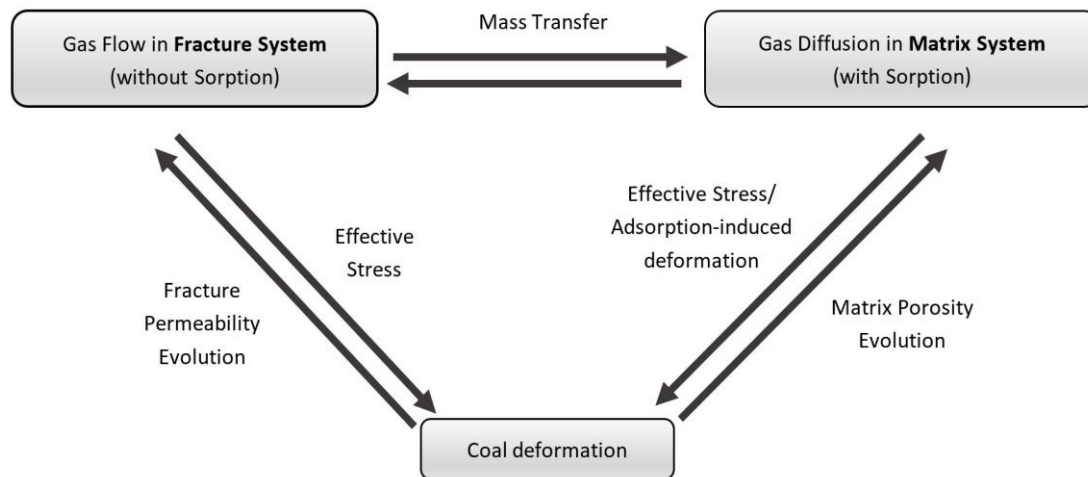
Figure 4 – Schematic of cross-coupling relations among gas flow in fractures, diffusion in matrix and coal deformation

5. Simulation results and discussion

5.1. 1st simulation phase

As the initial geometry, a 2D model with 6 matrix blocks are developed to simulate the CO_2 flow-adsorption-swelling process *(see Fig. 5)*. The fractures are modelled as the free space between matrices, and the fracture apertures are calculated directly from the model geometry as the orthogonal distance between the two fracture boundaries. This enables in calculating the local fracture aperture and its time-dependent variation due to the sorption-induced mechanical deformation. The initial geometry has fractures with initial fracture aperture of 0.7 mm and 0.5 mm throughout the model, simulating natural fracture networks in typical coal seams. Two fracture apertures are defined to clearly distinguish modified flow patterns during each injection cycle. The fracture aperture varies with time, due to the deformation of matrices, where the model simulates the temporal and spatial variation of each fracture aperture. The aperture variation is used to calculate the corresponding permeability of a certain point, which then is coupled with the flow equation – thus the CO_2 flow varies continuously with time, as the fracture permeability varies. The outer boundaries of the blocks are fully constrained *(see Fig. 5)*.

Matrix blocks and fractures act as separate domains with dependent variables of 'p_m' for matrix pressure and 'p_f' for fracture pressure, respectively. Pressure distribution in fractures and matrices are modelled with coefficient form PDE, because the governing equations have to be modified from the conventional ones to account for variable porosity, permeability, diffusion and adsorption. A confining pressure of 25 MPa is applied on the outer boundaries of each matrix block. The CO_2 is injected into one fracture (from left side) as a piecewise function that increases from atmospheric pressure to 10 MPa, within one hour. As shown in Fig. 5, a finer mesh is generated closer to fractures to accurately simulate the process. The 1st simulation is run until the system reach the full pressure equilibrium.

The model parameters used for the analysis are obtained from experimental analyses and several previous researches (Kang et al., 2019; Masoudian et al., 2014; Mazumder et al., 2008; Robertson & Christiansen, 2005; K. Sampath et al., 2020), which are tabulated in table 1. Data of high-rank coal samples (i.e., semi-anthracite, anthracite) are used in the study, as they are the coal types that significantly contribute to CO_2 sequestration and CBM extraction. Since the greater interest of the research is to analyse the localized alterations in the DFM model, the modelling results are discussed based on four points of interest distributed throughout the geometry. In fact, two points are selected from the fracture domain and the other two are selected from the matrix domain *(see Fig. 6)*.
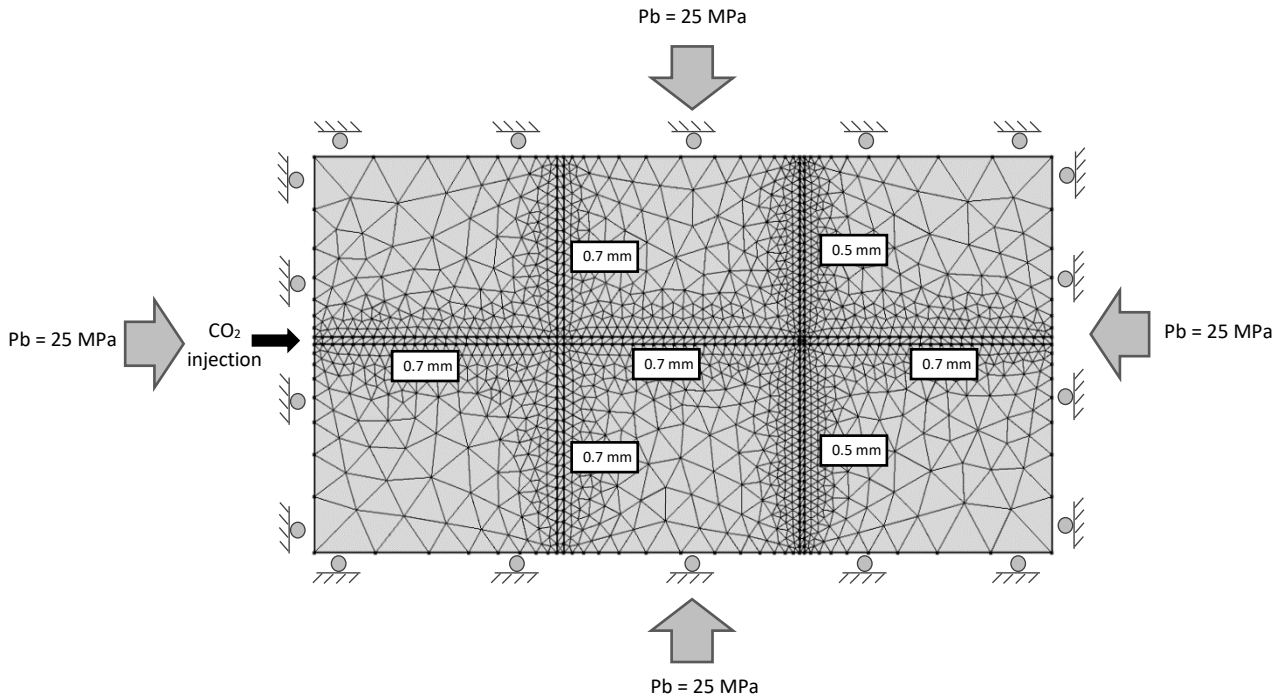
Figure 5 – Initial geometric model used for the simulation, indicating the boundary conditions and meshing.

Table 1 – Modelling parameters used for the analysis

Parameter	Value
Coal density (kg/m^3)	1440
Langmuir sorption constant (m^3/kg)	0.0477
Langmuir pressure constant (MPa)	12.44
Temperature (^{0}C)	40
CO_2 diffusion coefficient (m^2/s)	1.76×10^{-11}
Young's modulus (MPa)	2713
Poisson's ratio	0.339
Atmospheric pressure (kPa)	101.325
Langmuir volumetric strain constant	0.02395
Biot's coefficient	0.8
Density of CO_2 at STP (g/ml)	0.00196
Molecular weight of CO_2 (g/mol)	44.01
Initial matrix porosity	0.0075
Initial fracture aperture (mm)	0.7
Fracture stiffness (GPa/m)	2
Fracture porosity	1
Universal gas constant (J/(mol.K))	8.314
Dynamic viscosity (Pa.s)	1.84×10^{-5}
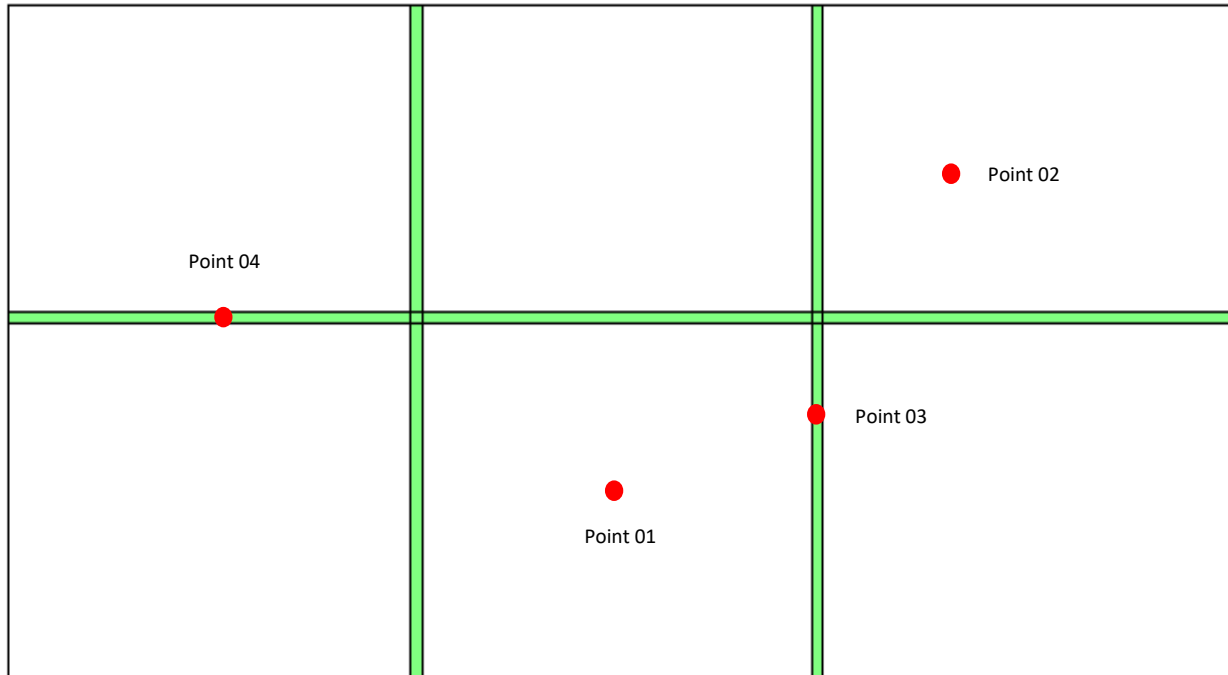
Figure 6 – Points of interest used to analyze the simulation results.

5.1.1. CO_2 pressure distribution in 1st simulation phase

Fig. 7 shows the temporal and spatial distribution of pore pressure in the 1st simulation phase. As mentioned in the numerical modeling approach, the fracture pressure develops rapidly in the lab-scale coal specimen due to high fracture permeability because the fractures are considered as fully void spaces, defining the fracture permeability according to the parallel plate law. Since, initial fractures are having a relatively large fracture aperture in mm-scale, the initial permeability is quite high and therefore the injected CO_2 tend to flow in the fractures rapidly. This is clearly visible in Fig. 7, in which all the natural fractures are fully saturated with the maximum pore pressure (which is equal to the injection pressure of 10 MPa), within the first 0.5% of the simulation period.

This in fact causes the CO_2 diffusion into the coal matrices from all the bounding fracture matrix interfaces, resulting in a gradual pore pressure development in the matrix domain. However, it should be noted that the temporal pressure development in the matrix domain is not as sudden as that in fracture domain, due to the low matrix diffusivity in the matrices. The gradual CO_2 diffusion into matrix results in the

CO_2 adsorption on to potential adsorption sites, causing adsorption-induced swelling, which will be discussed in a latter section

5.1.2. Deformed geometry after 1st simulation phase

Fig. 8 shows the deformed geometry after the 1st injection cycle, when the entire coal specimen is at the pressure equilibrium at 10 MPa. As discussed, the pressure development causes several mechanical modifications, especially the adsorption-induced matrix swelling. The volume expansion of the matrices causes deformation in the fracture network as evident in Fig. 8. In fact, the degree of fracture closure primarily depends on the initial fracture aperture, in which it is noticeable that the fracture with the initial aperture of 0.5 mm has been completely closed down due to matrix swelling, compared to the fracture of 0.7 mm aperture. It should be noted that the fracture aperture at the boundaries remain same due to the fixed restrains defined in the model.

Since the original geometry is deformed significantly due to mechanical alterations in the 1st CO_2 injection phase, the deformed geometry is then re-meshed and transferred to the 2nd phase of the model to simulate the 2nd CO_2 interaction cycle.
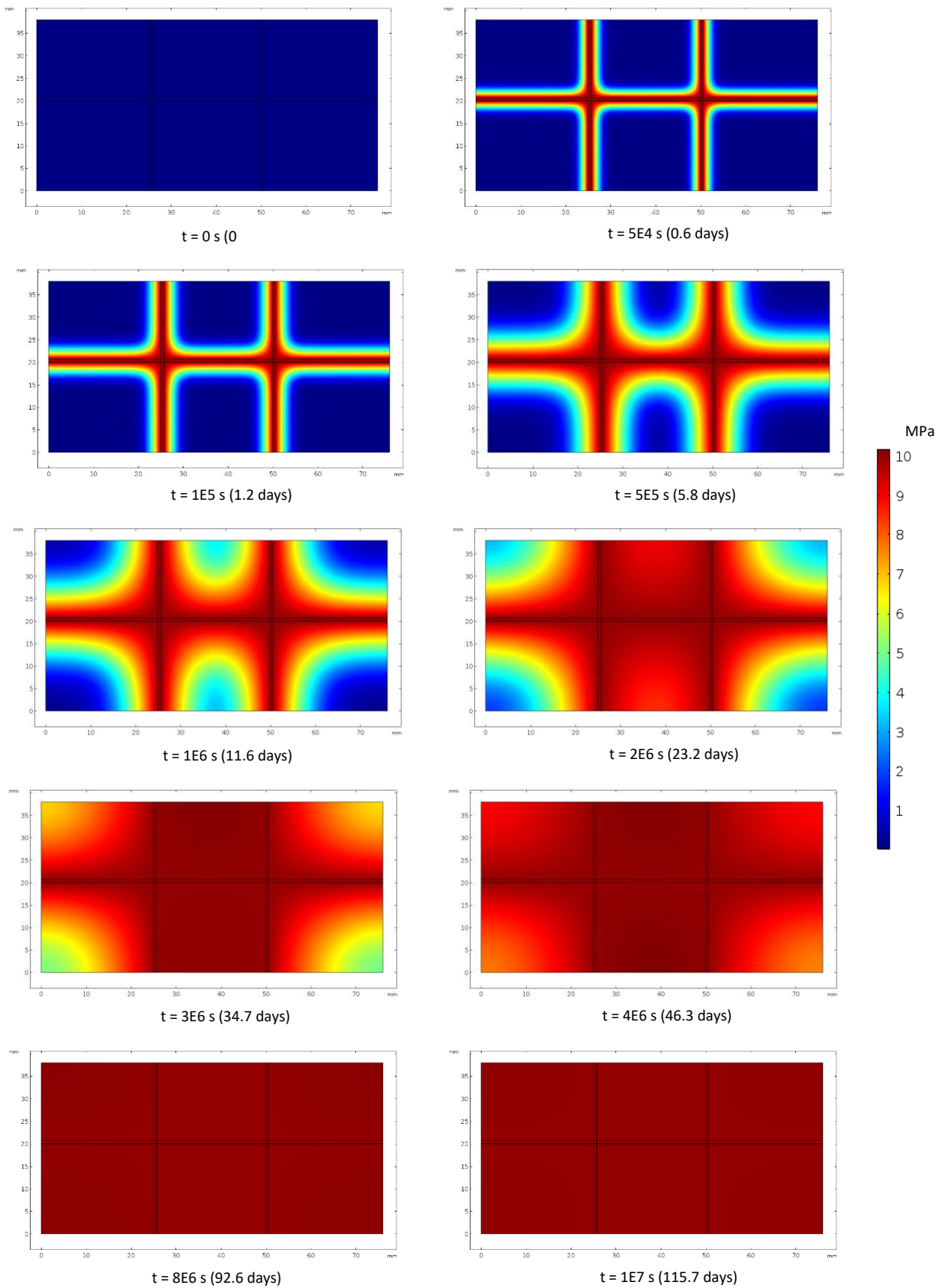
Figure 7 – Temporal and spatial variation of pore pressure during the 1st CO_2 injection phase.
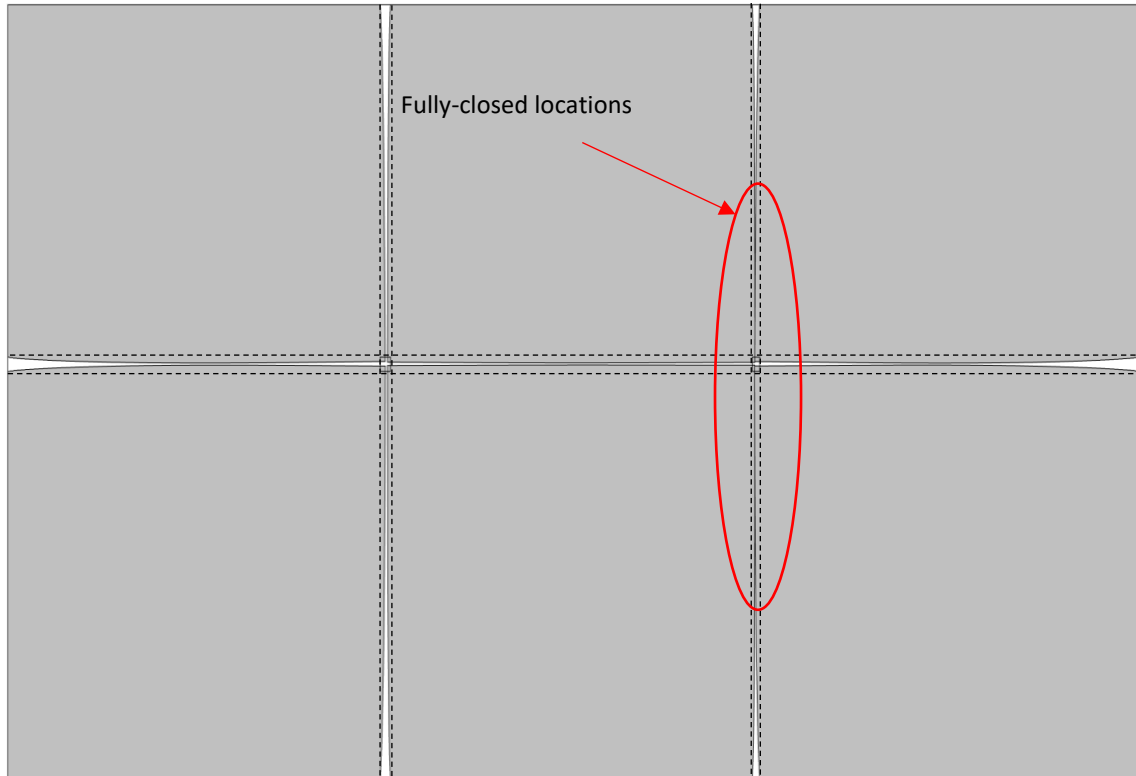
Figure 8 – Deformed geometry after 1st simulation phase, indicating the fracture closure
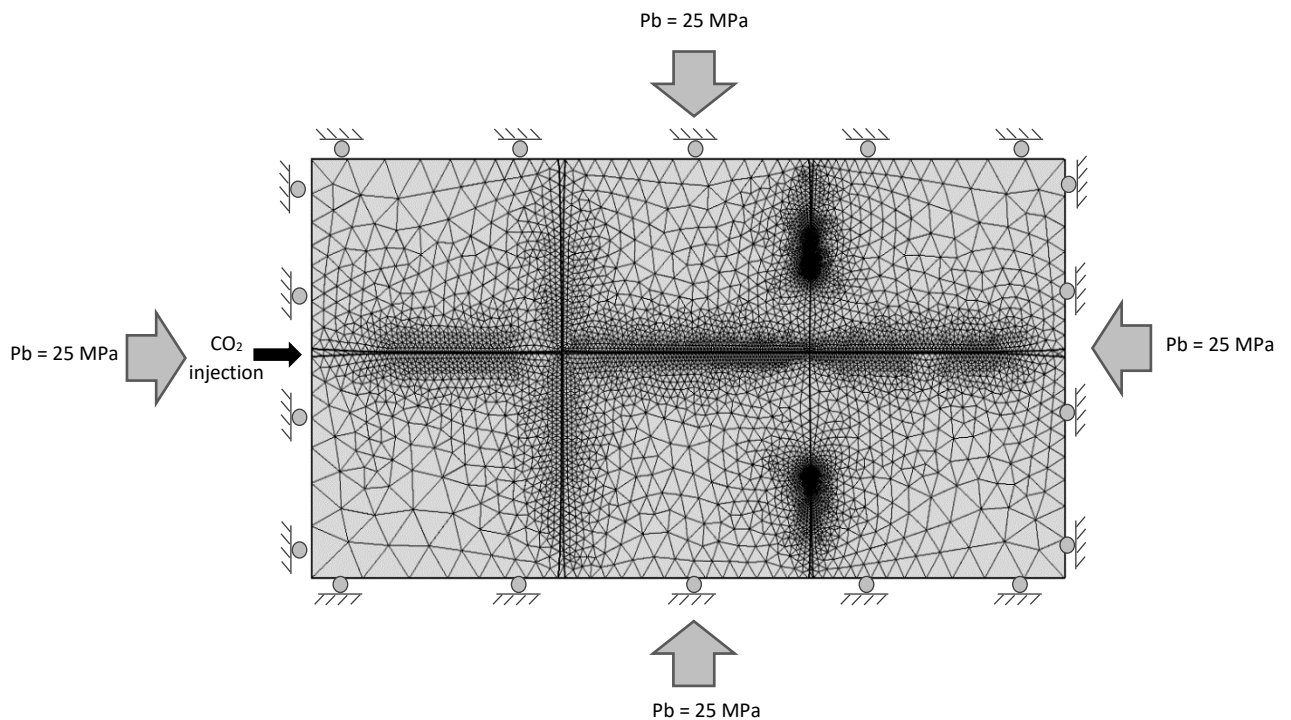
Figure 9 – Deformed geometric model used for the 2nd simulation, indicating the boundary conditions and re-meshing.

5.2. *2nd simulation phase*

The mesh regenerated from the deformed geometry after 1st simulation phase is shown in Fig. 9. It is noticeable that the mesh gets complex since the smaller fractures are fully closed due to matrix swelling and therefore, mesh elements need to be as small as possible to cover the sharp edges. Since, the outer boundaries are fixed, they remain unchanged, and it is notable that 0.5 mm fracture has been partially closed down due to coal matrix swelling. Hence, that fracture is disappeared in the second geometry and the bounding two coal matrices act as a single matrix block, that completely modifies the CO_2 flow behaviour in the 2nd simulation phase. In this phase, the CO_2 injection pressure is increased from 10 MPa to 20 MPa as a piecewise function, as shown in Fig. 2. The initial pore pressure is considered as 10 MPa, as it is already saturated due to initial CO_2 injection. Other boundary conditions remain unchanged and all the parameters, hydro-mechanical theories are similar to the 1st simulation phase

5.2.1. *CO_2 pressure distribution in 2nd simulation phase*

Fig. 10 shows the temporal and spatial distribution of pore pressure in the 2nd simulation phase. It can be seen that the flow behaviour in the 2nd injection cycle is different than that in the 1st cycle. In fact, since 0.5 mm fracture has been closed down at the interconnection, those bounding two matrices act as a single matrix and CO_2 diffuses into the matrix from the primary 0.7 mm fracture. Although, 0.7 mm fracture aperture has been reduced, it has not been fully closed, and the fracture aperture is large enough to provide a rapid fracture flow as in the 1st cycle. However, a part of the 0.5 mm fracture still exists near to the boundary, due to fixed displacement condition, that provides rapid gas flow through that remaining fracture, when CO_2 reaches the particular location. Hence, it is evident that the flow alterations are highly localized in a deformed fractured coal mass and that should be analysed carefully using a DFM modeling approach.

5.3. *Overall analysis of 1st and 2nd simulation phases*

5.3.1. *Matrix and fracture pressure distribution*

This section explains the temporal variation of matrix and fracture pressures, considering the selected points of interest, as shown in Fig. 6. In the 1st phase, CO_2 pressure is increased from atmospheric pressure to 10 MPa and in the 2nd phase it is increased from 10 MPa to 20 MPa. Fig. 11 shows the pressure distribution of two points of interest located in two different locations in the matrix domain, that clearly distinguish the two phases. It can be seen that the system has reached its equilibrium after 1st phases and again increased the pressure after the 2nd injection cycle. As illustrated in Fig. 11, the pressure developments at those two points are not identical but localized in both CO_2 injection cycles. In fact, since point 2 is further away from the fractures, pressure development at point 2 is much slower than that at point 1. This is because the high permeable fractures provide easy flow paths for CO_2 to reach the matrix boundaries, but the low diffusivity in matrix causes a delayed pressure development at locations near to the matrix centers.

In contrast, as already explained the fracture pressure development is quite sudden due to high fracture permeability; therefore, no difference in fracture pressure development between the selected two points of interest (i.e., point 3 and point 4) can be found in the given time frame *(see Fig. 12)*.

5.3.2. *Variation of volumetric strain*

The volumetric strain in the matrix is resultant from a combination of multiple mechanical deformations, including effective stress variation, fracture fluid pressure and adsorption-induced swelling. Fig. 13 illustrates the temporal variation of volumetric strain at two selected points. The volumetric swelling also clearly distinguishes the two phases, where it is noticeable that the swelling in the 1st phase is quite larger than the 2nd phase, probably due the high pressure induced matrix compaction. Further, Langmuir theory suggests that the matrix swelling reaches a plateau at high pore pressure conditions, which is clearly illustrated in the current model.

t = 1E7 s (115.7 days)

t = 1.01E7 s (116.9 days)

t = 1.02E7 s (118.1 days)

t = 1.05E7 s (121.5 days)

t = 1.1E7 s (127.3 days)

t = 1.2E7 s (138.9 days)

t = 1.3E7 s (150.5 days)

t = 1.4E7 s (162.0 days)

t = 1.8E7 s (208.3 days)

t = 2E7 s (231.5 days)
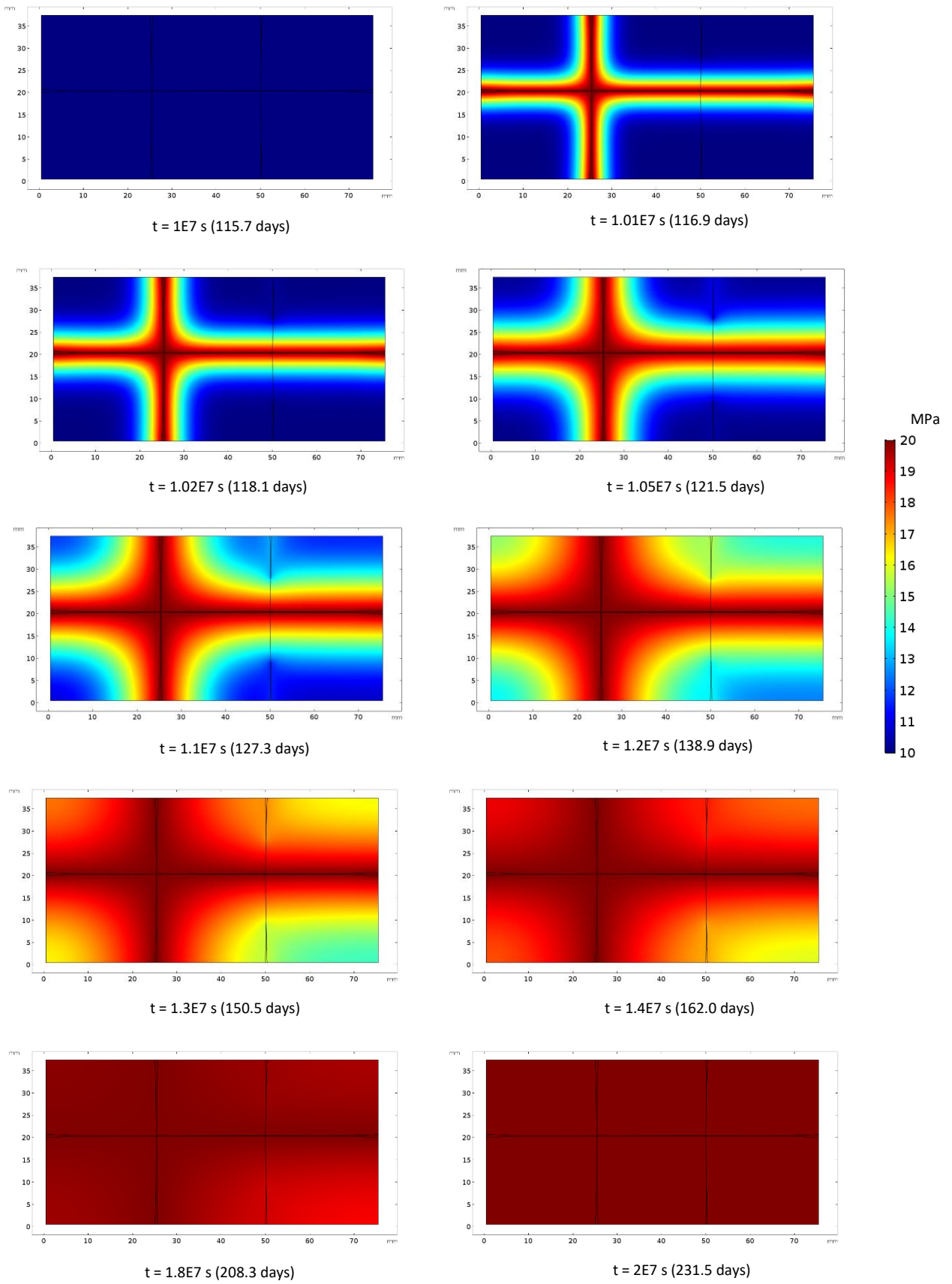
Figure 10 - Temporal and spatial variation of pore pressure during the 2nd CO_2 injection phase.
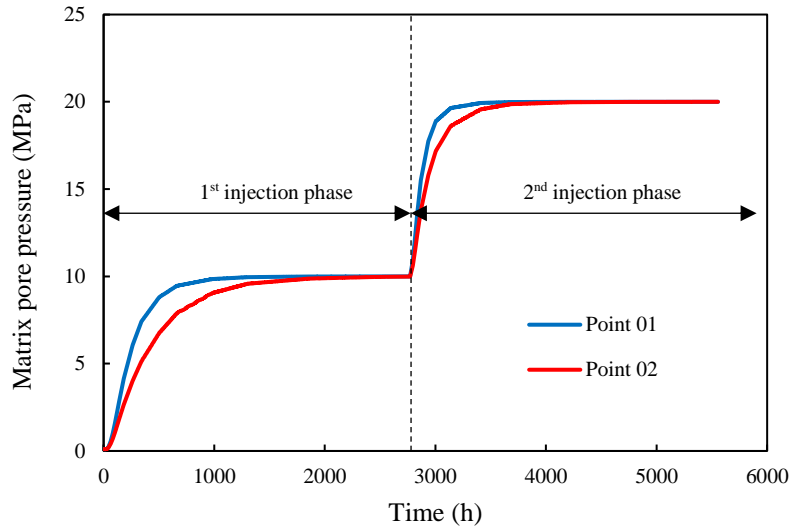
Figure 11 – Variation of matrix pressure distribution with time.
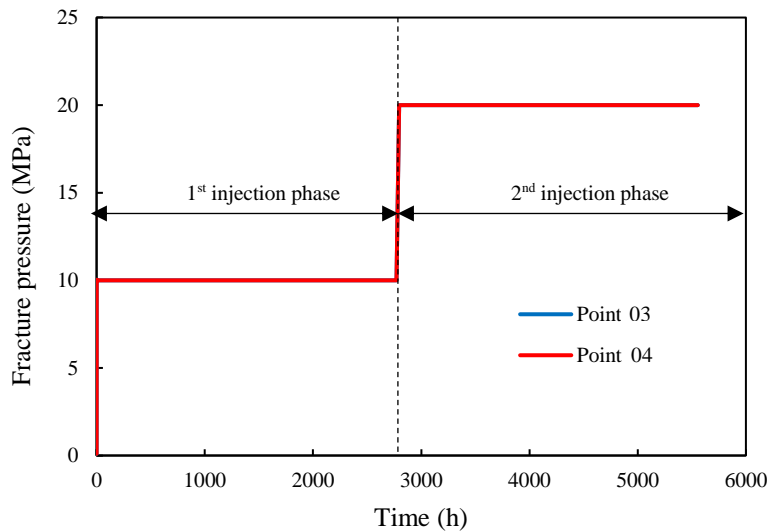
Figure 12 – Variation of fracture pressure distribution with time.

It is noticeable that volumetric swelling at point 02 is less than that of point 1 because point 2 is much closer to the fixed boundary that restrains the deformation. Moreover, Fig. 13 (b) shows the variation of volumetric strain with time in log scale, that clearly shows the shrinking of the coal matrix at the beginning due to the applied fracture pressure and confining pressure on the matrix boundaries. However, with time, the adsorption-induced matrix swelling becomes predominant, surpassing the shrinkage – thus the overall matrix has been swelled significantly at the final pressure equilibrium, which can close down the fractures and reduce the fracture permeability. This is further discussed in the following section, in which the variation fracture aperture in presented.

5.3.3. *Variation of fracture aperture and fracture permeability*

Fig. 14 shows the fracture aperture variation with time at point 03 and 04, which depicts that fracture aperture has been reduced with time due to matrix swelling and leveled off when reaching the equilibrium. The internal figure highlights the aperture variation at the very beginning of the CO_2 injection, which clearly illustrates that the apertures are slightly increased at the beginning due to the applied CO_2 pressure on the fracture boundaries. However, this is overcome by the matrix swelling, which in turn reduces the apertures at
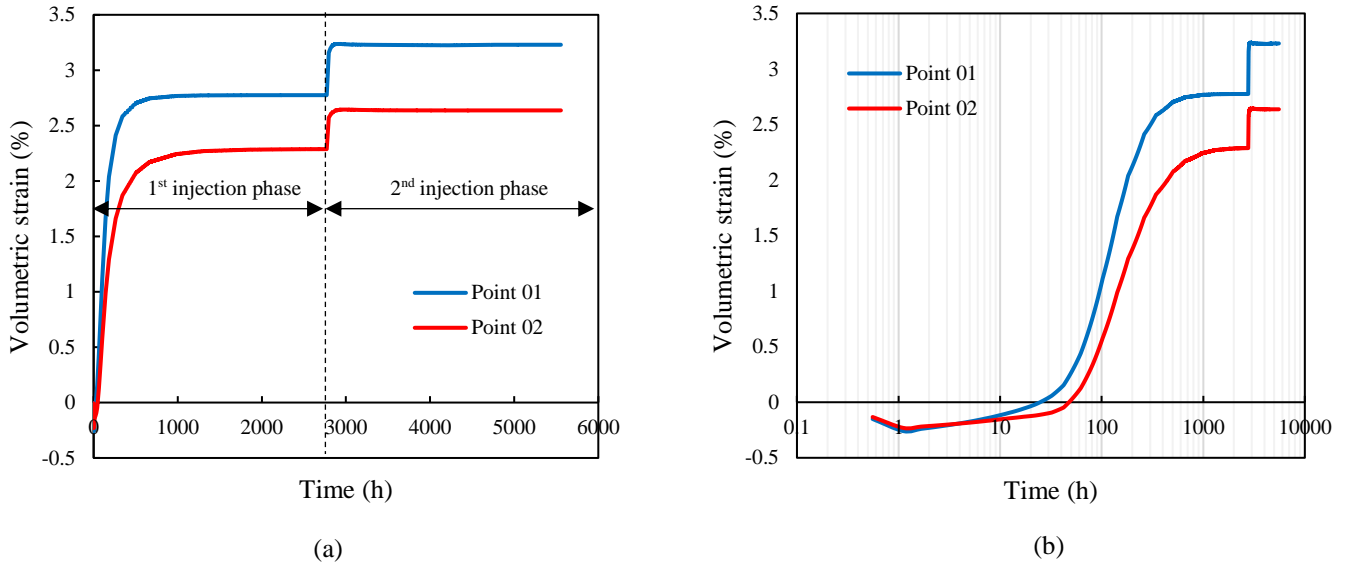
Figure 13 – Variation of volumetric strain with time; (a) time axis in normal scale and, (b) time axis in log scale, highlighting the initial shrinkage.

the pressure and swelling equilibriums. As apparent from the figure, due to initial smaller fracture aperture and high swelling potential of bounding coal matrices, the fracture at point 4 has been fully closed down during the interaction. As can be seen, when the two-fracture surfaces get into contact, the determined aperture remains at zero, which shows no overlapping between two fracture surfaces, confirming the validity of the contact models with no penetration rule. This aperture reduction can significantly influence the flow behaviour in the coal mass.

Further, the fracture aperture variation shows a large reduction in the 1st phase and a small reduction in the 2nd phase, due to the small volumetric swelling that occurred at larger pore pressures. Importantly, the fully closed fracture in the 1st phase (i.e., point 3) remains fully closed, as there is no room for further fracture closure. However, the fracture aperture corresponding to point 4 shows two closure steps related to two injection cycles, confirming that further CO_2 injection causes added modifications in the fractured coal geometry. This in turn may significantly affect the CO_2 injection process, probably causing a less CO_2 injection efficiency.

Since the fracture aperture reduces with the matrix deformation, the fracture permeability also reduces, because the permeability is determined as a function of aperture at the corresponding locations *(see Fig. 15)*. As

illustrated in the figure, when the fracture is fully closed down, the fracture permeability becomes zero, which would completely block the flow through that fracture and make localized flow modifications.

5.3.4. Variation of contact pressure

The numerical analysis includes contact pressure development incorporating no-penetration rule, at which the two fracture surfaces get in contact during the deformation. As evident from previous explanations, some small fractures get fully closed during the 1st CO_2 injection cycle and other fractures also get closed to some extent due to further swelling of the matrices. Fig. 16 illustrates the temporal variation of contact pressure development at one fully closed fracture. It clearly shows that the contact pressure remains zero up to a certain time until the two fracture surfaces get in contact, and then gradually increases with further swelling. This comes to a plateau at the end of 1st CO_2 injection cycle due to the intermediate pressure equilibrium, but then increases again rapidly with the further CO_2 injection. It is noticeable that the magnitude of developed contact pressure at the 2nd cycle is not as high as that at the 1st CO_2 cycle, probably due to the high pore pressure-induced matrix compaction.
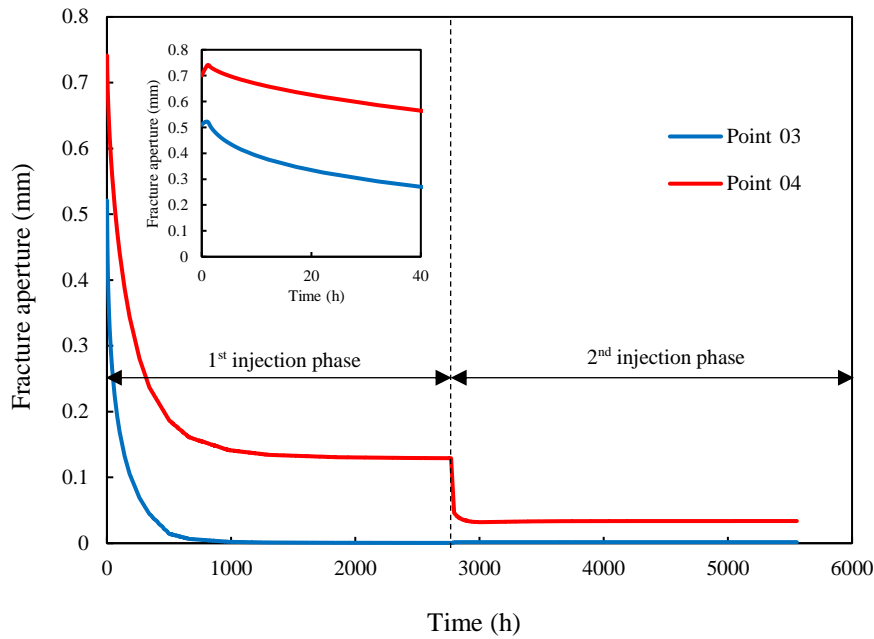
Figure 14 – Variation of fracture aperture with time
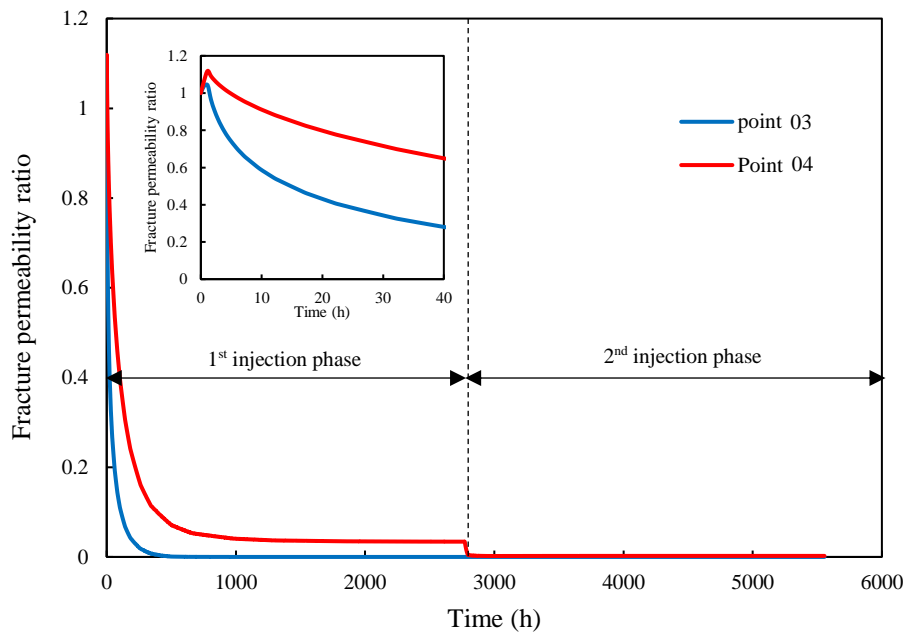
Figure 15 – Variation of fracture permeability with time.

5.3.5. *Further deformed geometry after 2ⁿᵈ simulation phase*

Finally, Fig. 17 shows the further deformed geometry after both 1st and 2nd CO₂ injection cycles are completed and the system is under pressure equilibrium at 20 MPa pore pressure. Interestingly, as highlighted in the figure itself, more fractures are closed at this stage when compared to the previous stage, visually confirming that further CO₂ injection certainly causes added structural modifications in the fracture coal geometry. As the next step, this geometry can be re-meshed, and a 3rd injection cycle can be modelled to assess further structural modifications. However, the complex geometry with very sharp edges may affect the meshing process, increase the computational burden and probably hinder the results accuracy.
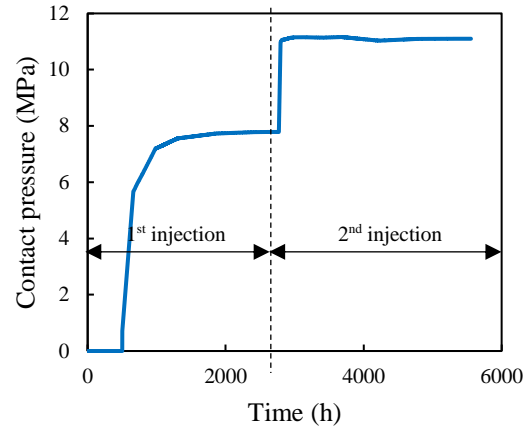
Figure 16 – Variation of contact pressure development of a fully closed fracture with time.
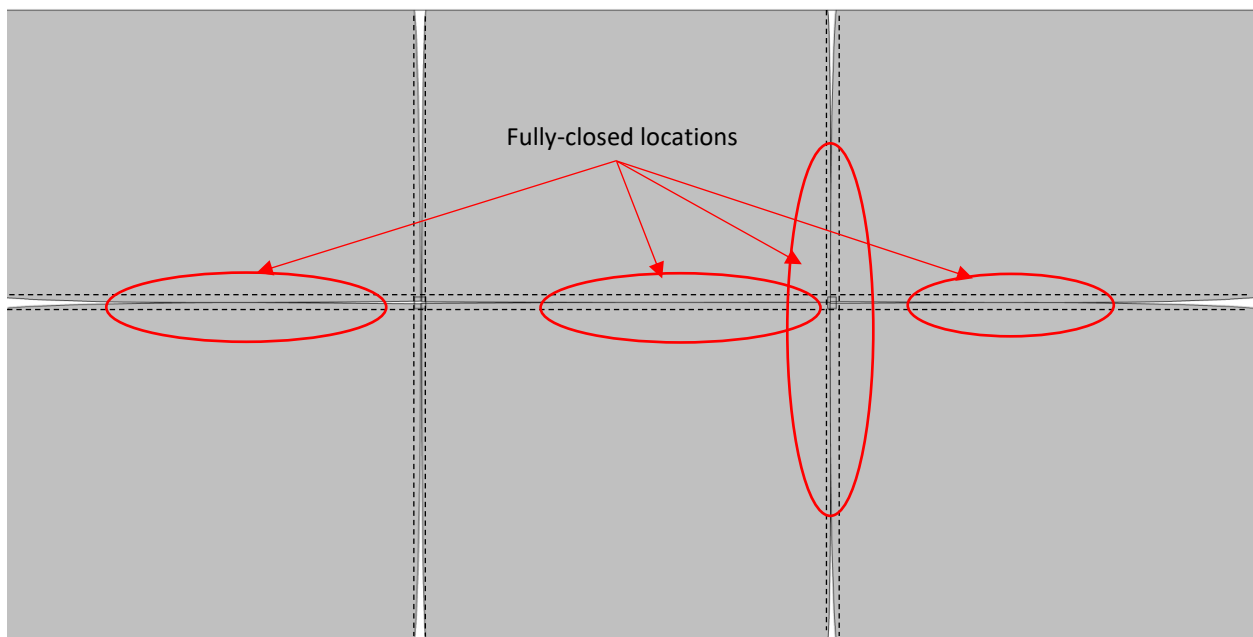
Figure 17 – Further deformed geometry after the completion of both 1st and 2nd simulation phases.

6. Conclusions

This study numerically investigates how the stepwise CO_2 injection affects the structural modifications in fractured coal seam, by developing a fully coupled lab-scale DFM model. Following conclusions are made based on the outcomes of the study.

- When the CO_2 is injected into the fractured coal mass, it rapidly flows through the high permeable fractures, diffuses into low-diffusive matrices, and adsorbs on to potential adsorption sites, causing adsorption-induced matrix swelling. This in turn causes fracture aperture and permeability reduction causing structural modifications in the fractured coal seam.

- The geometric modifications that occurred during the 1st CO_2 injection cycle drastically affects the CO_2 flow behaviour in the 2nd CO_2 injection cycle, in which significant localized flow modifications can be observed in regions near to fully closed fractures.

- However, the structural alterations that occur in the 2nd cycle are not as adverse as that in the 1st cycle, probably due to the Langmuir-type models adopted in adsorption and swelling processes. However, these models are well-confirmed with experimental results; thus, the developed fully coupled model is capable of successfully incorporating them in the simulations.

51

- Overall, it can be concluded that the CO_2 adsorption-induced structural alterations are highly localised in fractured coal seams; hence, the modelling should be done by using DFM approach that incorporates distinct fracture and matrix domains and their explicit geometric properties.

7. Reference

Agheshlui, H., Sedaghat, M. H., & Matthai, S. (2018). Stress influence on fracture aperture and permeability of fragmented rocks. *Journal of Geophysical Research: Solid Earth*, *123*(5), 3578–3592.

Aminian, K. (2003). Coalbed Methane-Fundamental Concepts. *Petroleum & Natural Gas Engineering Department, West Virginia University*, 8–15.

Bertrand, F., Buzzi, O., & Collin, F. (2019). Cleat-scale modelling of the coal permeability evolution due to sorption-induced strain. *International Journal of Coal Geology*, *216*, 103320.

COP21. (2015). *Adoption of the Paris Agreement—Annex: Paris Agreement. United Nations Framework Convention on Climate Change (Cop21), Paris France (30 Nov e 11 Dec). Http://unfccc.int/resource/docs/2015/cop21/eng/l 09.pdf (accessed December 2015)*.

Coulomb, C. A. (1773). Sur une application des regles de maximums et minimums a quelques problemes de statistique relatifs a larchitesture. *Académie Royale de Science Memorie Mechanics and Mining Sciences*, *7*, 343–382.

Crank, J. (1979). *The mathematics of diffusion*. Oxford university press.

Cui, X., & Bustin, R. M. (2005). Volumetric strain associated with methane desorption and its impact on coalbed gas production from deep coal seams. *Aapg Bulletin*, *89*(9), 1181–1202.

Darcy, H. P. G. (1856). *Les Fontaines publiques de la ville de Dijon. Exposition et application des principes à suivre et des formules à employer dans les questions de distribution d'eau, etc*. V. Dalamont.

Kang, J., Zhang, B., Wang, J., Wu, J., Wang, L., Yin, B., & Kang, T. (2019). Mechanical testing of anthracite to assess its surface energy and temperature dependence. *Fuel*, *239*, 76–86.

Lepillier, B., Daniilidis, A., Gholizadeh, N. D., Bruna, P.-O., Kummerow, J., & Bruhn, D. (2019). A fracture flow permeability and stress dependency simulation applied to multi-reservoirs, multi-production scenarios analysis. *Geothermal Energy*, *7*(1), 24.

Ma, Q., Harpalani, S., & Liu, S. (2011). A simplified permeability model for coalbed methane reservoirs based on matchstick strain and constant volume theory. *International Journal of Coal Geology*, *85*(1), 43–48.

Masoudian, M. S., Airey, D. W., & El-Zein, A. (2014). Experimental investigations on the effect of CO_2 on mechanics of coal. *International Journal of Coal Geology*, *128*, 12–23.

Mazumder, S., Wolf, K., Van Hemert, P., & Busch, A. (2008). Laboratory experiments on environmental friendly means to improve coalbed methane production by carbon dioxide/flue gas injection. *Transport in Porous Media*, *75*(1), 63–92.

Oudinot, A. Y., Koperna, G. J., Philip, Z. G., Liu, N., Heath, J. E., Wells, A., Young, G. B., & Wilson, T. (2011). CO2 injection performance in the Fruitland coal fairway, San Juan Basin: Results of a field pilot. *SPE Journal*, *16*(04), 864–879.

Pan, Z., & Connell, L. D. (2007). A theoretical model for gas adsorption-induced coal swelling. *International Journal of Coal Geology*, *69*(4), 243–252.

Robertson, E. P., & Christiansen, R. L. (2005). *Modeling permeability in coal using sorption-induced strain data*. Idaho National Laboratory (INL).

Saghafi, A., Faiz, M., & Roberts, D. (2007). CO2 storage and gas diffusivity properties of coals from Sydney Basin, Australia. *International Journal of Coal Geology*, *70*(1–3), 240–254.

Sampath, K. H. S. M., Perera, M. S. A., Ranjith, P. G., Matthai, S. K., Rathnaweera, T., Zhang, G., & Tao, X. K. (2017). CH4-CO2 gas exchange and supercritical CO2 based hydraulic fracturing as CBM production-accelerating techniques: A review. *Journal of CO2 Utilization*, *22*, 212–230.

Sampath, K., Perera, M., Matthai, S., Ranjith, P., & Dong-yin, L. (2020). Modelling of fully-coupled CO2 diffusion and adsorption-induced coal matrix swelling. *Fuel*, *262*, 116486.

Shi, J., & Durucan, S. (2005). CO2 storage in deep unminable coal seams. *Oil & Gas Science and Technology*, *60*(3), 547–558.

Shi, J. Q., & Durucan, S. (2003). A bidisperse pore diffusion model for methane displacement desorption in coal by CO2 injection. *Fuel*, *82*(10), 1219–1229.

Tunc, X., Faille, I., Gallouët, T., Cacas, M. C., & Havé, P. (2012). A model for conductive faults with non-matching grids. *Computational Geosciences*, *16*(2), 277–296.

Witherspoon, P. A., Wang, J. S., Iwai, K., & Gale, J. E. (1980). Validity of cubic law for fluid flow in a deformable rock fracture. *Water Resources Research*, *16*(6), 1016–1024.